FORCE SPACE STUDIES OF ELASTOMERIC ANISOTROPIC FIBRILLAR ADHESIVES

A DISSERTATION

SUBMITTED TO THE DEPARTMENT OF APPLIED PHYSICS

AND THE COMMITTEE ON GRADUATE STUDIES

OF STANFORD UNIVERSITY

IN PARTIAL FULFILLMENT OF THE REQUIREMENTS

FOR THE DEGREE OF

DOCTOR OF PHILOSOPHY

Daniel Ruben Soto

August 2010

This dissertation is online at: http://purl.stanford.edu/vw463hb1522

I certify that I have read this dissertation and that, in my opinion, it is fully adequate in scope and quality as a dissertation for the degree of Doctor of Philosophy.

Thomas Kenny, Primary Adviser

I certify that I have read this dissertation and that, in my opinion, it is fully adequate in scope and quality as a dissertation for the degree of Doctor of Philosophy.

Kathryn Moler, Co-Adviser

I certify that I have read this dissertation and that, in my opinion, it is fully adequate in scope and quality as a dissertation for the degree of Doctor of Philosophy.

Mark Cutkosky

Approved for the Stanford University Committee on Graduate Studies.

Patricia J. Gumport, Vice Provost Graduate Education

This signature page was generated electronically upon submission of this dissertation in electronic format. An original signed hard copy of the signature page is on file in University Archives.

Abstract

Previous research into the climbing ability of the gecko lizard has revealed an adhesive system fundamentally different from existing synthetic adhesives. Instead of using a soft material, the gecko uses a complex system of hairs of beta-keratin, a material that is not tacky. This unique architecture affords the adhesive characteristics that make it well suited for climbing.

Borrowing themes from the gecko, we developed a synthetic adhesive possessing similar properties using molded arrays of micron-scale silicone pillars. These arrays demonstrate the gecko property of frictional adhesion where increased shear stress at the interface leads to increased normal load capacity. To distinguish between intrinsic and emergent behavior, we also isolated single pillars to test on a dual-axis force-sensing cantilever capable of micro-Newton resolution. We observed that gecko-like properties were observed for tapered pillars but not for pillars of uniform cross-section.

Most synthetic adhesive architectures use a uniform cross-section beam but the results presented here suggest such a design does not capture gecko-like behavior. These results point to ways to optimize the type of adhesion demonstrated by the synthetic dry adhesives and to create adhesives tailored for climbing or static applications.

Acknowledgements

This work would not have been possible without the efforts and encouragement of many people. My principal advisor, Tom Kenny, has been a great guide and mentor, encouraging me to look beyond the details of the work at hand to see the larger context and impact. Mark Cutkosky has allowed me to collaborate with his lab and the experience has been very valuable. It has been interesting and valuable to be member of two labs with different cultures. Kathryn Moler has been a source of advice during my time at Stanford, her tough questions have improved the quality of my work. My mentor in the Kenny group was Ginel Hill. Her work provided the platform for many of the measurements presented in this work. In Aaron Parness and Noé Esparza, I found both colleagues and friends. Their expertise made this work possible and their friendship made this work enjoyable. There is also a larger group of graduate student colleagues. The Kenny group is a place with wide-ranging skill sets and interests. Advice has been available on topics ranging from embedded electronics to energy policy, from silicon nitride to skiing. I have enjoyed my time here and am grateful to everyone current and past. The BDML lab has provided another group of friends and colleagues for support both academic and personal. I'd also like to acknowledge the DARE fellowship and the VPGE for their support over the past two years. The VPGE is doing great work to make sure that the graduate experience at Stanford works for all students. I would also like to thank the Physics and Astronomy program at San Francisco State University for giving me the opportunity to demonstrate my potential as a graduate student. Last, some very personal thanks to my family. My parents have done their best to encourage and support my scientific curiosity. They made sure that computers and chemistry sets

were available for me to learn and play. I know they made sacrifices to nurture my abilities and I am grateful to them for that. The last thank you goes to my wife Alissa. Her patience, compassion and support have kept this journey from being a lonely one.

Contents

List of Tables

List of Figures

Chapter 1

Introduction

The elucidation of the structure of the gecko adhesive mechanism has revealed a new adhesive architecture and technology. Before the mechanisms of the gecko's adhesive system were investigated, most known adhesive systems consisted of a very soft material that could create large surface areas between two rigid surfaces. Examples of this architecture include adhesive tape and the toes of many frogs. In each case a tacky intermediate material is used to increase surface area. Conventional adhesive materials are soft, with bulk moduli below 100 kPa [1]. The gecko uses micron and nanometer scale hairs of β-keratin, which has a bulk modulus of 1.6 GPa [2], to form its adhesive. The material these hairs are made from is much stiffer than conventional adhesive materials found on adhesive tape. This opens an avenue for the creation of adhesives that no longer rely on the intrinsic properties of the adhesive material but rather on the geometry of the material. Conventional pressure sensitive adhesive materials are subject to creep, outgassing, and temperature dependence. Adhesives made from suitably chosen materials can avoid these problems. Polydimethylsiloxane (PDMS rubber), polypropylene, and carbon nanotubes have been used to fabricate gecko-inspired adhesives. These materials can be used for adhesives appropriate for high temperature or low pressure environments where traditional adhesive materials are likely to fail.

1.1 Outline

This work describes the fabrication and investigation of a gecko-inspired artificial adhesive. In Chapter 2, useful background material is presented for understanding this fibrillar artificial adhesive. This material includes models of adhesive behavior and a review of previous fibrillar adhesives. The design and fabrication process of these adhesives is described in Chapter 3. In Chapter 4, fabricated arrays are tested and their adhesive properties are described. Individual adhesive elements are isolated from arrays and tested in Chapter 5. In Chapter 6, models and simulations are described that suggest that pillar shape plays a role in the type of adhesion observed and predict some of the behavior observed in the testing in Chapters 4 and 5.

Chapter 2

Background

This chapter provides a brief introduction to the theory of adhesives. This introduction provides a basis of understanding for fibrillar adhesives and how they differ from the most familiar example, adhesive tape. The chapter ends with a review of other gecko inspired adhesives.

2.1 Adhesion Fundamentals

To better understand fibrillar adhesives, it is useful to start with a discussion of adhesion in general and the fundamentals of more familiar adhesives such as tape. Adhesives rely on intermolecular forces as the attractive forces between objects [1].

2.1.1 van der Waals Adhesion

Chief among these intermolecular forces that are responsible for adhesion are the van der Waals forces [1]. These forces result from dipole moments in the materials attracting each other. Even materials without permanent dipole moments such as noble gases, have instantaneous dipole moments from quantum-mechanical fluctuations. These fluctuating dipole moments result in an overall attractive force [3].

At distances greater than several nanometers, these van der Waals forces fall off quickly and the maximum attractive force is found at a distance of a few nanometers.
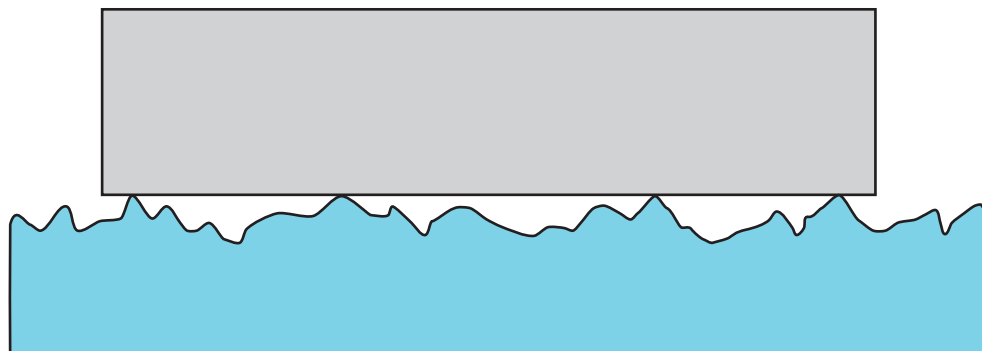
Figure 2.1: Depiction of surface roughness between two surfaces that are intended to be adhered together. The top gray surface is depicted as perfectly smooth for simplicity. The bottom blue surface shows a surface roughness common to most materials. It is only in the regions around where contact is made that van der Waals forces can act. In this case, this the area is very small.

In order for this van der Waals attraction to create adhesive forces large enough to hold two objects in contact, the amount of area in close proximity must be large. Since most surfaces have a surface roughness that exceeds this nanometer length scale for attractive force, the surfaces must deform in order for large areas to be sufficiently close for the van der Waals interaction. In Figure 2.1 there is an idealized depiction of a perfectly smooth surface in contact with a rough surface. This image shows how very close contact only occurs in a few locations while other areas are too far away for significant attractive force. In Figure 2.2 the yellow layer represents an intermediate layer of adhesive between the smooth and rough surfaces. This adhesive layer is very soft and able to deform so that large areas are in close contact with the rough surface. Pressure sensitive and fibrillar adhesives use two different approaches to create these large areas of intimate contact necessary for macroscopic adhesion.
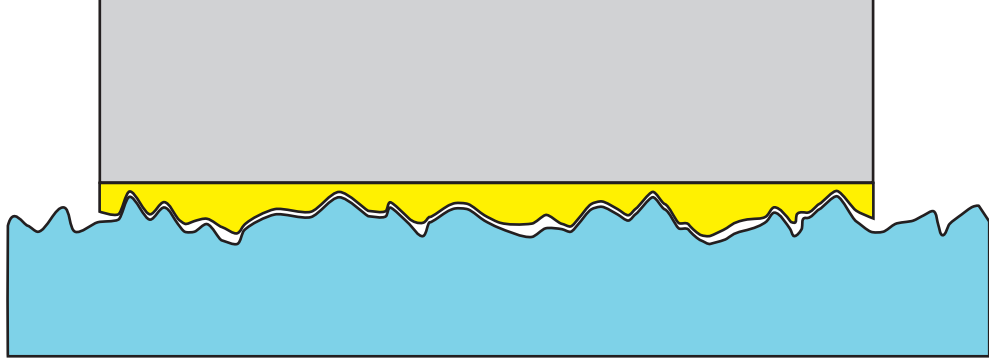
Figure 2.2: Depiction of the role that a pressure sensitive adhesive (yellow) plays in increasing the amount of intimate surface contact between two surfaces. In Figure 2.1, only small areas were close enough for van der Waals interaction. The addition of the yellow intermediate material increases this intimate contact area.

2.1.2 Pressure Sensitive Adhesives

Pressure sensitive adhesives use a material that is very soft to create the intermediate layer between two rigid materials. In addition to being soft, the material must also be cohesive enough to withstand tensile stress in the material. To see how a soft cohesive material can create adhesion, we consider the amount of contact between two surfaces having a pressure sensitive intermediary layer. The equilibrium area of contact can be thought of as the area that minimizes the following energy equation

$$U_{\text{total}} = -\Delta\gamma A + U_{\text{deformation}}(E, A) \qquad (2.1)$$

where the first term $(-\Delta\gamma A)$ is the lowering of the energy of the system when the two surfaces make contact, and the second $(U_{\text{deformation}}(E, A))$ the raising of the system's energy as the material is deformed to cause a contact area A. The surface energy per unit area $\Delta\gamma$ is a function of the material properties such as the polarizability and is directly proportional to the amount of area in contact. The deformation
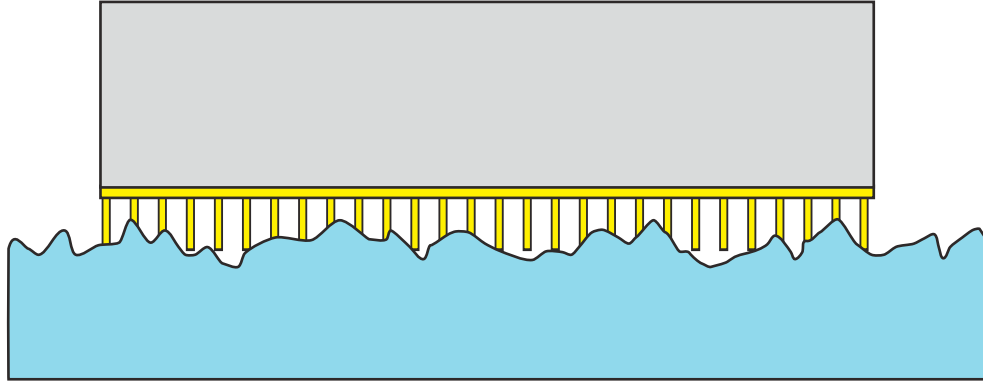
Figure 2.3: Depiction of the role that a fibrillar adhesive (yellow) plays in increasing the amount of intimate surface contact between two surfaces. In this case, the surface roughness is filled by fine hairs that can make contact at different distances from the smooth surface. These hairs allow for more van der Waals interaction area compared to the bare surfaces.

energy is an increasing function of the amount of area in contact and the Young's Modulus or rigidity of the material.

Carl Dahlquist determined empirically that a material with a Young's Modulus less than 100 kPa is tacky [1]. This means that the equilibrium value of A in Equation 2.1 is large enough for the materials to exhibit adhesion.

2.1.3 Fibrillar Adhesives

Fibrillar adhesives do not rely on the low Young's Modulus of an adhesive material. The gecko uses a material (β-keratin) that has a modulus of $\sim$2 GPa, roughly four orders of magnitude above the Dahlquist criterion. The gecko makes this material behave like an adhesive by creating very fine, slender structures. These fine structures create a material that has an effective modulus that fulfills the Dahlquist criterion. The use of hairs rather than a planar layer allows the gecko adhesive to demonstrate

properties not seen in pressure-sensitive adhesives like tape or rubber cement.

The most striking of the properties of the gecko adhesive that are a result of its fibrillar structure is the directional or anisotropic behavior. This means that depending on the orientation of the gecko hairs and the direction of the stress applied, that the adhesive behavior will be different. The other property, though more subtle, is that the adhesion displayed by the gecko adhesive is qualitatively different than the type of adhesion displayed by pressure sensitive adhesives. We can visualize these unique properties with the aid of a concept called the limit surface.

2.2   Limit Surface

To understand the properties of these different adhesives, it is useful to look at the adhesive stresses in a space where the forces in x, y, and z directions are the axes of the space. We will call this space the force space. The limit surface is then the locus of points in this force space where relative movement between the two surfaces occurs. This limit surface generally divides the force space into regions where stable attachment is possible and where relative movement of the adhesive and substrate (adhesive failure) will occur. For a limit surface, a sliding failure where the two surfaces are still in contact and a detachment failure where the two surfaces separate are considered equivalent. Most of this discussion involves two-dimensional force spaces so, strictly speaking, we will be mainly discussing limit curves. We can empirically determine the limit curve of an adhesive contact by subjecting the adhesive interface to stress until the interface fails. To trace out the limit surface, these stresses should be in proportions varying between primarily normal stress and primarily shear stress.

2.2.1   Coulomb Friction Limit Surface

A familiar system that we can use as a limit surface example is the ideal friction of a block on an inclined plane. As we see in Figure 2.4, this limit surface is a simple

pair of sloped lines given by

$$F_N = \frac{1}{\mu}|F_S|.$$

For values of θ less than the critical angle θ_c, the normal and shear forces at the interface lie in the shaded region of the plot and the block does not slide. When the angle exceeds θ_c, the force pair lies outside the stable grey region, the interface fails, and the block begins to slide. The shaded surface does not include any region with negative values of F_N which means that this interface cannot support any adhesion.

   We can envision other limit surfaces related to this ideal coulomb-friction surface to help build some intuition. First, consider a hockey puck or curling block on ice. The interface between the puck and the ice can be sheared with very little force. Assuming the surface obeys coulomb friction, the limit surface will be a v-shaped surface with a relatively steep slope. The slope is equal to the reciprocal of the coefficient of friction, so for ice, this slope will be of large magnitude. A smooth-soled shoe will also have a low-coefficient of friction on this smooth ice. This means that attempting to create a large shear stress at the interface will lead to interface failure or slipping, a result familiar to anyone who has walked and fallen on ice. In contrast to this situation, consider instead, rubber soled tennis shoes on asphalt. This interface will support a large amount of stress for a given normal force. This surface will have a lower magnitude slope and will include a greater percentage of the half of the force space that is compressive. We can take this limit surface to an extreme by imagining a frictionless, weightless, rigid dowel in a matching hole. In the normal direction, the dowel can be removed with any non-zero tensile force and can withstand any compressive force. It can also bear any shear load without moving. In this case, the limit surface is the shear force axis and the stable region is the compressive half-space. Each of these examples will demonstrate isotropic friction, that is, though we are considering limit curves in two dimensions, if we extend to three dimensions of force space, these v-shaped curves will become cone-shaped surfaces. We now describe some anisotropic surfaces.

   If we consider the interaction of a skateboard and a concrete surface, we have an anisotropic limit surface. For forces along the long axis of the skateboard, there is very
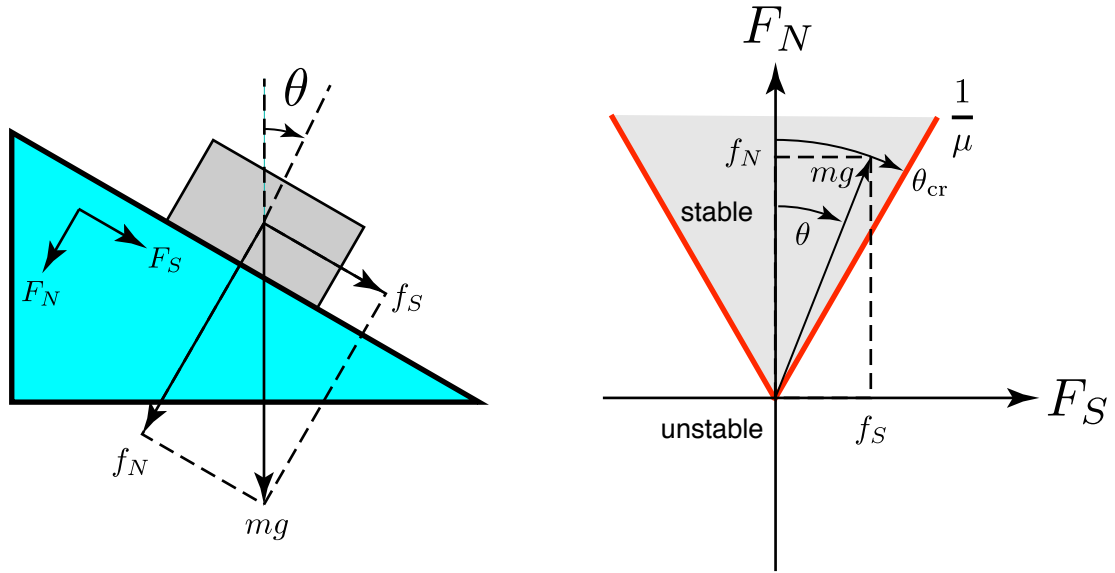
Figure 2.4: Coulomb friction limit curve. The gray area indicates pairs of normal and shear forces at the adhesive interface that remain attached. Pairs of forces below the red limit curve will result in the breaking of the adhesive interface. For a block on a plane, the force pairs form a circular arc with radius mg that sweeps a circle as θ is increased. When θ is greater than the critical angle θ_{cr}, the arc crosses the limit curve and sliding begins. Also, if any tensile normal stress is created at the interface the surfaces will detach.
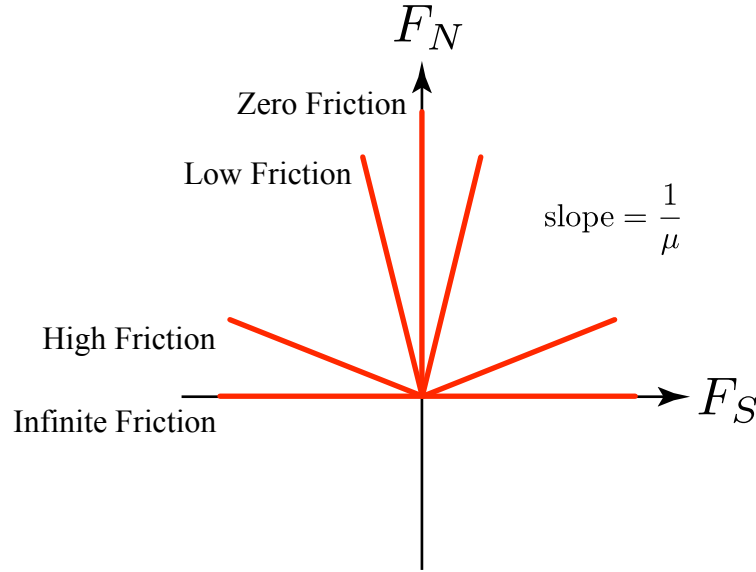
Figure 2.5: These four limit curves depict ideal Coulomb friction surfaces with varying coefficients of friction. The region above each of these curves is the stable region. The 'Zero Friction' limit curve is a vertical line for a zero-friction surface. At the other extreme, an peg in a hole would create a horizontal line for an infinite friction surface. The intermediate surfaces represent smooth and rough surfaces such as ice on ice and rubber on asphalt.

low resistance to movement since the bearings are designed to roll with little friction. Though the bearing forces are complex, we will assume that increasing normal force on the skateboard adds to the rolling resistance. For forces along the short axis of the skateboard, the limit curve along that axis is determined by the coefficient of friction between the urethane wheels and the concrete surface. This gives a limit surface that is not rotationally symmetric about the normal force axis. The natural gecko adhesive, due to its structure, also does not exhibit a surface that is rotationally symmetric.

2.2.2 Embedded Cone Model

To include the effects of adhesion, an old and simple model known as the embedded cone model captures much of the behavior. This model simply subtracts an offset
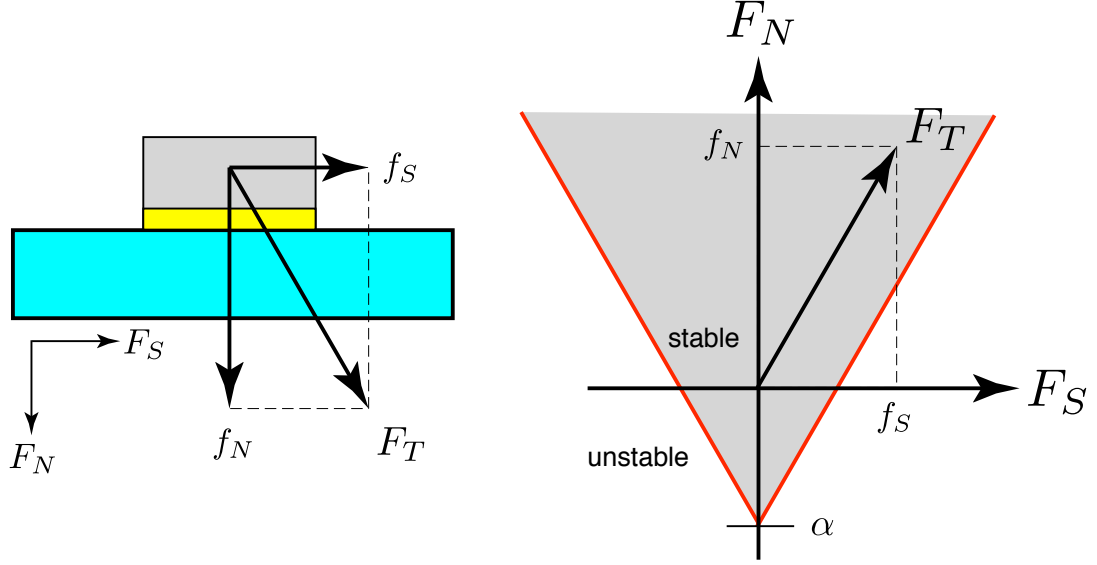
Figure 2.6: Embedded cone limit curve. The gray area indicates pairs of normal and shear forces at the adhesive interface that remain attached. Pairs of forces below the red limit curve will result in the breaking of the adhesive interface. The α indicates the maximum tensile normal force that the interface can withstand. Note that in contrast with the coulomb surface, that there are areas within the stable area that can withstand normal tensile forces.

from the coulomb friction limit surface [4, 5].

$$F_N = \frac{1}{\mu}|F_S| - \alpha$$

The limit surface now includes the origin and regions with negative values of F_N.

As we did with the ice and asphalt, we can conduct a thought experiment to envision limit curves including adhesion. Consider for example a frictionless refrigerator magnet. Any amount of shear force will result in interface failure and relative movement. The limit curve is then only a line along the normal force axis that extends from infinite compression to the strength of the magnet in tension. As we add friction to the interface, the slopes will reduce in magnitude as we saw for the ice and asphalt examples. If we place this magnet on the end of the dowel from our previous
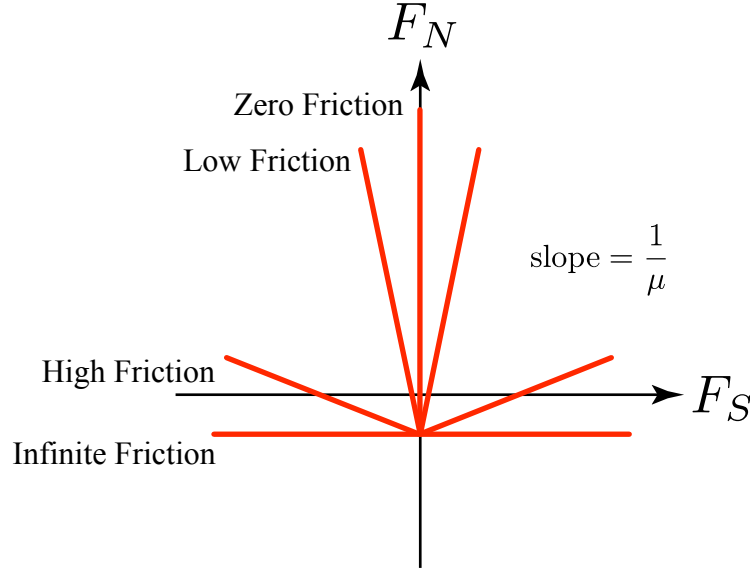
Figure 2.7: These four limit curves depict embedded cone surfaces with varying amounts of shear friction but equal amounts of maximum normal capacity. The zero friction limit curve is a fictional, frictionless magnet that withstands no shear force but some tensile normal force. Low and high friction curves correspond to a magnet with either low or high friction. The infinite friction curve could be the result of a peg in a hole attached by adhesive at the bottom.

examples, we will have a limit surface that is a line parallel with the shear force axis.

2.2.3 Savkoor Briggs Model

The adhesive behavior exhibited by pressure sensitive adhesives is also observed in the contact of hemispherical surfaces. Savkoor and Briggs introduced a model for hemispherical contacts that accounts for the shear and normal forces and their interaction [6]. The Savkoor-Briggs theory is an extension to earlier theories on the interactions between hemispherical surfaces [7, 8]. The Hertz theory [7] treated the deformation of hemispherical surfaces in the presence of compressive forces but in the absence of attractive surface forces. The JKR theory [8] extended the Hertz theory to include attractive surface forces. The JKR theory predicts a finite adhesion force for a hemisphere in contact with a plane dictated by the surface energy of the material

(γ) and the radius (R) of the hemispherical surface.

$$F_N = -\frac{3}{2}\pi\gamma R \tag{2.2}$$

This JKR prediction for the force at detachment of a fibril is widely used but does not account for shear stress. The Savkoor-Briggs theory extends the JKR theory by accounting for the presence of shear stress at the adhesive interface. In this analysis, the shear force causes a reduction of the radius of contact predicted by JKR theory and thus a reduction in the normal direction adhesive force. Their model can be plotted as a limit surface to reveal, instead of a cone, a parabolic surface.

The Savkoor-Briggs model provides an expression for F_N as a function of F_S. It is a parabolic function with a y-intercept of $-\frac{3}{2}\gamma\pi R$, the JKR pulloff force for zero shear:

$$F_N = \frac{K\lambda}{32\gamma\pi R}F_S^2 - \frac{3}{2}\gamma\pi R$$

Where $K\lambda$ forms a dimensionless factor that takes into account the shear modulus and bulk modulus of the material and ends up being a function of the Poisson's ratio of the material. For a polymer $\nu = 0.5$, $K\lambda = 8$ and the normal force at failure is given by

$$F_N = \frac{1}{4\gamma\pi R}F_S^2 - \frac{3}{2}\gamma\pi R$$

We see that like the embedded cone model, the maximum normal adhesive force occurs when the shear force (F_S) is zero.

2.2.4   Frictional Adhesion Limit Surface

The limit surface displayed by the gecko (Figure 2.8) is unlike the embedded cone or Savkoor-Briggs limit surfaces that describe pressure-sensitive adhesives. It instead follows a model termed frictional adhesion [9]. The first clear difference is that the frictional adhesion surface exhibited by the gecko is not symmetric about the origin. Another important difference is that the frictional adhesion limit surface crosses

through the origin. Since the limit surface crosses the origin, that means that forces of relatively low magnitude can release the adhesive depending on the direction of the force. The asymmetric limit surface reflects the fact that the gecko's adhesive structure is also asymmetric. This anisotropic or directional behavior is one of the properties we want to replicate in our fibrillar adhesives. Were we to add a dimension in our force space for forces in the transverse direction, we would have axes for F_N, the normal force, F_S, the shear force, and F_T, the transverse force, and we would see that the gecko surface is symmetric about the $F_N - F_S$ plane. We could equivalently say that the limit surface is an even function of the transverse force. The asymmetry means that in one direction the gecko adhesive behaves like a coulomb-friction surface while in the other direction the adhesive behaves in a very novel way. As Figure 2.8 shows, as the amount of shear stress at the interface increases, the amount of normal stress that the interface can withstand is increased. This is an advantageous property for an animal that climbs vertical surfaces. The natural application of shear stress due to the weight of the animal will result in the ability to withstand moments that arise because the animal's center of gravity is away from the wall. This stress will increase while the animal is in motion and the stability of the interface will increase [10]. This frictional adhesive property is very advantageous for climbing and was a property we wanted to achieve in our fibrillar adhesive.

2.3   Previous Literature

There have been many attempts in the literature to make adhesives inspired by the gecko adhesive. The work described here is distinguished by our objective of creating an adhesive that will be well suited for climbing. This means that the gecko properties of anisotropy and frictional adhesion are important while other properties of the gecko adhesive such as multilevel hierarchy and nanometer terminal feature dimension may not be necessary. A brief summary of the gecko-inspired adhesives relevant to this work follow.

There have been many demonstrations of fibrillar adhesives made from materials that do not fulfill the Dahlquist criterion [11, 12, 13, 14, 15]. Commonly used materials
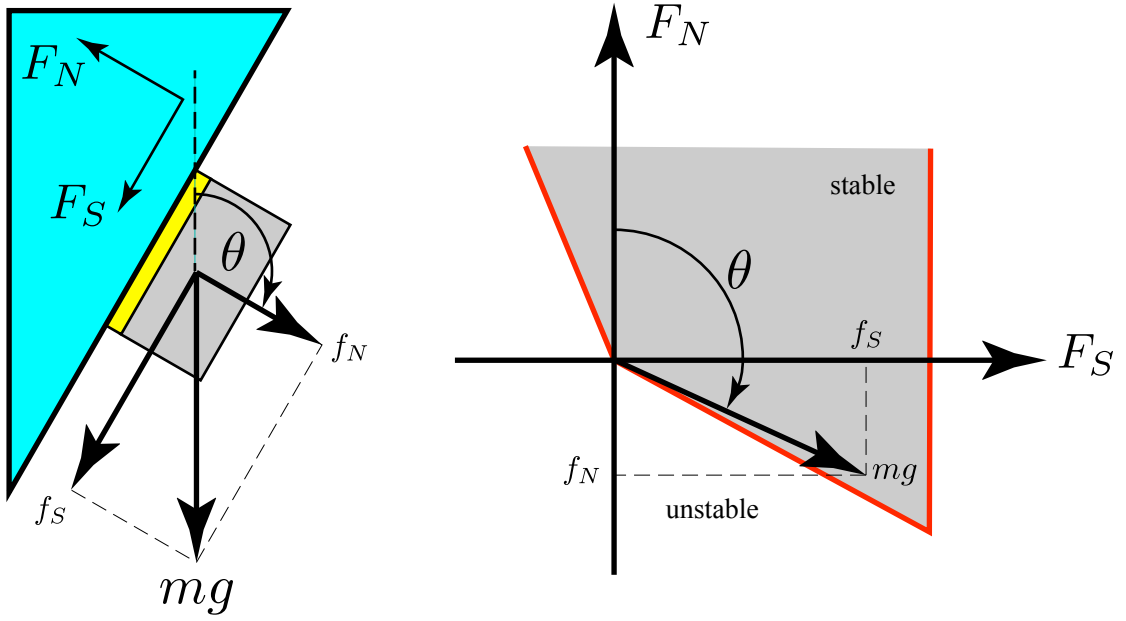
Figure 2.8: Frictional adhesion limit surface showing increased normal adhesive stability with increased shear stress. The grey area shows regions of stable attachment while the white areas below the curve are unstable areas where the adhesive will detach. The arrow on the force space graph shows the projections of the gravity force on the shear force and normal force axes. The positive F_N direction denotes compressive normal stress at the interface.

in the literature are elastomeric polymers [16, 12], carbon nanotubes [13, 17, 18], and thermoplastics [19]. The initial gecko-inspired adhesives exploited the principle of contact splitting [20] to create fibrillar adhesives that demonstrated adhesion in the normal direction. This contact splitting principle states that increasing the number of terminal features leads to improvement in adhesion.

These first fibrillar structures were simple pillars, [11] fabricated from polymethylmethacrylate (PMMA). These pillars were approximately 200 nm in diameter and $2\,\mu$m tall. The contact splitting principle has been taken to an extreme by researchers using carbon nanotubes [13, 17, 18]. The size and density of carbon nanotube arrays explain why they often report adhesion in excess of the gecko.

Going beyond contact splitting, researchers investigated the role of tip shape, adding structures to the top of the pillars to enhance adhesion [16, 12, 21]. The first of these tip structures often had cylindrical symmetry and formed a flat termination at the top of the pillar. These tips generally enhanced adhesion in the normal direction but were not usually tested for shear force generation or anisotropy. Gorb et al. [12] found that these tips often led to poor shear force performance. This was due to the fact that when the pillar bent under shear load, the surface area available for contact was reduced.

Inspired by the slanted hair architecture in many of the animals that use fibrillar adhesives, researchers began fabricating structures that were angled with respect to the backing layer [22, 23]. These structures began to show interesting interactions between the levels of shear and normal adhesion. Researchers using very slender fibrils (100 nm scale), often found that after repeated use or intentional training, the fibrils would take on a predominant orientation, affording the adhesive anisotropic qualities [17, 19].

The work presented here was motivated by the desire to create an adhesive that possessed the gecko-like behavior necessary for climbing. This included the frictional adhesion property and the anisotropic adhesion. The fabricated structures in this work are inspired by previous work on gecko synthetic adhesives [24] as well as work on slanted micro-structures using SU-8.

In this work we also designed a structure that was asymmetric. A key distinction

in this work is that we envisioned an adhesive structure that would change shape based on the amount of loading and that this change in shape would affect the adhesive properties. This asymmetrical structure has a sharp angled tip that allows the adhesive to present a variable surface area based on the amount of loading.

Chapter 3

Fabrication

3.1 Design Principles

This fabrication process drew inspiration from the adhesive structure of the tokay gecko [25, 26] and previous work [27, 28, 29, 30] on making angled microstructures using SU-8, a photosensitive epoxy. We envisioned a structure that would deform under compression to increase the surface area and achieve the frictional adhesion observed in the gecko.

The SU-8 material had been used successfully to fabricate high-aspect ratio structures so it was our choice for the photosensitive polymer mold material. Issues of ease of use and material compatibility led us to the choice of silicone rubber as the material we would cast and create the pillars with. Urethanes were also considered but because of material incompatibility, they would not cure while in contact with the SU-8 material.

3.2 Overview

This adhesive was created using a molding process. The reusable mold was created using SU-8 on a quartz wafer with a unique lithography process. The mold has an array of wedge-shaped pits. A two-part exposure process was used. The first exposure will create the vertical wall of the mold and the second will create the slanted wall.

We then vacuum cast and cure polydimethylsiloxane rubber (PDMS) in the mold and peel out to release. This process flow is depicted in Figure 3.1.

3.3 Mold

3.3.1 Metal Deposition

To create the mold, we deposited and patterned a thin layer of aluminum on a double polished quartz wafer to create a hardmask. The mold is fabricated using a double-polished transparent 100 mm quartz wafer. The wafer was cleaned using the RCA clean with a sulfuric acid and hydrogen peroxide bath to remove organic material followed by a hydrogen peroxide and hydrochloric acid bath to getter metal ions. We then sputter deposited a 100 nm film of aluminum onto the wafer. Then we performed a standard SNF photolithography process, using 1.0 μm of Shipley 3612 photoresist. This layer of photo resist was exposed with 19.5 mW/cm^2 of ultraviolet light on a contact aligner to create the pattern. The photoresist was developed and the aluminum was etched in a wet bath of phosphoric acid, acetic acid, and nitric acid. The photoresist was removed using a bath of PRX-127 at 40°C for 20 minutes. This aluminum layer served as a mask for the SU-8 layer in a later processing step.

3.3.2 SU-8 Deposition

We then spin coat and bake a layer of SU-8 on the side of the wafer that has the aluminum surface. First, the wafer was cleaned with isopropyl alcohol and then singed at 110°C for 5 minutes to drive off moisture. Approximately 5 mL of SU-8 2035 was drawn into a syringe from the bottle. The wafer is placed on a vacuum chuck spinner and the SU-8 was dispensed on the wafer center. During the dispensing stage, care was taken to avoid creating bubbles trapped in the viscous SU-8. The wafer was then spun at ~1000 RPM for 30 seconds to planarize the SU-8 at a target thickness of 80μm. The wafer was then baked to drive excess solvent from the SU-8 film. Care was taken to ensure even heating of the SU-8 to achieve a uniform thickness film. We used a plate of aluminum with a machined flat surface to make good thermal contact with
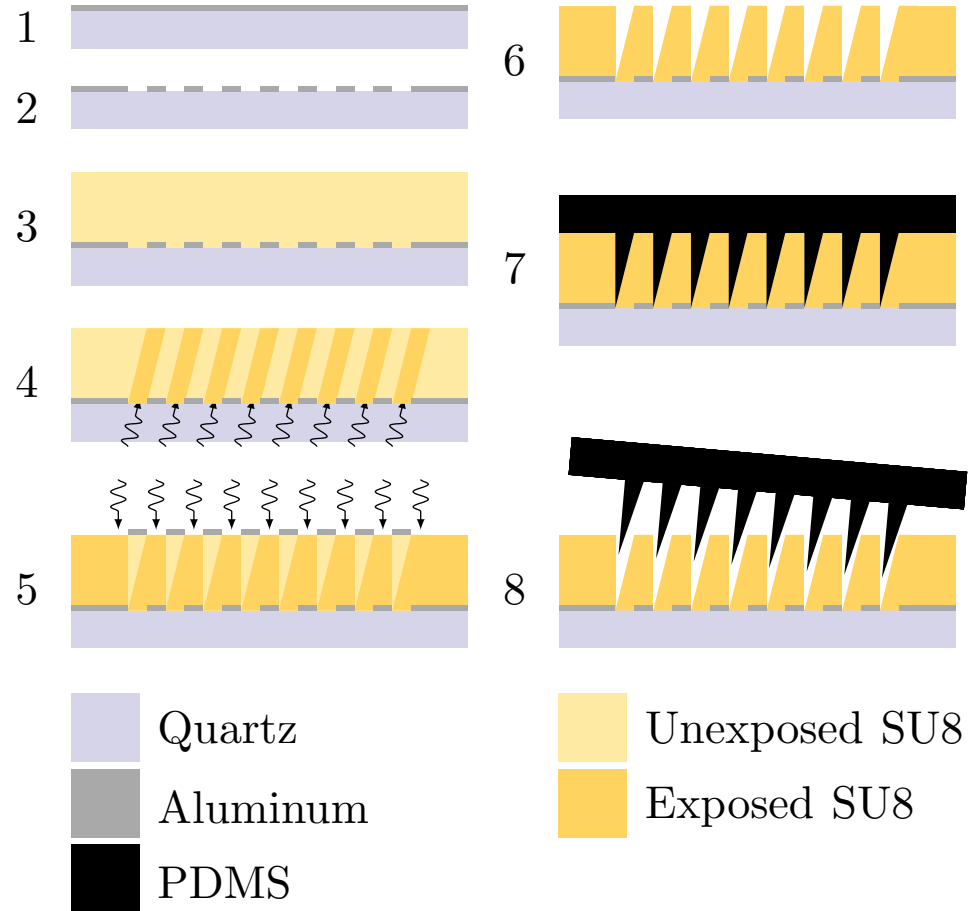
Figure 3.1: Fabrication Sequence 1) Deposit aluminum on quartz wafer 2) Pattern aluminum to create self-aligned mask 3) Deposit SU-8 on top of aluminum 4) Angled self-aligned UV exposure from backside 5) Align mask to topside and UV expose 6) Develop 7) Cast and spin PDMS 8) Peel out cast MicroWedges and backing layer

the hot plate. This provided better contact than the aluminum foil usually placed over the hotplate. We cleaned this plate to remove SU-8 transferred from earlier processes. The wafer was baked on this aluminum plate, starting at 65°C with a slow (5 minute) ramp to 95°C. The wafer was then held at 95°C for 13 minutes.

Special care was exercised during this part of the process. It is during this step that problems in the planarity of the SU-8 would arise. Generally, depressions, would form in the SU-8 often with a small bubble visible at the bottom of the depression. These depressions negatively influenced the yield of the adhesive.

3.3.3 First SU-8 Exposure

We first performed a planar exposure using a contact aligner. The quartz mask was aligned with the hardmask layer to provide registration between the vertical and slanted features. After alignment, the SU-8 was exposed to 200 mW/cm^2 of UV energy. On the Karl Suss contact aligner in the SNF facility, this exposure was performed in 2 equally timed steps (6.9 sec) separated by 10 sec. This exposure was performed with a long-pass filter (PL 360-LP Omega Optical) to block radiation shorter than 350 nm.

3.3.4 Second SU-8 Exposure

After the first exposure, the wafer was placed on a tilted exposure stage. We adjusted the stage, correcting for the index of refraction of the SU-8, to achieve the desired angle for the slanted surfaces of the mold. In this work we chose the pillar face angle to be 14.8° giving the wedges a 4:1 aspect ratio. We then exposed the wafer to ultraviolet light from the underside. The dosage used was 184 mW/cm^2 of UV energy in two equal doses (4.0 seconds) separated by 10 seconds. This exposure was performed under a collimated UV illumination system, taking advantage of the now self-aligned hardmask layer of aluminum.

3.3.5   SU-8 Cure and Develop

The SU-8 was then baked and developed using standard processes found in the SU-8 application notes. We baked the SU-8 on a hotplate for the chemical amplification of the photoresist. The bake started at 65°C and was ramped to 95°C and then held at 95°C for 7 minutes. The wafer was allowed to cool and then placed in a beaker of developing solution for approximately 9 minutes. We agitated the wafer occasionally and inspected for complete development of the SU-8 film. The wafer was then given a 100°C postbake for 5 minutes to harden the resist and prepare it for the temperatures it would experience during the molding process. At this point the mold was complete and ready for use in casting. Figure 3.2 shows a photograph of the transparent mold in a wafer container.

3.4   Casting Process

With the mold complete, we used it to cast a PDMS sample. The PDMS (Dow Corning Sylgard 170) is a two part mixture. Equal mass portions were combined and mixed thoroughly. The mixed and uncured PDMS was placed in a vacuum chamber with the SU-8 mold wafer. The chamber was evacuated and air trapped in the PDMS was liberated. Still under vacuum, the PDMS was poured on the wafer. Air trapped in the mold bubbled through the PDMS and was removed to prevent voids. We then removed the mold from vacuum and spun it to planarize the PDMS backing to the desired thickness. Our backings were in the range of 300 μm to 1200 μm. The PDMS was cured in an oven at 85°C for 15 minutes. The adhesive pillar arrays were released by gently peeling the backing layer from the mold. Figure 3.3 shows the PDMS layer after release from a mold. From these layers of PDMS, we cut samples and mounted them on glass slides for measurements. Figures 3.4 and 3.5 show SEM images of the resulting adhesive pillars.
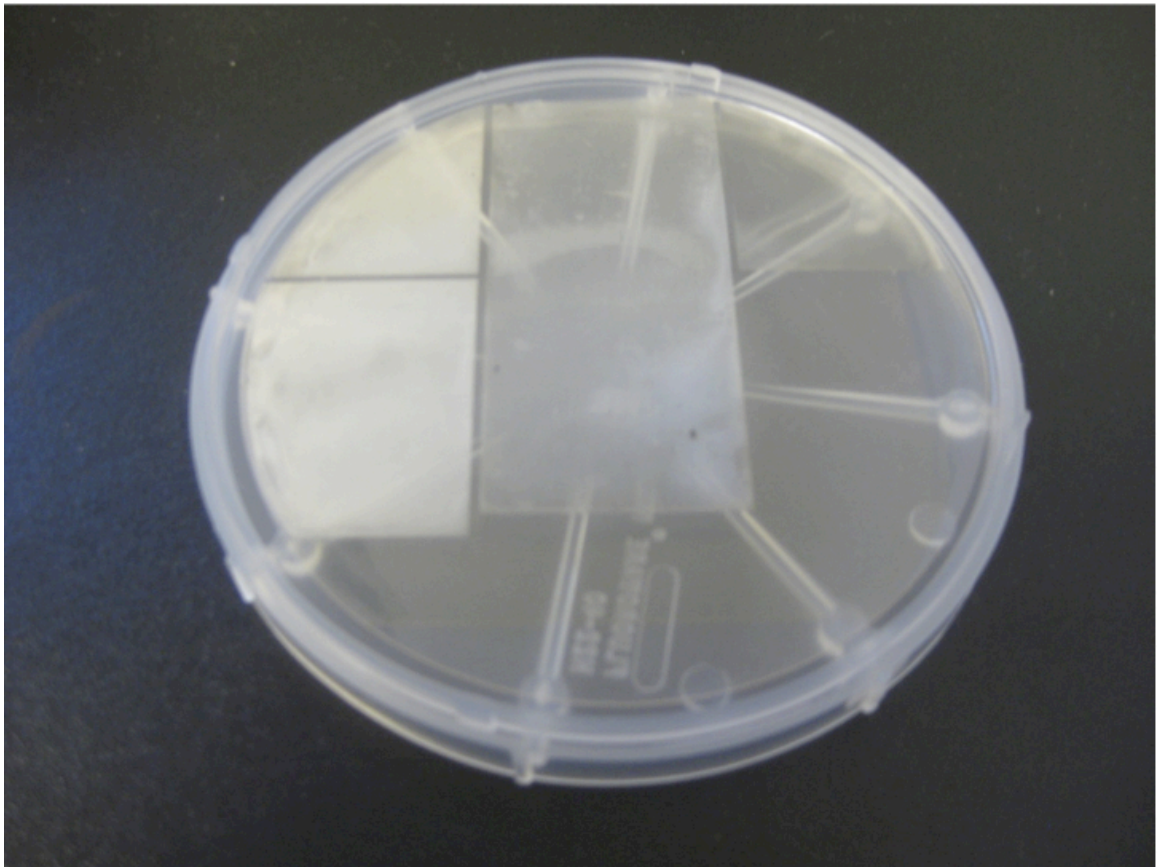
Figure 3.2: Photograph of complete SU-8 on quartz wafer mold. Different colors indicate arrays of different sized structures on the wafer.
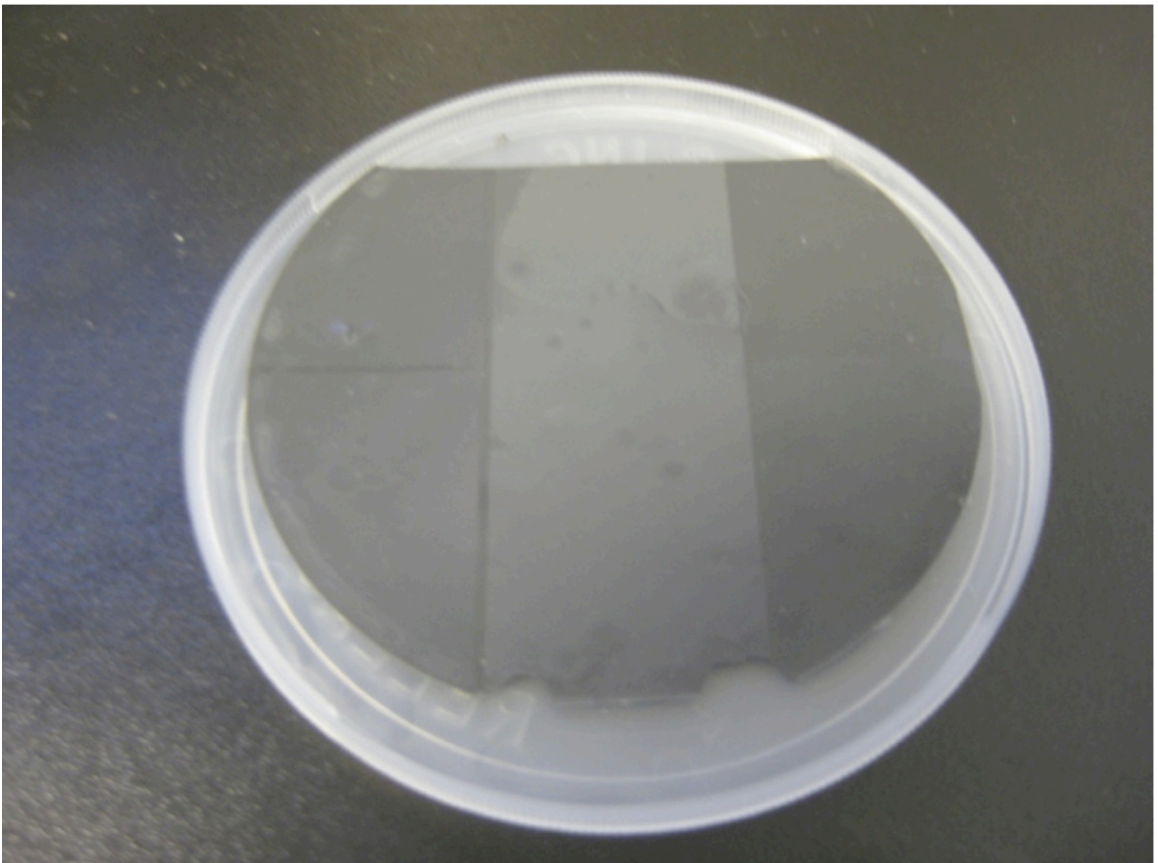
Figure 3.3: Photograph of adhesive pillar array as released from mold. PDMS is cast into the mold and cured and then peeled from the mold.
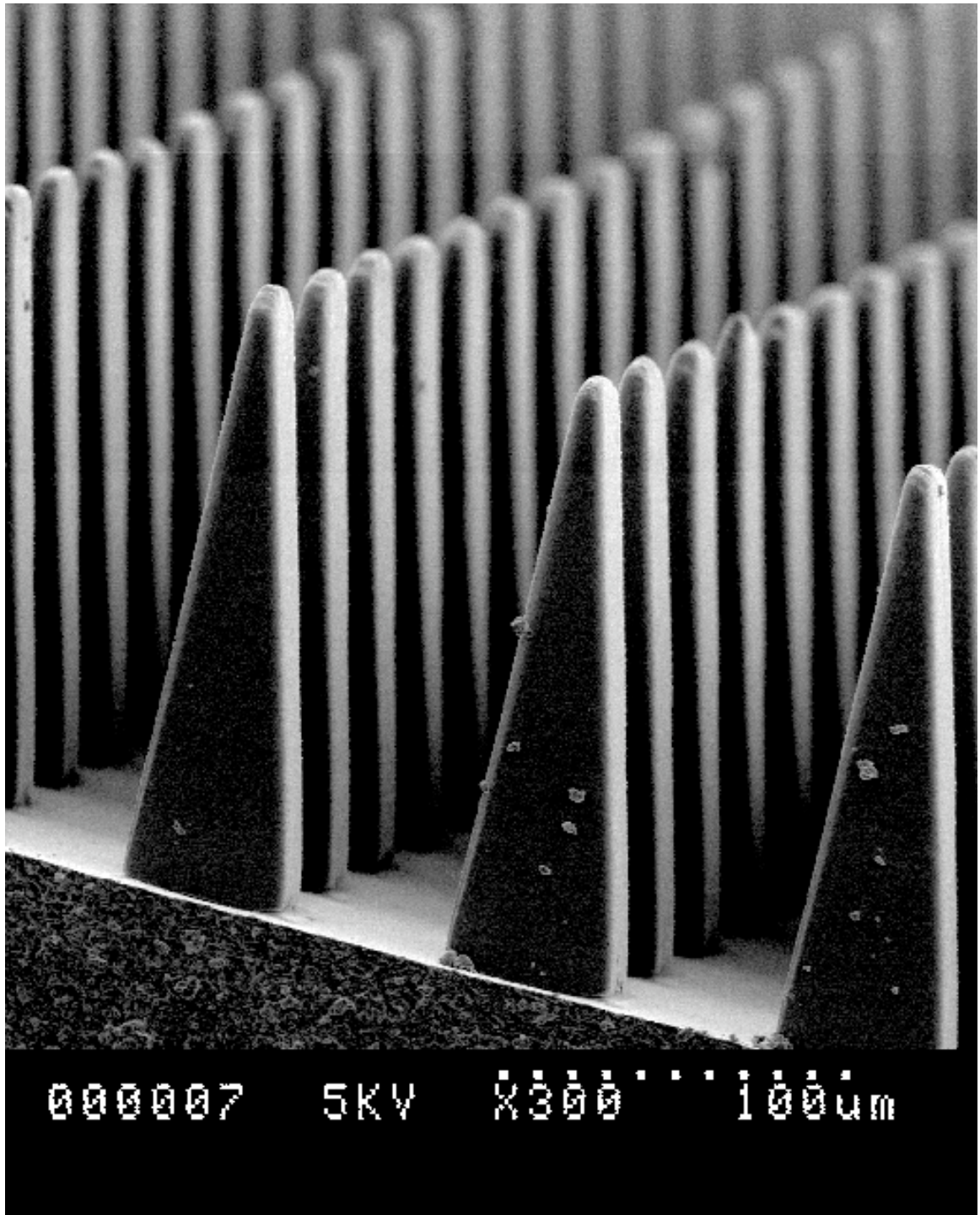
Figure 3.4: SEM image of adhesive pillar arrays. The left edge of the three foreground pillars is vertical and the right edge of these pillars is slanted at approximately 14°.
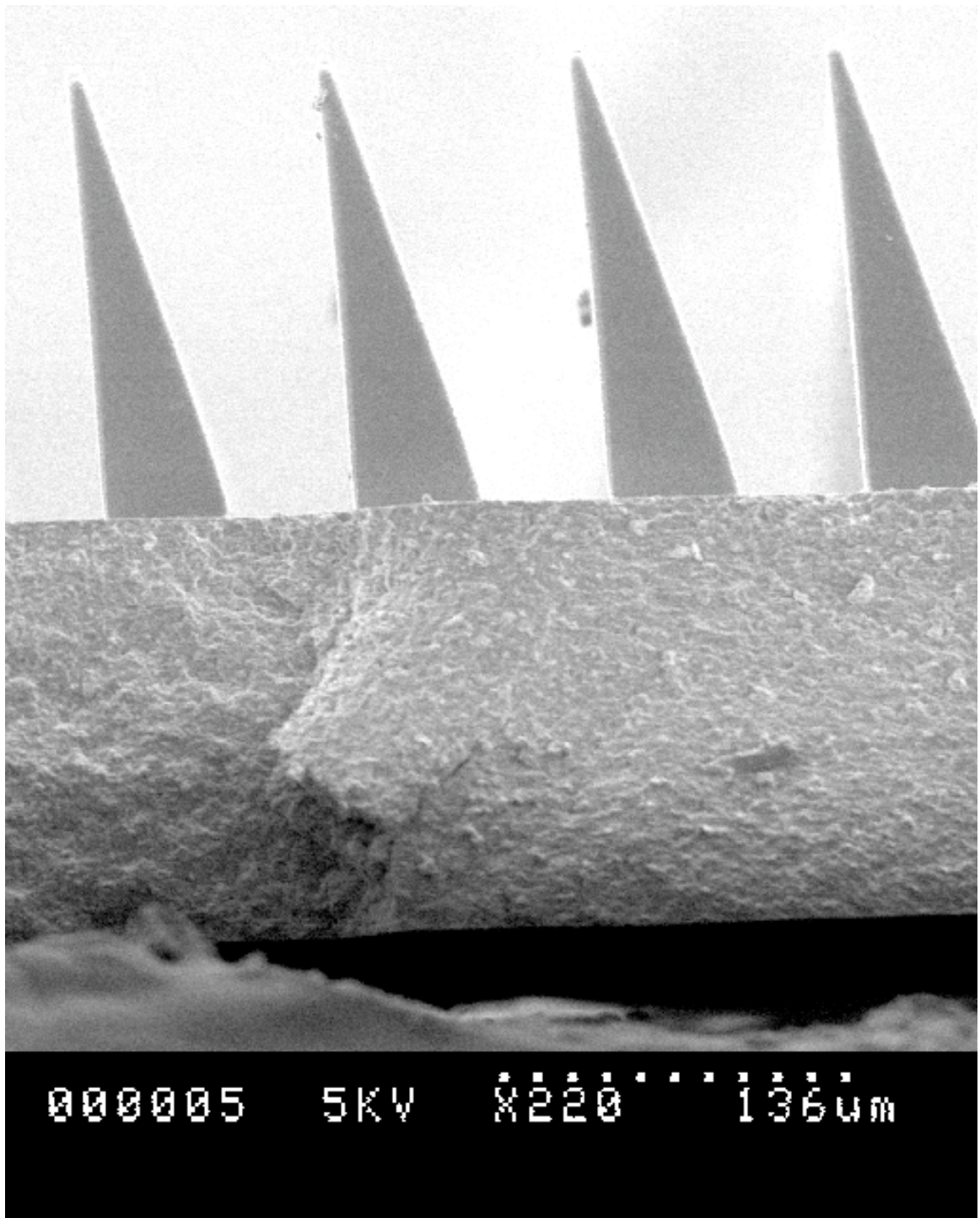
Figure 3.5: SEM profile view of adhesive pillar arrays. The vertical and slanted faces can be seen, as well as the tip of the structure. The thickness of the backing layer is also clearly visible and is equal to the height of the stalks.

3.5 Process Issues

To characterize this process as high-yield would be misleading. Though we could often create large areas of well defined pillars (at least 1 cm^2 with no obvious defects) often molds were unsuccessful.

This section will cover the process problems that we encountered.

3.5.1 Skinning

One especially vexing problem was that during the develop process, a film would form over the top of the mold. The reason for this layer was not determined. This caused two problems. The first problem is reduced yield due to having a reentrant aperture. Figure 3.6 shows a SEM image of this thin layer and adhesive pillars that did not completely release as a result. The second problem is that this leads to an overhang that causes the pillar to sit atop a narrower pedestal. Figure 3.7 shows a SEM image at the base of the pillar showing this narrowing. This introduces an extra compliance at the base of the pillar that affects the mechanics of the pillar. This compliance at the base will result in less bending across the beam, affecting the adhesive behavior.

3.5.2 Scalloping

Another area where the incomplete development of the mold caused noticeable variability in the structures was at the tip of the mold. In a feature reminiscent of "grass" in deep reactive ion etching processes, thin membranes of SU-8 remain in the bottom of the mold where the adhesive tip is formed. Figure 3.8 shows these high-aspect-ratio structures at the bottom of the mold. Figure 3.9 shows the resulting tip.

3.5.3 Alignment Issues

The process to create a slanted face and a vertical face involves an alignment through a 60-100 μm layer of SU-8. This distance is well beyond the depth of field in the optical system of our mask aligners at the fabrication facility. This necessitates the use of digital image capture alignment techniques and creates difficulty and uncertainty in
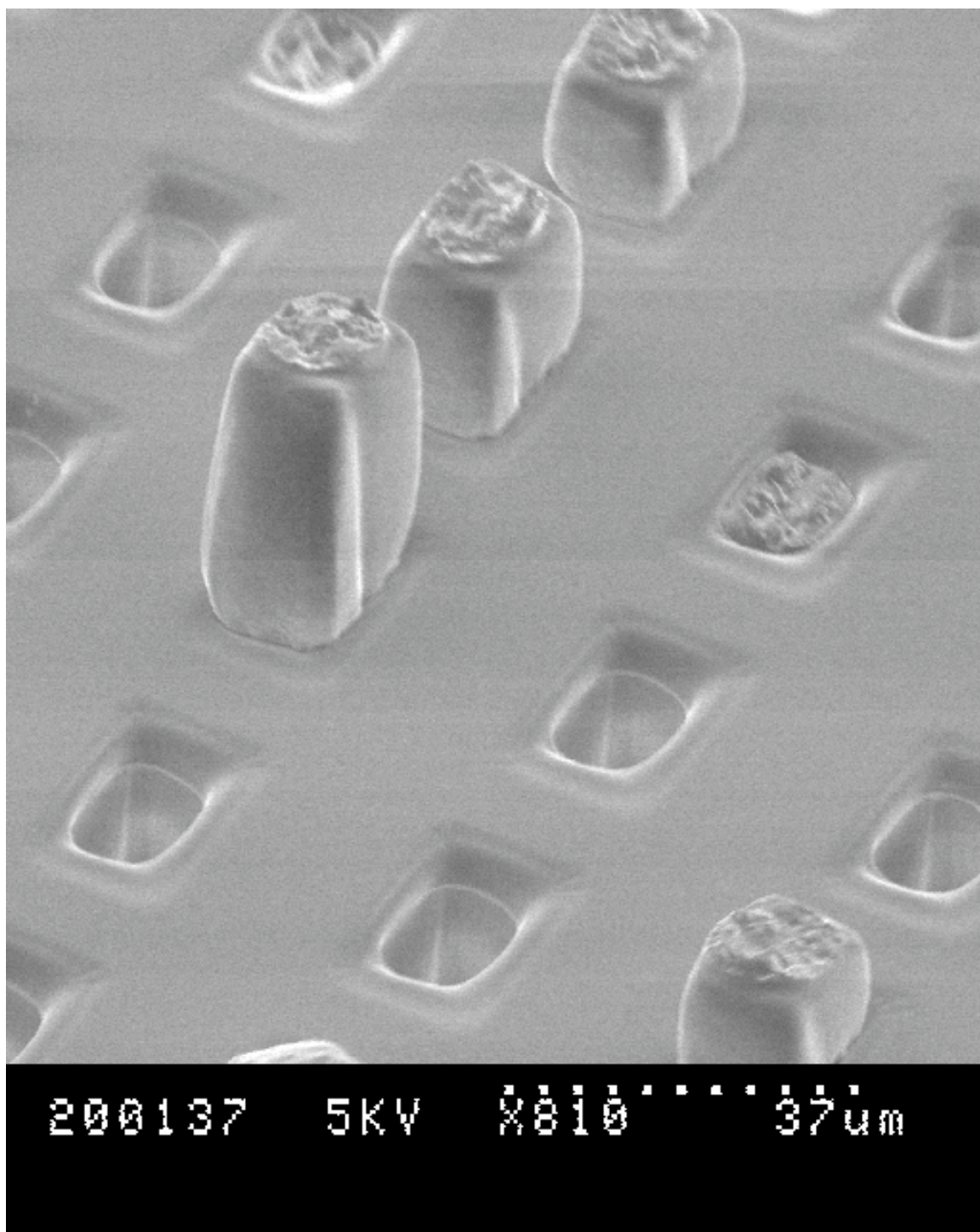
Figure 3.6: SEM image of overhanging film closing off the mold. This mold has had PDMS cast and partially released from the mold. Pillars are visible that have partially released before tearing as well as pillars that remain completely in the mold.
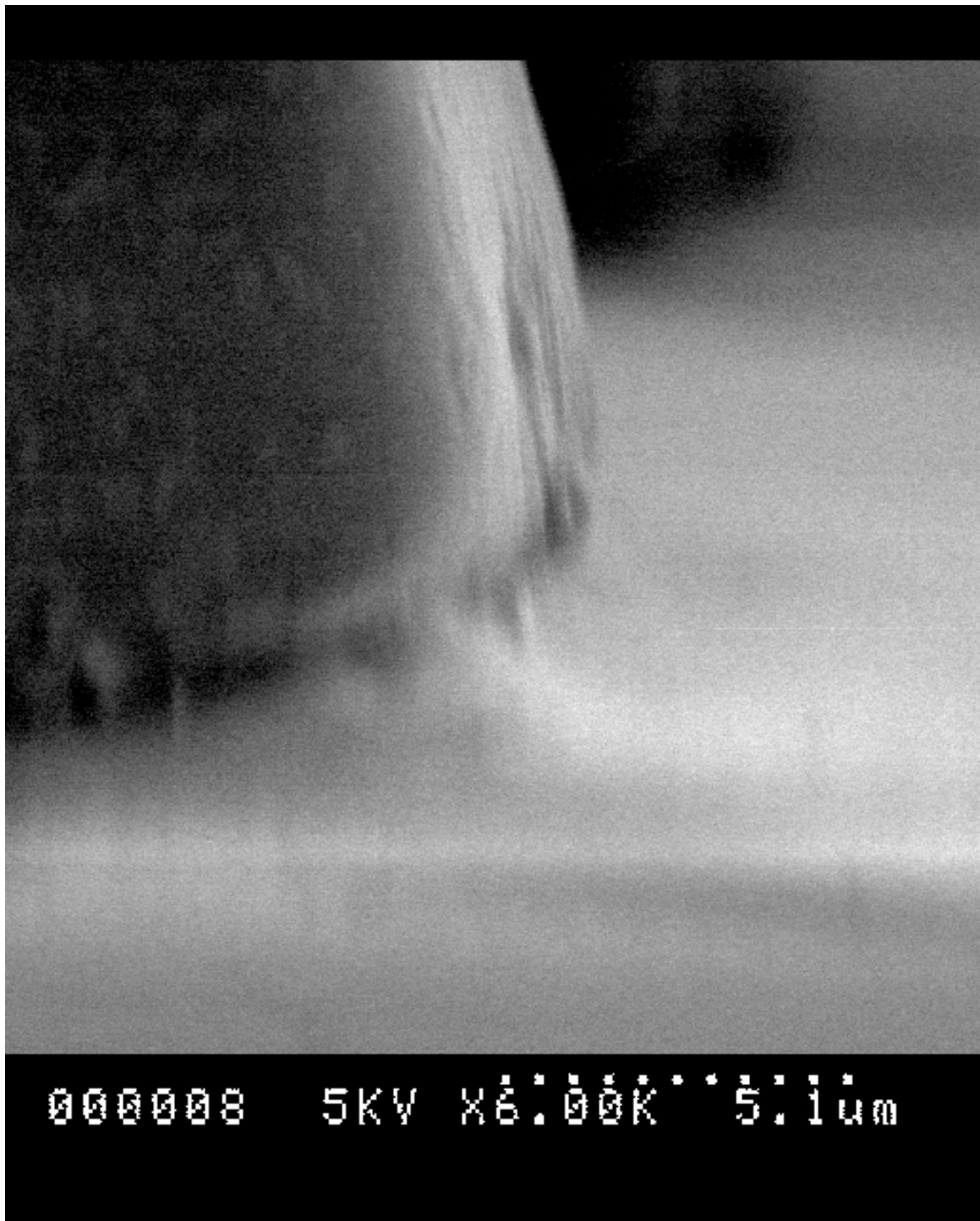
Figure 3.7: SEM detail image of the base of an adhesive pillar showing the undercut due to the overhanging film shown in Figure 3.6. This undercut affects the bending compliance of the pillar.
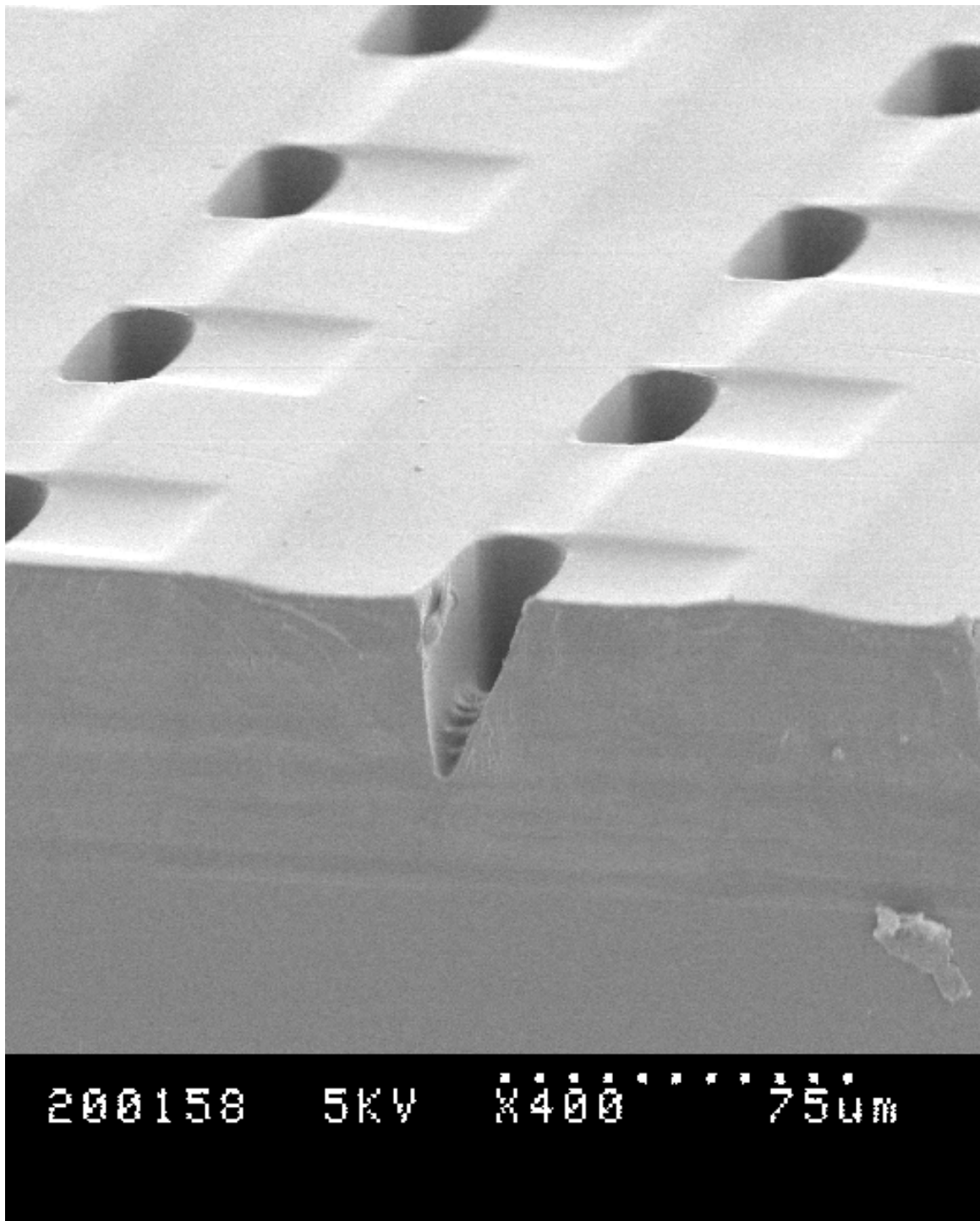
Figure 3.8: SEM image of incomplete development in the bottom of a mold cavity. Image shows sheet like structures at the tip of the mold cavity that lead to a roughened tip.
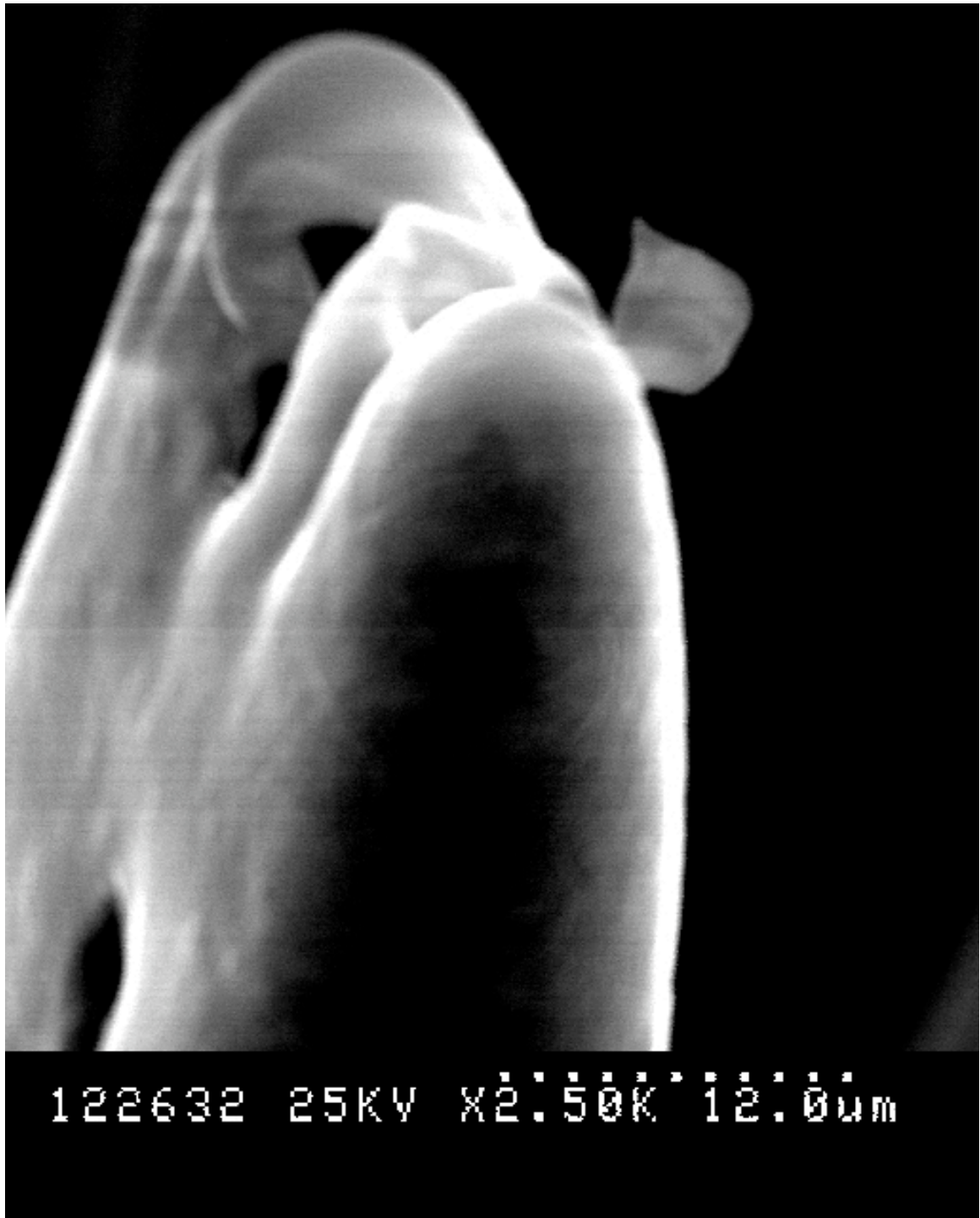
Figure 3.9: SEM image of roughened tip due to incomplete mold development.

the alignment process. The critical dimension of alignment is in the direction from the front slanted face to the back vertical face. This direction is from crown to flat on the wafer. If there is misalignment in the direction of the crown, the opening may reach the bottom of the SU-8, resulting in a truncated tip. If instead the misalignment is in the direction of the wafer flat, the mold feature will be more shallow. If the misalignment is great enough, an undeveloped region of SU-8 can be exposed at the surface. Figures 3.10 and 3.11 show what appears to be undeveloped SU-8 escaping to the surface after a misalignment. These figures also show that the feature is not as deep as expected, which is a consequence of misalignment.

3.5.4 Going Forward

This SU-8 process has provided a valuable prototyping platform for these asymmetric adhesives. It is not a robust process and the mold does not have a long lifetime since the SU-8 layer is prone to delamination and cracking. Efforts to create a mold from a more robust material would be worthwhile. There are efforts underway to explore micro-indentation as a tool. Adhesives have been attempted using micro-indentation [31] but did not yield high-aspect-ratio structures. If a robust mold could be made using this method, it would be a large benefit to the yield and reusability of the material.
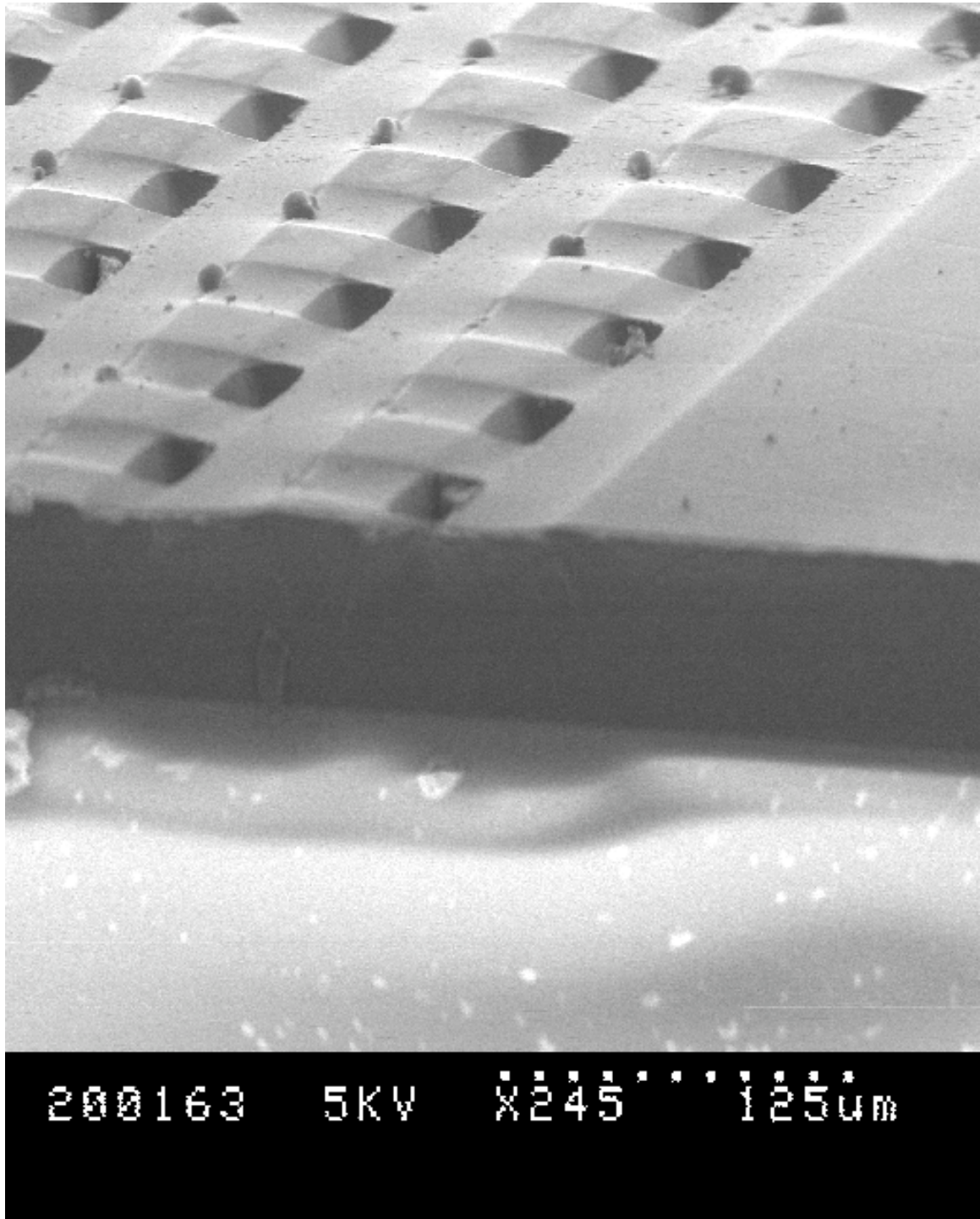
Figure 3.10: SEM image of misalignment allowing the escape of undeveloped SU-8 during the development process. Under the spherical bubbles there is a seam visible that exposes a volume of unexposed SU-8.
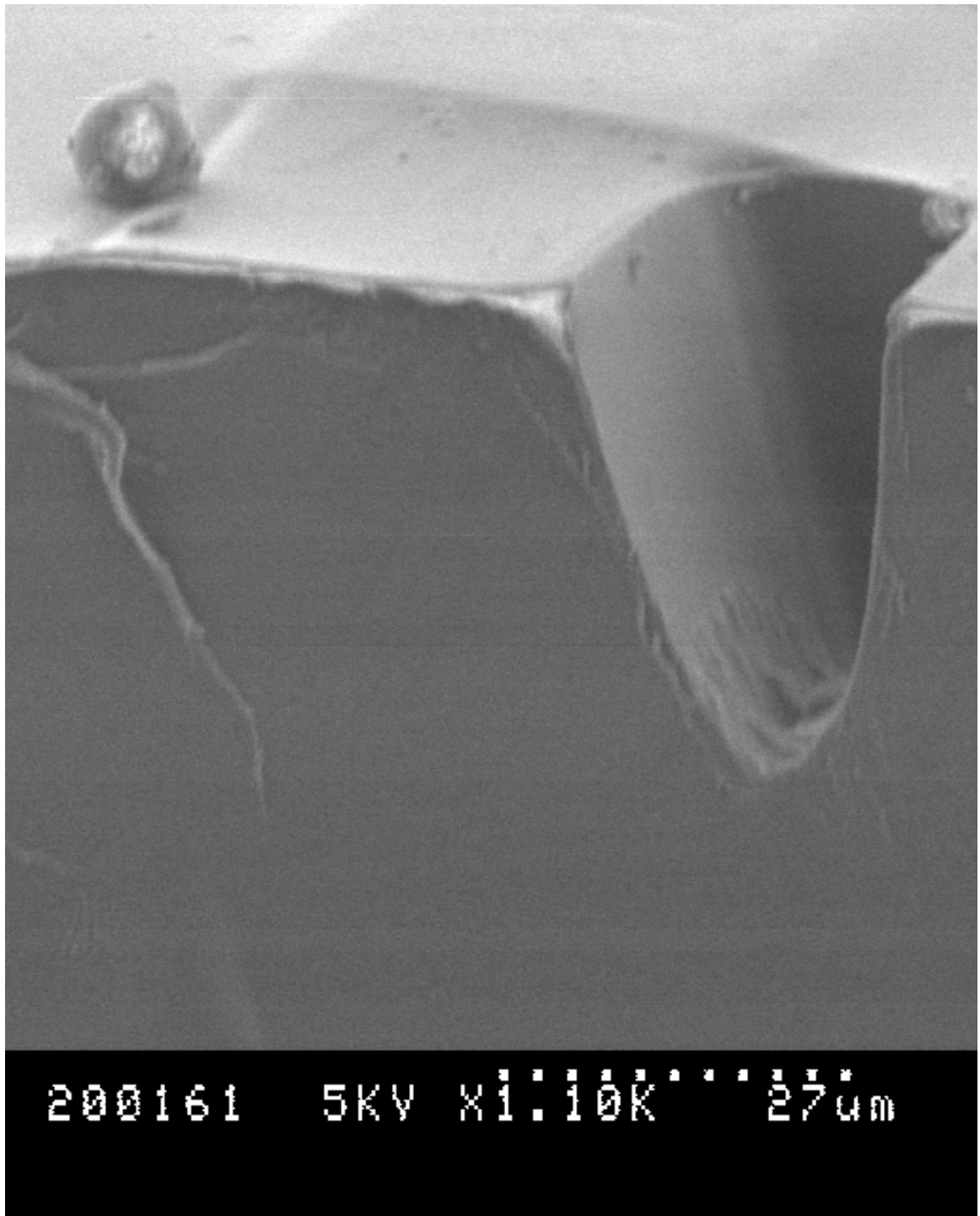
Figure 3.11: SEM image detail of undeveloped SU-8 escaping to the surface of the mold.

Chapter 4

Pillar Array Testing

The principal objective in the force testing of these adhesive arrays is to determine how the array behaves when subjected to combinations of shear and normal force. Of particular interest is the combination of shear and normal load that leads to failure of the interface. By mapping out the combinations of forces that cause failure, we can construct a region that the stresses must stay within to ensure stable attachment. Pressure-sensitive adhesives are generally applied with a compressive normal load before tensile stress is applied to the interface. We attach these fibrillar adhesives in a similar manner. This is achieved by bringing the adhesive and a surface for attachment into compressive contact to initiate the adhesive bond and then withdrawing the surface in a range of directions to create tensile stresses with varying components in the normal and shear directions. By using a force sensor that can simultaneously measure the shear and normal forces at the interface, we can determine these force pairs that bound the stable and unstable regions. These forces are plotted in a limit surface to visualize the pairs of forces for which stable attachment is possible.

4.1   Test Platform

We tested the adhesive arrays on a custom built force testing apparatus [24] with a three-axis motor stage to control friction and loading at arbitrary angles. A photo of the test apparatus can be seen in Figure 4.2 and a block diagram in Figure 4.3. The
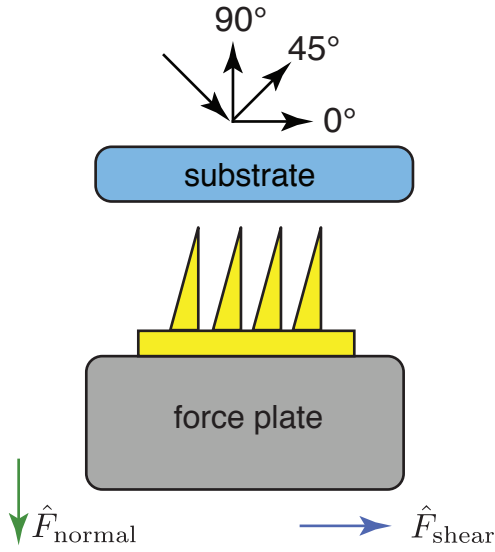
Figure 4.1: Limit surface test diagram showing the conventions for force and direction in our force testing setup. The arrows indicate the direction of positive force applied to the force plate. The unlabeled allow is meant to illustrate the direction of the substrate during the compressive phase of the trajectory. The arrows at 90° 45° and 0° are the different retraction angles for the tensile phase of the trajectory. The 90° retraction will cause mostly normal stress while the 0° will create mostly shear shear stress. These different angle and the resulting mix of normal and shear stress allow us to plot the limit curve.

setup is capable of moving a flat glass substrate and sample into and out of contact along trajectories in both the normal and tangential directions simultaneously. The apparatus consists of a 3-axis linear stage, force transducer, and 2-axis manual tilt stage. The motion stage (Velmex, MAXY4009W2-S4 and MA2506B-S2.5) has a 10 μm positioning resolution in the tangential direction and a 1 μm positioning resolution in the normal direction. A flat glass substrate was attached to the motion stage and the sample is placed upon a 6-axis force/torque sensor (ATI Industrial Automation, Gamma Transducer SI-32-2.5) with an accuracy of approximately $\pm$ 25 mN. The force transducer was mounted onto a manual 2-axis tilt stage (Newport, 30 Series Tilt Platform) which was used for manual alignment of the sample relative to the substrate. This alignment is somewhat unique since many researchers use hemispherical lenses to avoid alignment issues. Despite the difficulties that accompany alignment, we decided to use a flat surface since it best simulates the intended application of the adhesive (a climbing robot on vertical smooth surfaces). The stage was controlled by a custom microcontroller. Displacement instructions were sent from a Labview application running on a Windows XP system to the microcontroller over a serial connection. The microcontroller updated the stepper motors at a rate of 1 kHz. Force and position data were collected at a frequency of 1 kHz. Force data from the force sensor and displacement information from the stages were sent back to the Labview application and written to text files for later analysis. Data were analyzed using Matlab (The Mathworks, Inc.).

4.2 Testing Procedure

An array of adhesive of dimension $\sim$1 cm^2 was mounted on a glass slide. Since the backing of the adhesive was smooth, the backing will adhere to the glass slide. This glass slide was fixed to the load cell using a conventional tape adhesive. A camera was used to observe that the sample was coplanar with the flat glass substrate. If the sample and glass substrate are misaligned, it will be possible to have some pillars in severe compression, while not contacting other pillars. This coplanarity was difficult to achieve since the sample has non-uniform backing thickness and pillar height.
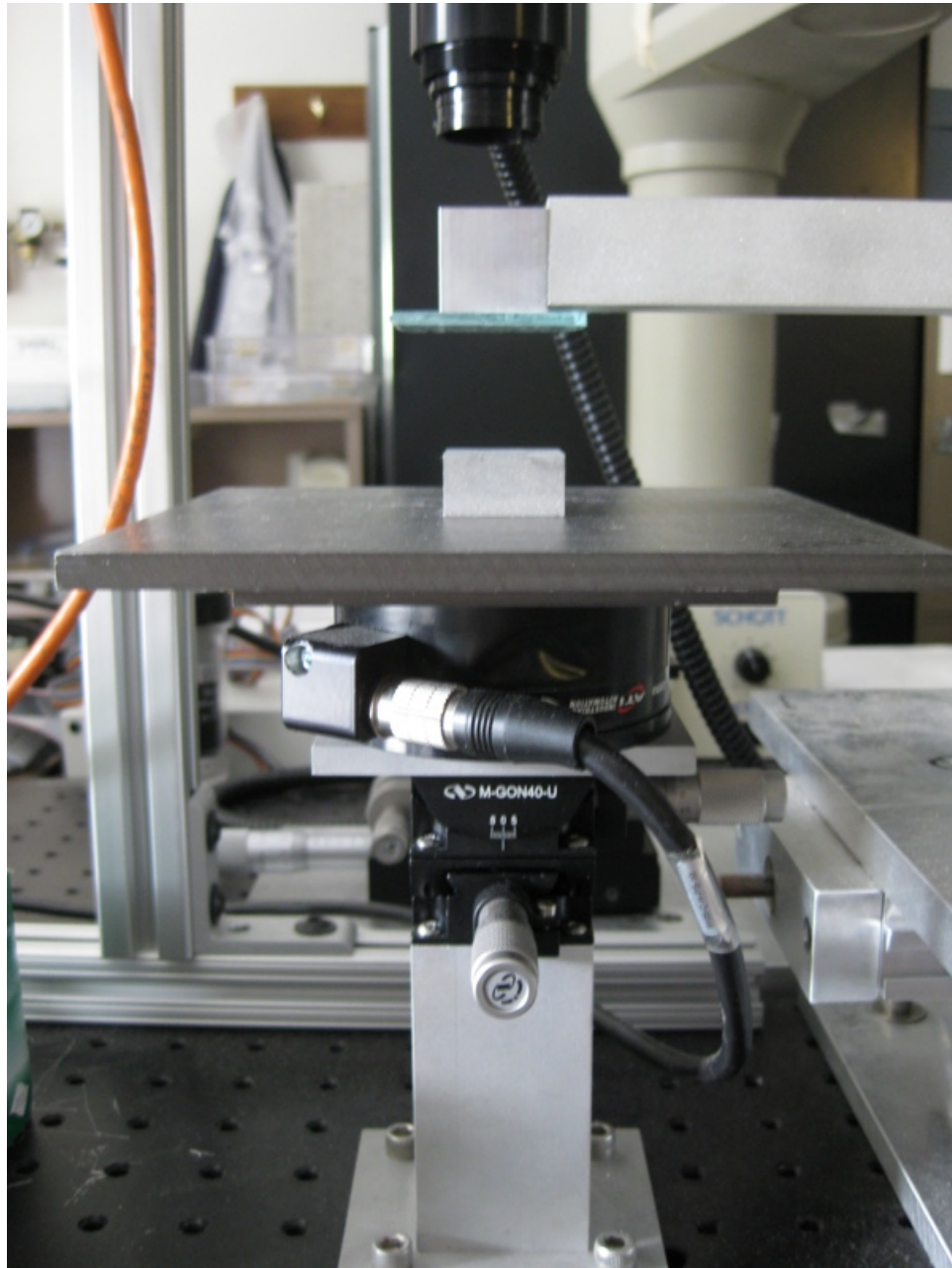
Figure 4.2: Limit surface testing apparatus. The camera objective used for alignment is visible at the top of the photo. Below the camera objective is the arm and glass plate. This glass plate makes contact with the adhesive affixed to the aluminum pedestal below the plate. Underneath the large grey plate is the load cell with the signal cable in front. The goniometers can be seen beneath the load cell atop the vertical pedestal. The arm and pedestal, while not ideal, are necessary to accommodate the large stages used for motion control.
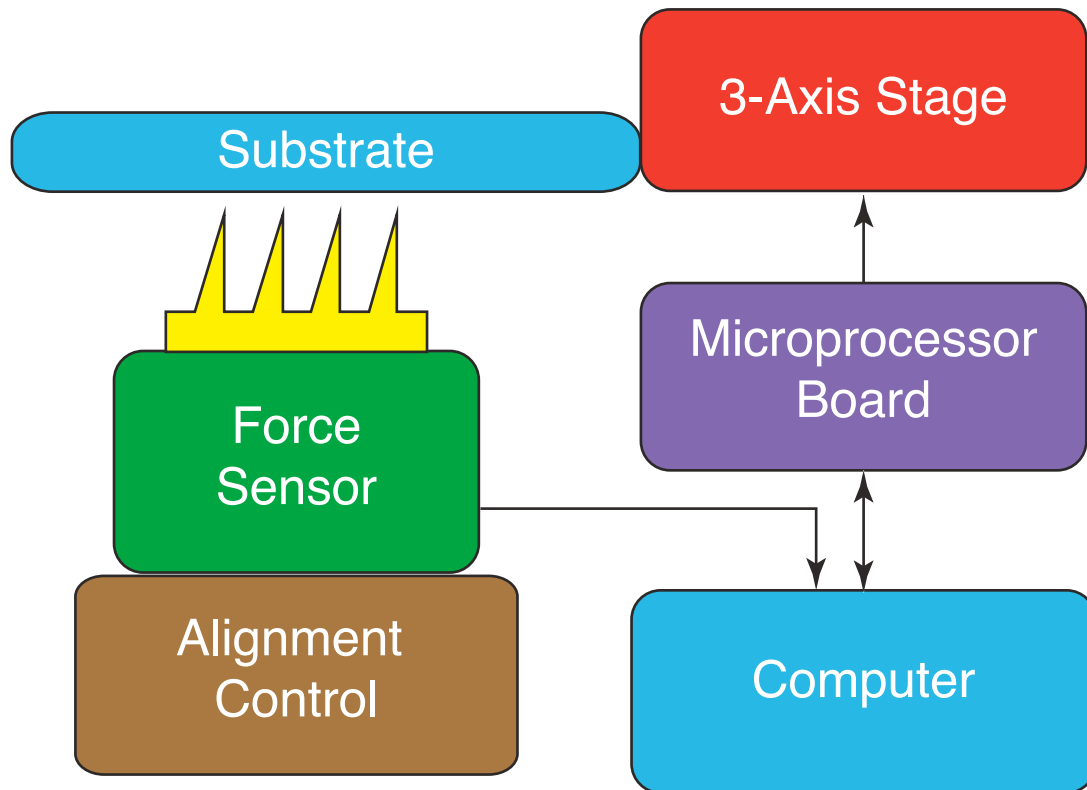
Figure 4.3: Force measurement apparatus block diagram depicting the signal flow in our system. The alignment control is manual and has no link to the computer. The computer sends locations and velocities to the custom microprocessor board which then drives the 3-axis stage. Stage encoder data for position feedback is returned to the computer through the microprocessor board. The force sensor data is fed directly to the computer. The computer runs a LabView application which coordinates the data.

Our approach was to use a camera to view the sample as it comes into contact with the glass substrate. When the wedges made contact with the glass surface the reflectivity of the bottom glass surface was enhanced and the areas of contact appear bright. The sample is brought slowly in and out of contact and when this color change occurs evenly across the sample we consider the sample aligned. We also took care to manually position the sample so that the rows of adhesive pillars were parallel to the direction of stage travel. This also was verified through the overhead camera. To specify the trajectory of compression and tension in the tests, we specified the distances and speeds at which the stage would move in software. These instructions were stored in the LabView application to be sent to the microcontroller at run time. With the sample fixed and aligned and the trajectories specified, the test apparatus runs and collects data. Figure 4.1 shows the angles and axes of the forces measured relative to the adhesive and the force transducer. These tests were displacement controlled. The amount of compression was specified by the distance that the stage travels in the normal direction after the initial contact. This initial contact position was defined as the point at which normal force due to compression is recorded. Generally the maximum compression distance was on the order of half of the pillar height, in this case approximately 40 microns. Once compression was finished, the glass surface was withdrawn at a velocity of 1000 μm/sec.

4.2.1   Data Analysis

Data was compiled, scaled, and then plotted. A plot of the data as collected looks like Figure 4.4. Failure points were identified using the max-power method [32]. The max power method defines the point during tensile loading where the dot product between the interface force and the velocity of the glass stage is a minimum. That is, t_f, the time of the failure is defined to be

$$\boldsymbol{F}(t_f) \cdot \boldsymbol{v}(t_f) \leq \boldsymbol{F}(t) \cdot \boldsymbol{v}(t), \forall t. \tag{4.1}$$

The shear and normal forces at the identified failure point were recorded for each of the trajectories. When we look at the data we see that failure is usually indicated

by changes in the slope of the force vs. time curves during the tensile phase of the trajectory. These changes in the force indicate transitions from static to kinetic or dynamic friction and release events. Figure 4.4 shows a failure when the substrate was withdrawn at an angle parallel to the interface (0° according to Figure 4.1). The black x marks depict the failure point predicted by the max power criterion. There are slope changes before the failure point shown but these slope changes were during the compressive phase and do not represent relative movement. The force trace plot (Figure 4.4) allows us to see the forces exerted by the adhesive as a function of time. The plot shows that dynamic sliding adhesion is obtained where despite slipping, both shear and normal adhesion forces are exerted. In this test, the adhesive was able to simultaneously maintain 2 kPa of adhesion and 8 kPa of shear. This implies that individual hairs that have detached are able to reattach and exert adhesive force. This property allows the adhesive a graceful failure mode desirable for robotics or locomotion applications. Other GSAs have demonstrated similar results using a spherical surface with a radius of ~5 mm [15]. These tests using spherical glass surfaces don't necessarily demonstrate the reattachment of fibrils since only a portion of the sample's fibers are in contact. This is in contrast with the testing described here, where the glass surface has a larger area than the adhesive sample and all the adhesive fibers are available for adhesive contact.

Figure 4.5 shows the force trace when the substrate is drawn vertically away from the microwedge adhesive (90° according to Figure 4.1). In this case the failure point predicted is not at the precise moment of the failure, but the forces reported are essentially the same. This is a minor shortcoming of the max power method. We inspected the data to be sure that each of the failure points reported appear to be correct. To construct the limit curve, the adhesive is tested at multiple compression depths and angles of withdrawal. Three tests are conducted at each compression depth and angle. The failure points are computed in each of these tests and compiled to construct a limit curve.
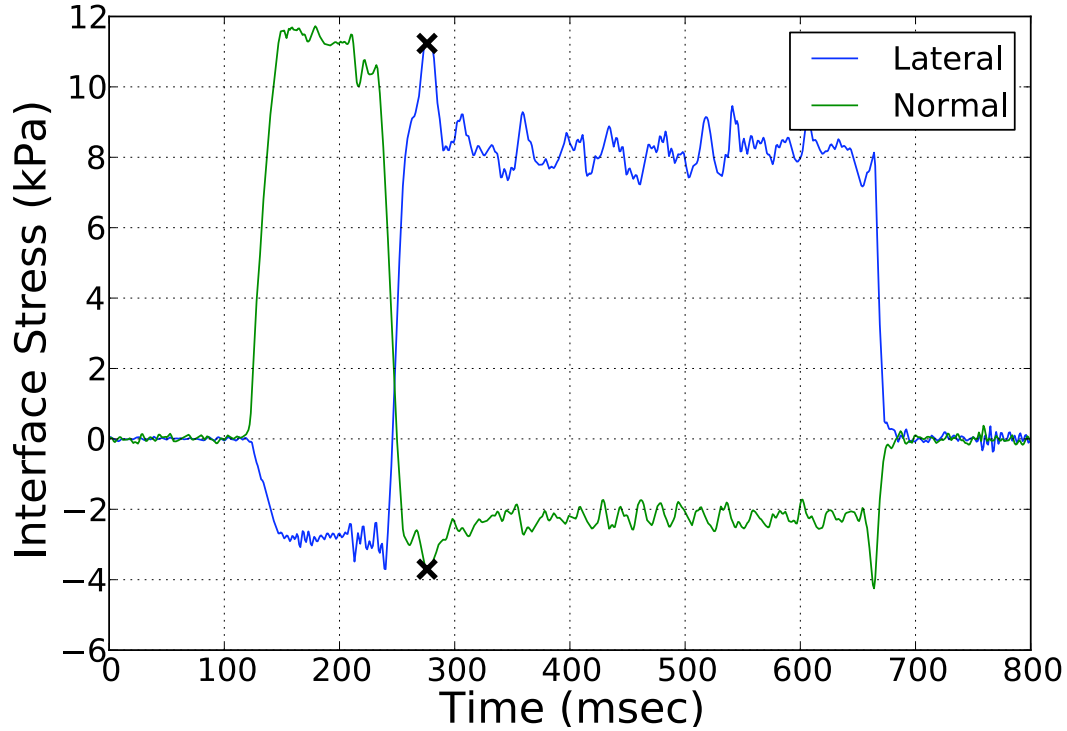
Figure 4.4: Adhesive array force trace with parallel (0°) retraction. The normal trace shows the initial compression phase followed by a region of adhesion during the parallel drag. In the shear trace, we see that there is a shear force created by the adhesive at the same time as the normal adhesion force. The failure point occurs at the black x mark. At the time of failure, the shear (lateral) and normal forces are recorded and plotted as a pair in the limit curve.

4.3   Results

Figure 4.6 shows the resulting limit surface from a fibrillar adhesive sample. The limit surface in Figure 4.6, obtained through many trials over a range of preload angles, preload depths, and exit angles, is a map of the release points for different shear to adhesion ratios. We notice that the surface crosses the origin and has a negative slope as it leaves the origin. As discussed in Section 2.2.4, this negative slope indicates that the normal stress capacity of the adhesive is increased by the application of shear stress at the interface. The limit surface also shows that force
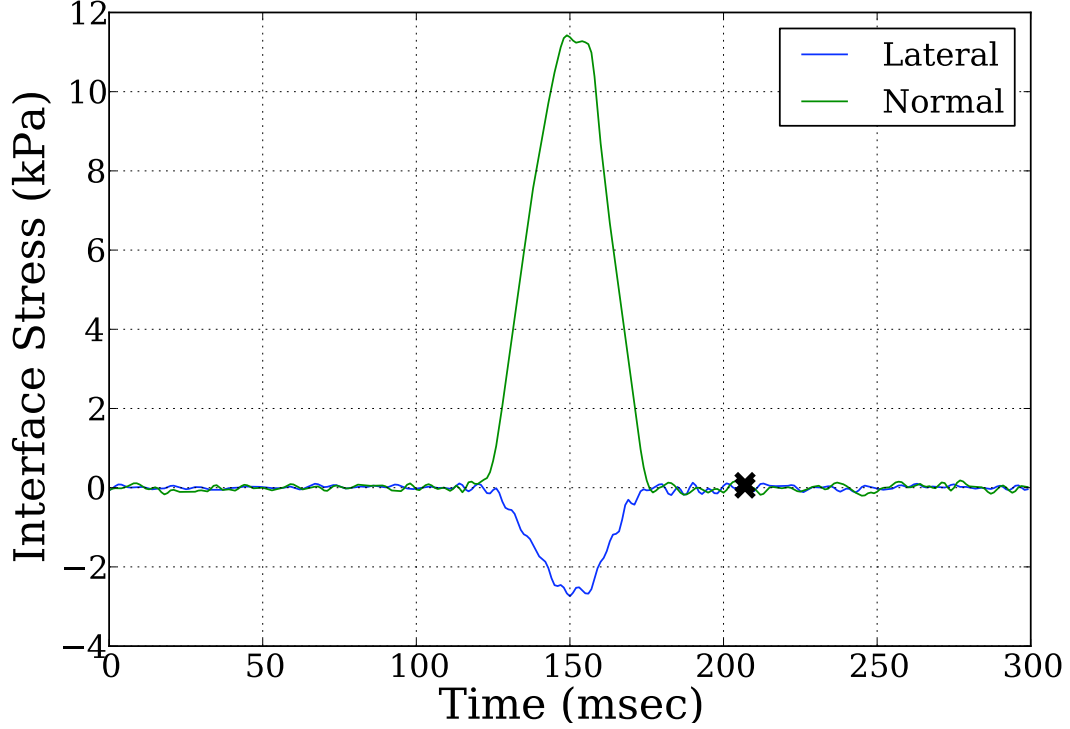
Figure 4.5: Adhesive array force trace with vertical retraction. The compression phase can be seen in the normal trace beginning near 120 msec and ending near 150 msec. During the tensile phase, this force is reduced and falls to zero. We see that the stresses during the retraction or tensile phase in this case are primarily in the normal direction. It is also clear that at the time of failure there is little or no adhesive force (negative normal interface stress).

pairs very close to the origin can result in detachment. This means that when the shear stress is removed from the interface, the adhesive can be removed with very little force. The increase of normal force with the application of shear force saturates at a shear force corresponding to ∼13 kPa of shear stress. Above this level, the normal holding power is reduced and at ∼18 kPa of shear stress, the interface can only be maintained if there is compressive normal force at the interface. A more detailed discussion of these array results can be found in [33] and [34].

As a control, we tested a flat thin sample of PDMS rubber to determine its limit surface. The limit surface of the flat control in Figure 4.7, shows behavior similar
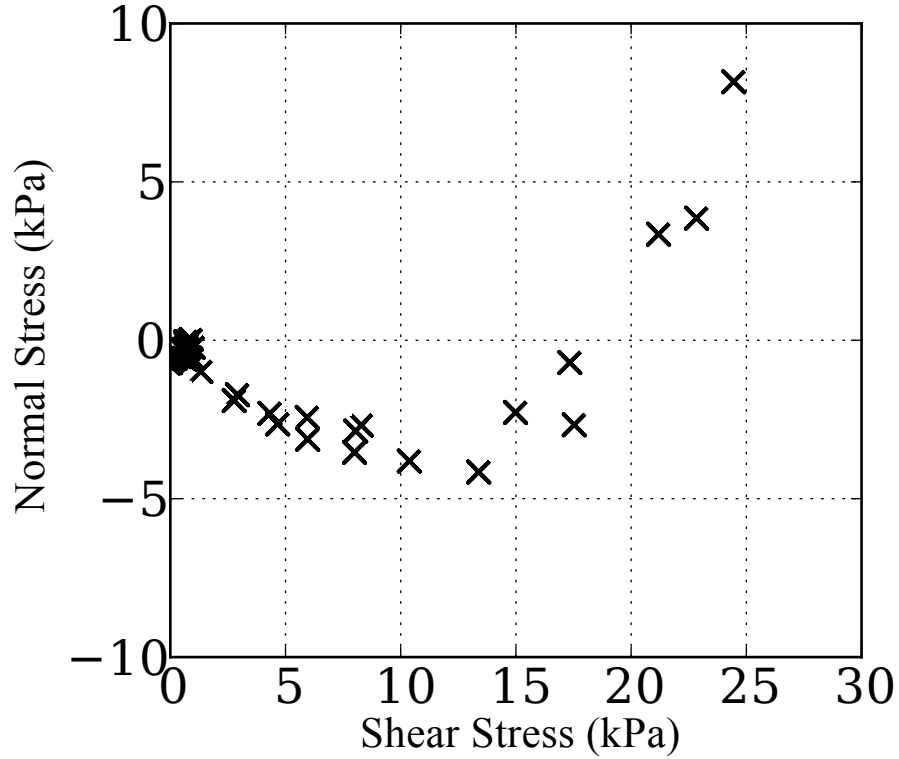
Figure 4.6: Limit curve for adhesive pillar array. Each plot point represents an adhesive failure. The points in force space above the line described by the pairs are stable while points below the curve will detach. We see that the adhesion is increased as the shear increases. Also, if the shear is decreased to zero, the adhesion is reduced and the adhesive can be removed with very little force.

to the embedded cone model (discussed in section 2.2.2) where increasing shear decreases the available normal force. Also, the limit surface of the flat control does not pass through the origin. This implies that there must be a normal force exerted at detachment when there is no shear and that there is no detachment possible without the application of tensile stress to the interface. It should be noted that the maximum normal stress achieved is 2 times greater for the flat control sample. This reminds us that our choice of adhesive depends on the specific behavior we desire.
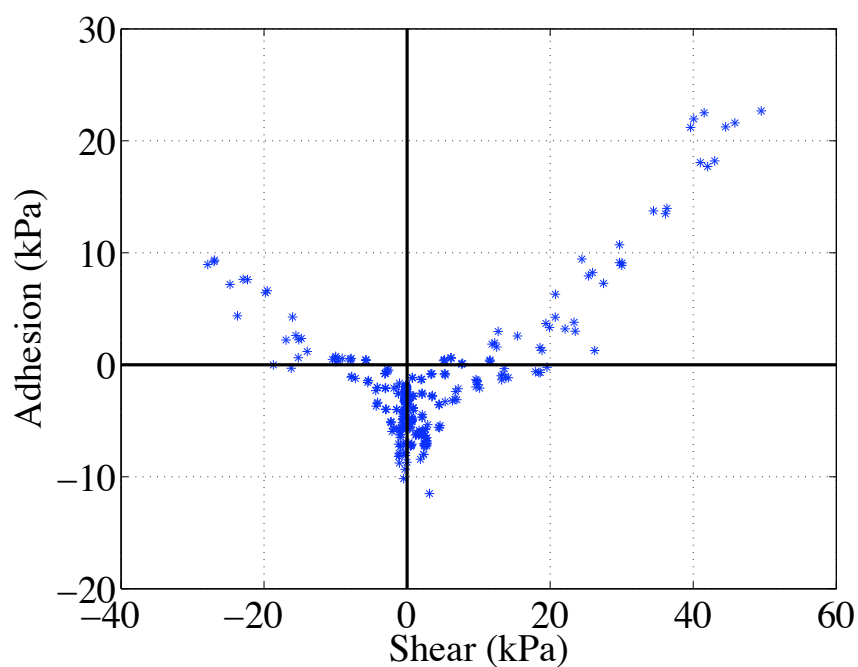
Figure 4.7: Limit curve for PDMS flat control sample. We tested the material used for the adhesive pillars by creating a flat sample and testing. Each plot point represents an adhesive failure. This curve has a different character than Figure 4.6. This limit curve does not intersect the origin and increasing shear leads to diminished adhesive capability.

Chapter 5

Single Pillar Testing

This chapter describes the testing performed on single isolated pillars from the adhesive arrays. In Chapter 4 the adhesive properties of arrays of tapered adhesive pillars are discussed. Having accumulated this body of data on the behavior of these pillars in arrays, we became interested in the behavior of single elements. We set out to determine what aspects of the adhesive behavior are intrinsic to the wedge structures and what aspects are emergent in these large arrays. To measure the behavior of single isolated pillars, we use a system with similar capabilities to the array testing system, but with μN force resolution. This system allows us to observe behavior that is not evident in arrays of thousands of pillars. We also performed testing of nontapered pillars to understand the role that the pillar shape plays in the adhesive properties.

5.1 Force Measurement System Description

5.1.1 Dual Axis Cantilever

The central part of this force measurement system is a force transducer capable of μN resolution force measurement. In the array testing apparatus we used a commercially available force sensor with mN resolution. In this case, the force sensor is a dual-axis micromachined force sensor as described in [35, 36]. This flat-tipped piezoresistive
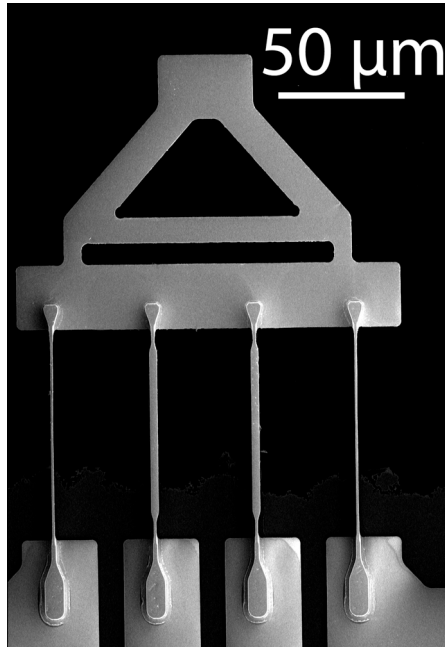
Figure 5.1: SEM image of dual-axis cantilever. Normal force is in the out of plane direction. The normal force piezoresistors are located in the two short members at the base of the triangular tip. The shear force is in the horizontal direction. The four slender structures deflect together. The shear force piezoresistors are located at the base of the inner two structures. The thickness is reduced in those areas to concentrate the stress.

cantilever is capable of simultaneously measuring forces along two orthogonal axes to measure the forces at the adhesive interface. An electron microscope image of a representative cantilever is shown in Figure 5.1. This sensor is a microfabricated silicon cantilever with implanted piezoresistive regions that form strain sensors that change resistance when the cantilever is deflected. These piezoresistive regions are depicted in a rendered illustration of the cantilever in Figure 5.2. It is similar to an atomic force microscope (AFM) cantilever but instead of a sharp tip, this sensor has a 20 μm by 40 μm platform for the pillar to adhere to and its unique geometry enables simultaneous detection of normal and shear forces applied at the tip.

The change in resistance is sensed by a Wheatstone-bridge signal-conditioning circuit and converted to a voltage. The structure is designed so that the members
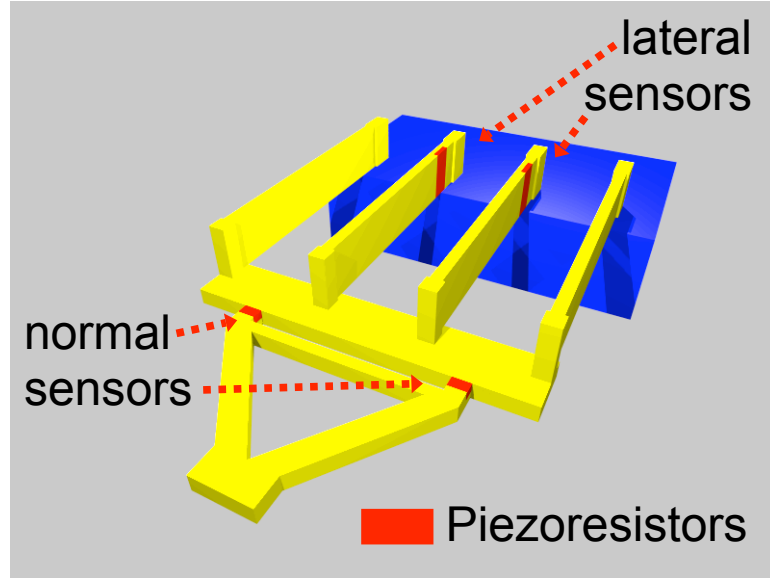
Figure 5.2: Rendered illustration of the dual-axis cantilever. The locations of the normal and lateral force piezoresistive sensors are indicated on the illustration.

used to sense normal forces are stiff in the shear direction and vice versa to minimize crosstalk between the two axes. To calibrate the sensor, we measure the displacement sensitivity of the cantilever and signal-conditioning circuit directly, and then estimate the cantilever's stiffness using a combination of resonant frequency measurement, finite-element modeling, and interaction measurements with a reference cantilever [37]. The spring constants of the cantilevers vary from 0.3–0.6 N/m in the normal direction and 0.3–3.0 N/m in the lateral direction. The values of these stiffnesses of the two cantilevers most often used for this testing are shown in Table 5.1. It is important to note that these stiffnesses are within an order of magnitude of the corresponding stiffnesses of the pillar structures. This is in contrast with the array testing setup where the difference between the normal stiffness of the array and the force plate is about a factor of 200. When the data is interpreted, special attention must be paid to account for the deflection of the dual-axis cantilever during testing since the compliances are similar.

Cantilever	k_N (N/m)	k_S (N/m)	s_N (V/μm)	s_S (V/μm)
529b02	0.659	3.898	0.224	1.148
629a03	0.313	0.307	0.148	0.473

Table 5.1: This table shows the stiffnesses and displacement sensitivities for the cantilevers used in these measurements. k_n is the normal spring constant of the cantilever and k_l is the lateral or shear spring constant. s_N is the normal sensitivity of the cantilever circuit at the nominal gain and s_S is the shear sensitivity.

5.1.2 Force Measurement System

The measurement is performed in a method very similar to the array measurement. We have tilt stages for alignment, an actuated stage for positioning, and a force transduction element. To characterize the adhesive properties, we determine the set of shear and normal force pairs for which stable attachment is possible. A photograph of the system is provided in Figure 5.3.

The stage that provides motion is a piezoelectric actuator (P-731.20, Physik Instrumente). Typical load drag pull trajectories are executed and the resultant forces are stored on a computer for analysis. These plots show the normal and lateral forces on the dual-axis cantilever during contact with the adhesive pillar.

The adhesive pillar and cantilever are placed in a custom system that allows for alignment of the pillar and cantilever, motion control, and force data collection. The dual-axis cantilever is mounted to a piezoelectric stage (P-731.20, Physik Instrumente) with capacitive position sensors (E-509.C2, Physik Instrumente) to provide micron-scale positioning of the cantilever relative to the fibril under test. The cantilever is mounted and wirebonded to a surface-mount breakout board and a cable was attached. These leads are sent to a signal-conditioning circuit based on a Wheatstone bridge to monitor the resistance change in the piezoresistive strain sensors. A data-acquisition board (PCI-6052E, National Instruments) is used to output the analog signal to the piezoelectric stage and to acquire the analog signals from the capacitive position feedback and the Wheatstone bridge. These signals are controlled and tabulated by a software application (Labview, National Instruments) running on a desktop computer running Microsoft Windows XP. Figure 5.4 provides a schematic
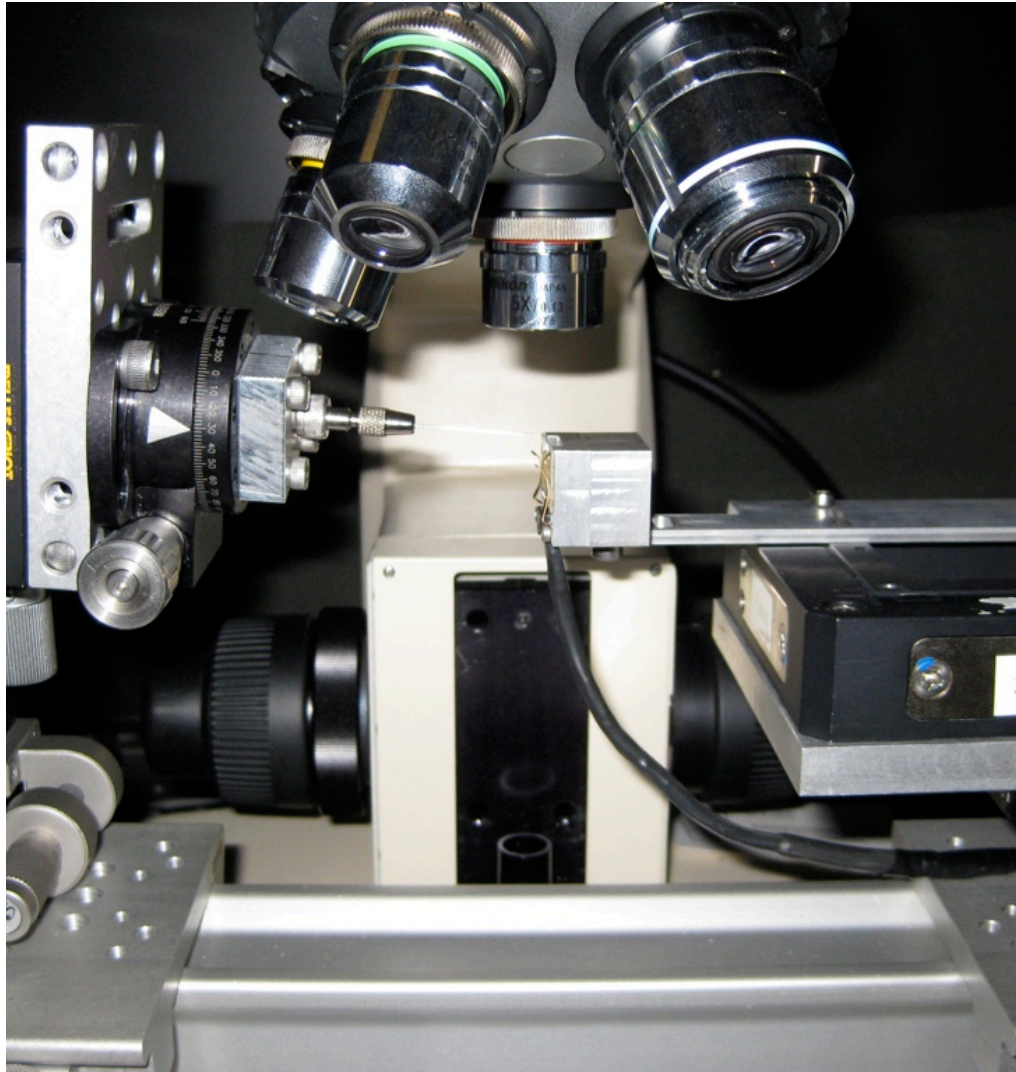
Figure 5.3: The force measurement apparatus for single adhesive pillar measurements. The microscope objective for viewing is at the top of the photo. The black box on the right is the piezoelectric stage. The aluminum arm and block holds the cantilever and circuit board at the center of the photo. The black wire runs the signal back to the signal-conditioning circuit. On the left are the positioning stages to allow for six-axis positioning relative to the cantilever surface.
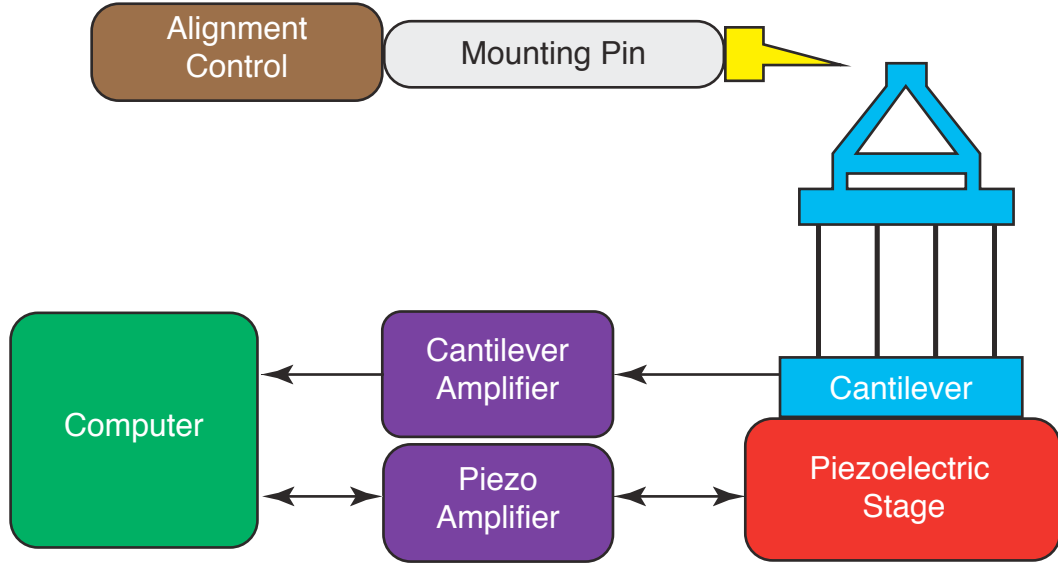
Figure 5.4: Single adhesive pillar apparatus block diagram.

representation of these connections.

The adhesive is mounted at the end of a steel pin. The pin holder has five degrees of freedom to provide alignment and adjustment relative to the plane of the cantilever tip. Any adjustments needed in the sixth degree of freedom are made by gently bending the mounting pin.

5.1.3 Sample Preparation

Isolated stalks were mounted using two different sources. The first sources were molds that, owing to clogging and other degradation, had sparse coverage of stalks when cast. We later fabricated molds that had custom fabricated stalks with sufficient spacing to make manual isolation simpler.

Using either of these types of molds, isolated hairs are identified and then cut from the backing using steel razor blades that are cut and ground to allow for better

viewing under the dissection stereomicroscope. Sample sizes are on the order of 200 μm by 200 μm. For mounting, a steel pin was prepared by tapering the flat side of the pin until the tip diameter was on the order of the sample size. Cyanoacrylate adhesive was used to fix the pin to the sample. Samples were allowed to cure for at least an hour before testing. A mounted sample and the dual-axis cantilever are shown in Figure 5.5.

5.1.4 Limit Curve Test

A single pillar limit curve was plotted by performing multiple trajectories on a single wedge that simulate loading of the adhesive under use. By withdrawing the cantilever at different angles, we can achieve varying ratios of normal to shear adhesive force and can map out a limit curve.

Figure 5.6 shows the relative orientations of the cantilever and pillar, the convention for forces on the cantilever, and the directions of pillar motion during the test. The cantilever approaches the tip, makes contact, and applies compressive stress to the interface. In these tests, we apply compressive forces of 1–5 μN. After the compression phase, the cantilever is withdrawn from the pillar along a straight line at an angle θ to the cantilever surface (Figure 5.6). The angle θ varies from 0° to 90° to provide loads varying between primarily normal and primarily shear. For high shear loads, the pillar is deflected and the side of the pillar contacts the substrate. We find the forces present at the moment of failure by analyzing the force trace data (Figure 5.7). The stresses at the interface increase until the interface breaks, at which point the measured forces either decrease rapidly or level off. Failure can be either a vertical detachment from the surface or a slipping failure while the pillar is still in contact.

A typical plot of the shear and normal force data can be seen in Figure 5.7. As in the array testing, we look for failure events where the force vs. time plot undergoes an abrupt change in slope after the accumulation of force at the interface. These failure points are initially determined by looking at the maxima and minima of the normal force data. We do not use the power method to determine the failure point. In these tests, the stiffnesses of the force cantilever are comparable with the stiffnesses of the
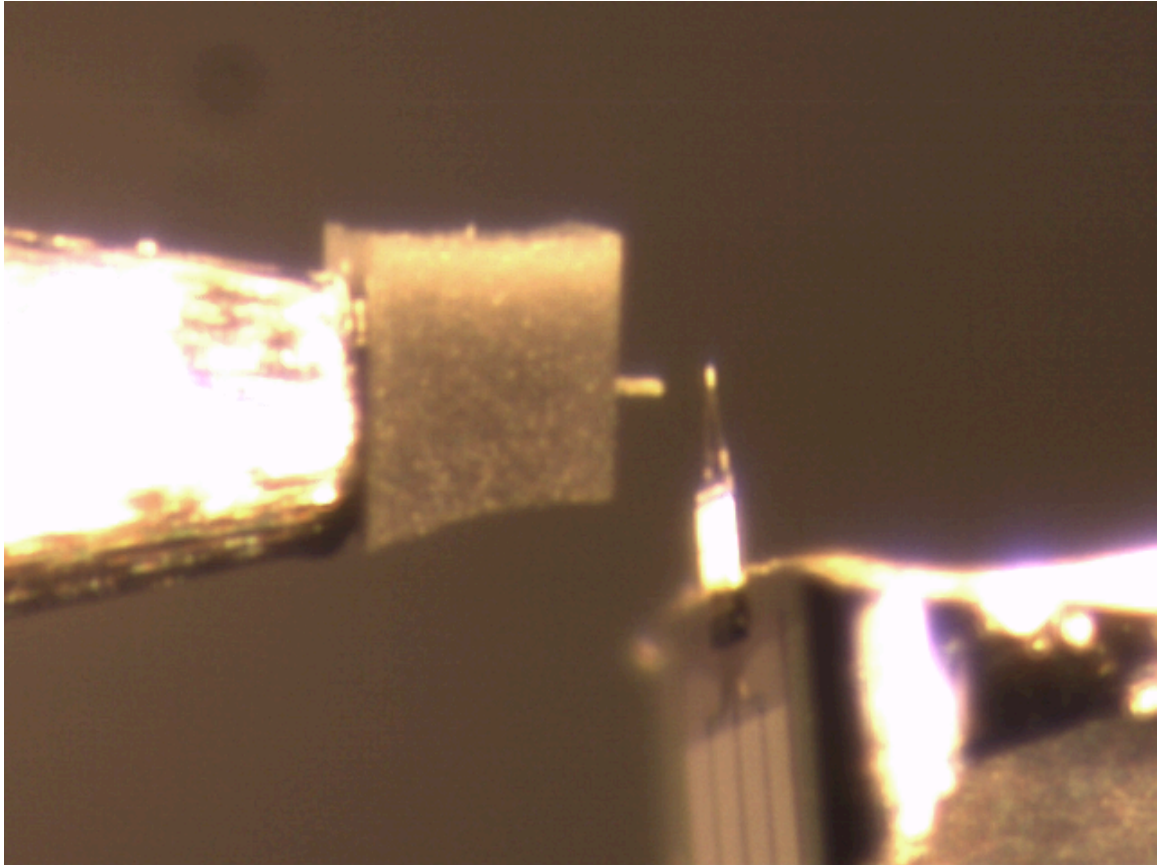
Figure 5.5: Profile image of single adhesive pillar and force cantilever. The mounting pin is visible on the left of the image. The texture on the pin is from shaping the pin to fit the PDMS sample. The block of PDMS is in the center of the photo with a single pillar protruding from the right side. The cantilever and die are in the lower right of the photo.
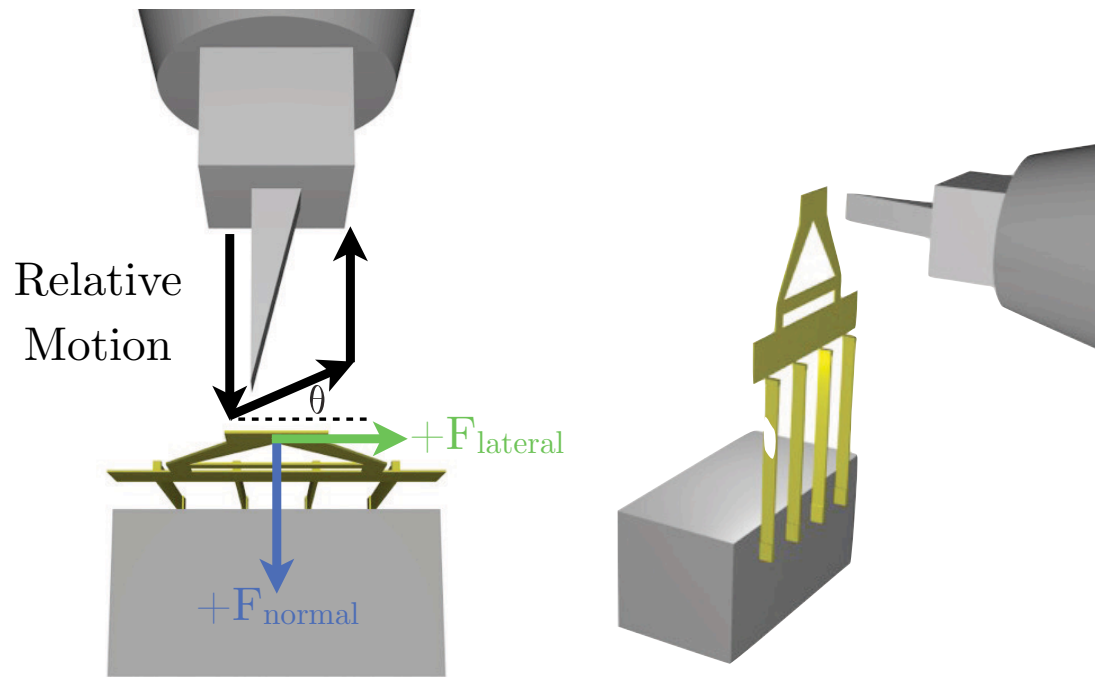
Figure 5.6: Diagram of mounted pillar and force-sensing cantilever. The black arrows indicate the relative motion of the pillar and cantilever. The blue and green arrows indicate the direction of positive forces exerted on the cantilever. This convention is used in the force plots.
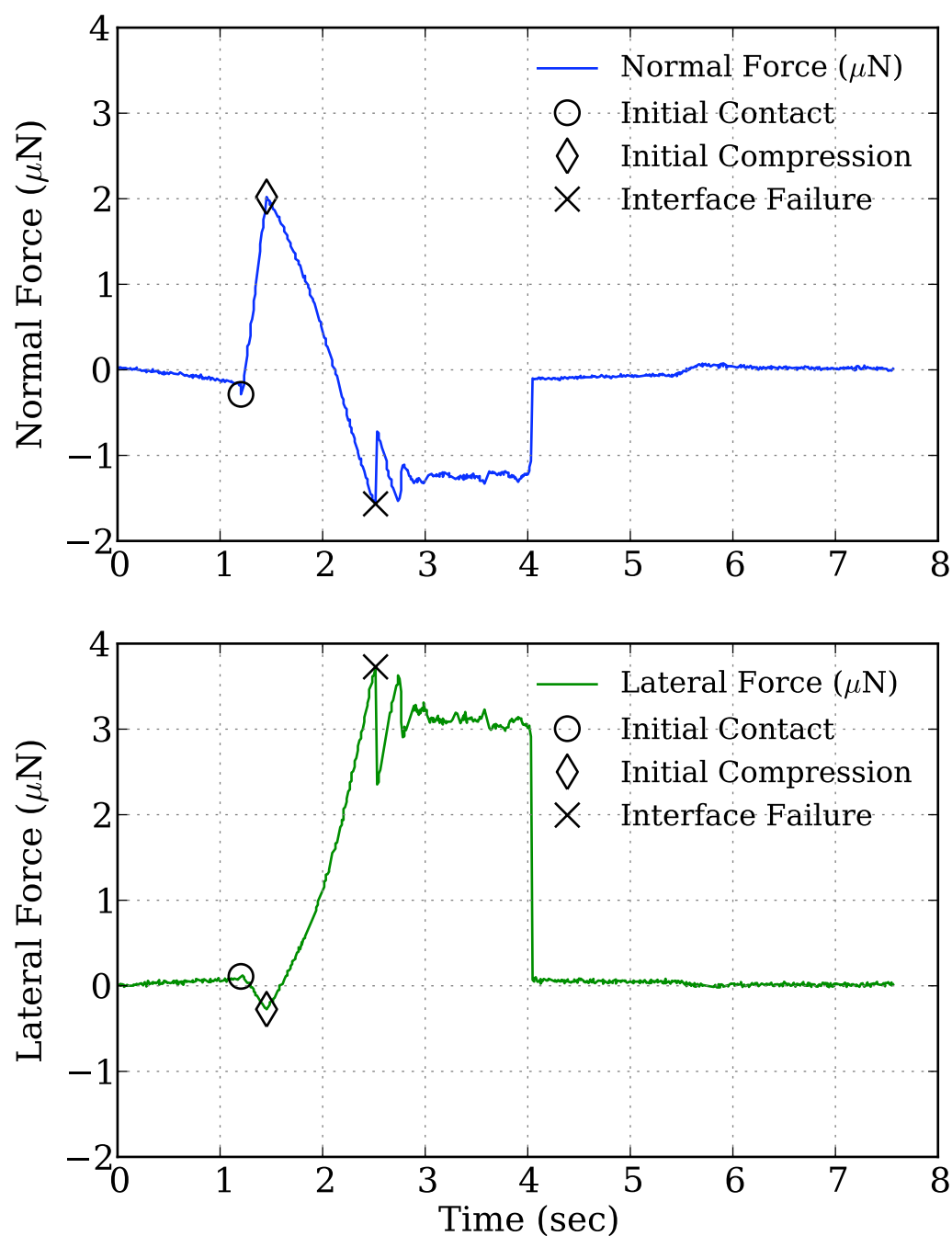
Figure 5.7: Single pillar force trace. This test is similar to the force traces performed in the previous chapter on adhesive arrays. The failure in this test is performed as a sliding test that will generate more shear than normal force. Notice that after the initial failure that there is a reattachment event.

adhesive pillar. Because of this condition, the velocity of the stage and the velocity of the substrate are different. In the case of the array measurements, the force plate was much stiffer than the array and the velocity of the stage could be equated with the relative velocity of the adhesive backing and the substrate. We then examine these points and if they appear incorrect, we manually determine the points by inspecting the force traces for slope discontinuities using a graphical user interface coded in python (Enthought Python Distribution, Enthought, Inc.). By using these points for all the different loading conditions, we create a limit curve.

The normal and shear forces at these failure events are plotted as points in force space with normal force on the vertical axis and shear force on the horizontal axis. These force–time traces are collected for a variety of tension trajectories. The compiled force time traces are analyzed to find the shear and normal forces at the release event. We take the set of shear and normal forces at release and plot them. When these points are plotted together, they create a limit curve [38] that separates force pairs with stable attachment from force pairs that will detach.

5.2   Data Collection and Analysis

5.2.1   Piezo Drift

As the cantilever approaches the adhesive pillar, the normal force signal experiences a significant drift. The adhesive pillar material, PDMS, is a dielectric material and we expect uncontrolled static charge on the surface. Electrostatic attraction has been ruled out as a possible cause since the sign of the drift remains the same when the cantilever is reversed. Figure 5.8 shows this signal drift when the cantilever is approached from the front as well as from the back. Although the signal of the cantilever being pushed and pulled is in the opposite direction, we see that the drift is in the same direction. This implies that the signal drift is not electrostatic attraction deflecting the cantilever. Grounding the mounting pin did not improve the drift. We did not test to see if coating the sample in a conductive material would improve the drift. Also, a pin without PDMS on the tip did not cause a signal drift. One possible
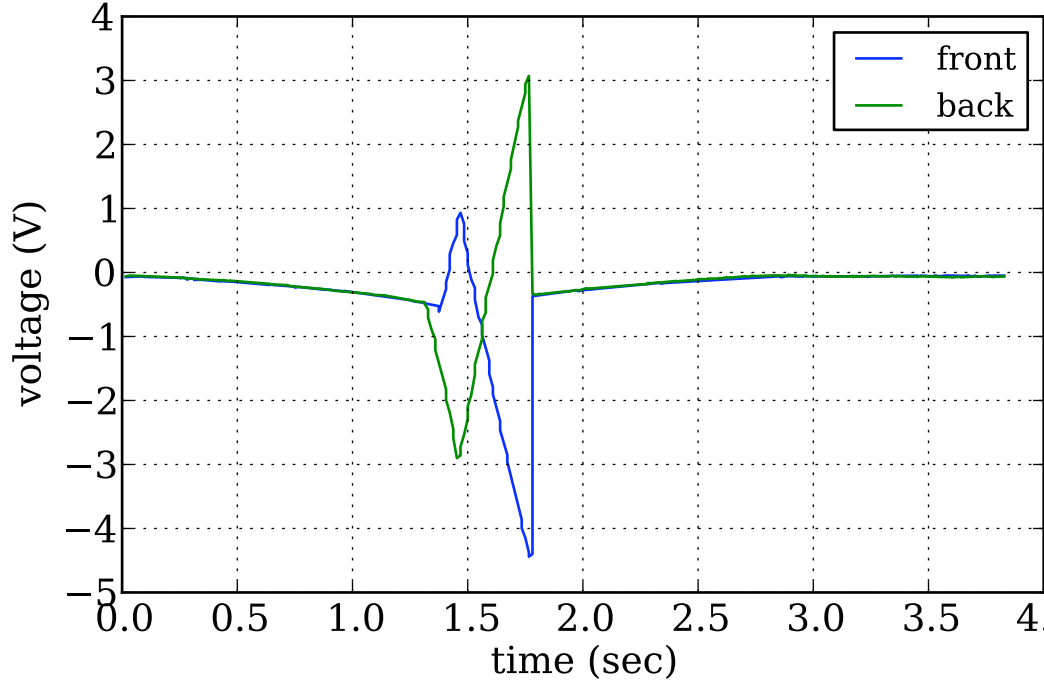
Figure 5.8: Reversal Test of Cantilever. Cantilever was approached from front and back side of cantilever to determine if electrostatic attraction was the cause of the signal drift.

explanation is that the PDMS is affecting the implanted piezoresistors in a manner similar to the gate on a field-effect transistor. This drift is a well-behaved function of the distance between the sample and the cantilever. To account for its effect, the voltage immediately before contact is treated as the zero point and subtracted from the force voltage signal.

5.3   Results

These limit curve tests give us two ways to look at the behavior of the adhesive pillars. The time-domain tests showing the force data allow us to see how the adhesive behaves while in contact. We can see at what force the pillar fails and how the pillar behaves during that failure. The force-domain limit curves allow us to determine

what combinations of forces allow for stable adhesion. We will discuss each of these below.

5.3.1   Time Domain Force Trace Results

There is an interesting contrast in the adhesive behaviors of the array and the single element in these similar tests. In the array, we observe a sustained level of adhesion and shear while the adhesive is experiencing a sliding failure. The single terminal structure sometimes displays large changes in adhesion during dragging which indicate events of detachment and reattachment. This attachment and detachment phenomenon is often called stick-slip. During the array sliding failure, the individual fibers of the array are losing contact and reattaching. Since there are thousands of structures this result is averaged out. This is another advantage afforded to fibrillar adhesive structures because of their distributed, redundant contacts. However, pronounced stick-slip was not seen in all force traces. When we use a more flexible cantilever (629a03), we see pronounced stick-slip events more often. Though not ideal from a measurement standpoint, the more flexible cantilever provides a more realistic testing of the adhesive pillar. This is because the pillar performs best when suspended on a compliant structure to allow for conformation to the surface irregularities. This adhesive has been integrated with a compliant backing and showed improvement in its performance [39].

The stick slip events with the more flexible cantilever can be seen in Figure 5.9. Notice that at the same time that the shear adhesion is lost due to the slip detachment event, there is also a loss in normal adhesion. When we use a stiffer cantilever (529b02) however, the amount of adhesion lost is less as we see in Figure 5.7. This could be a reflection of the larger amount of deflection in the more compliant cantilever. When the interface fails, the more compliant cantilever moves a larger distance and makes it more difficult to quickly reattach. The cantilever surfaces have not been well characterized to determine if this is only due to the stiffness difference or is related to some irregularity on the surface of the cantilever.
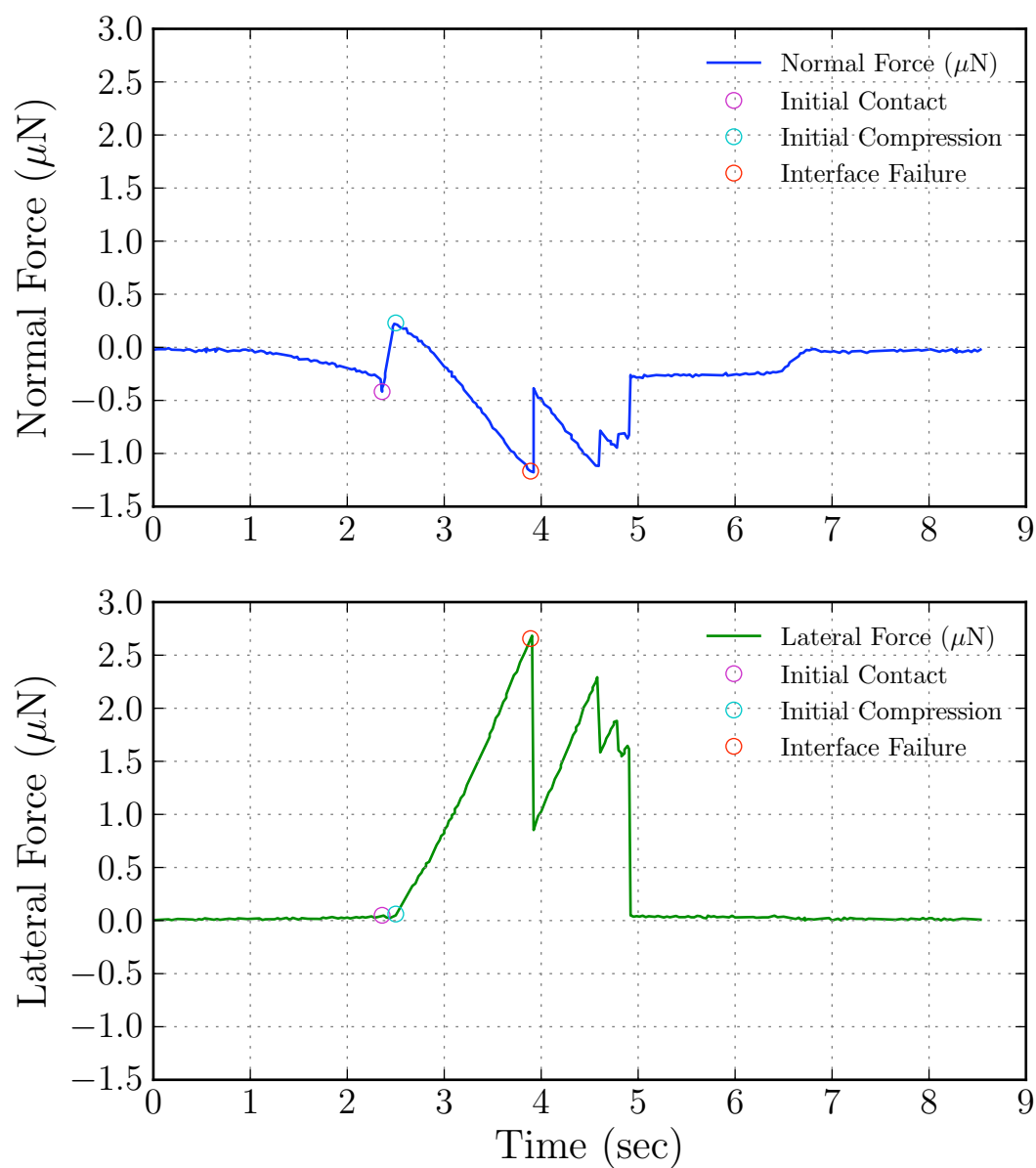
Figure 5.9: This force trace was performed using a more compliant cantilever than in Figure 5.7. Note that after the initial failure that there is a larger loss of force before the reattachment event.

	Shear Stress (kPa)	Normal Stress (kPa)
Predicted	2.7	11
Measured	4.5	13

Table 5.2: Comparison of extrapolated failure stress and observed failure stress for adhesive arrays. The single pillar measurement underestimates the force observed in the array measurements.

5.3.2   Single Wedge Limit Curve

A single wedge limit curve is shown in Figure 5.10. This limit curve shows an interesting behavior not seen in the array limit curves. For small shear loads, there is a reduction in the amount of normal force capacity, consistent with pressure-sensitive adhesive behavior. Once a threshold of approximately 2 μN of shear force is applied, the behavior changes to the frictional adhesion behavior. This low shear adhesive behavior, in the context of an adhesive optimized for climbing, can be thought of as a parasitic adhesion. To overcome this parasitic force to detach would compromise the efficiency and stability of an animal or robot using such an adhesive [9]. We do not observe this parasitic adhesion in the arrays. Unless the adhesive pillars fail simultaneously, we are unlikely to see this parasitic effect.

The wedge limit surface shows that for near vertical pulloff directions, there is relatively little change in the normal adhesive failure force observed. For near parallel pulloff directions, however, there is a clear dependence on preload, with larger preload forces leading to improvement in both shear and normal forces at failure. This behavior is also observed in the adhesive setae of the tokay gecko [36].

If we assume simultaneous attachment of all fibers with equal force, we can find the predicted array adhesions by

$$F_s \rho_s \tag{5.1}$$

were F_s is the force per stalk predicted by the single pillar measurements and ρ_s is the density of stalks. For the corresponding arrays for this single structure the stalk density is 625 per mm^2. Comparing the points on the limit curve with the highest tensile stress, and using 4.3 μN and 17 μN we generate the Table 5.2.
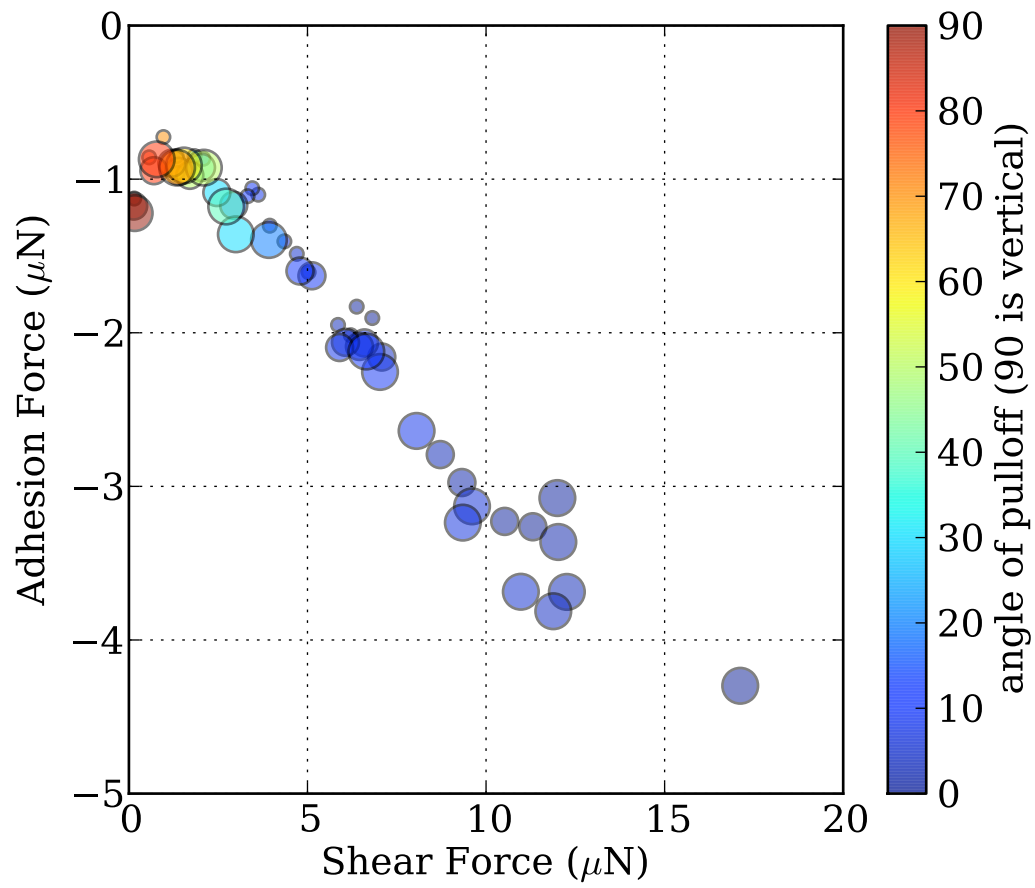
Figure 5.10: Limit curve for single wedge element. Color denotes the angle of pulloff. The size of the plot elements represents the force at the maximum compressive load.

In Table 5.2 we see that the measured normal force is greater than that predicted by the single pillar measurements. We believe that this discrepancy comes from the different relative stiffnesses in the single pillar and array measurements. The array measurement uses a force plate that is much stiffer than the array and can deform the pillars more than is possible in the single pillar tests with the more compliant dual-axis cantilever.

5.3.3   Non-Tapered Wedge Limit Curve

It is challenging to manufacture the tapered shape found in our adhesive pillars. To determine the effect of the tapered shape, isolated single adhesive pillars of uniform cross-section were fabricated and tested in the same way as the tapered to determine the limit curve.

The dimensions of the non-tapered pillar were chosen to match the height (60μm) and width (20μm) of the tapered pillar but with a range of thicknesses in the direction of bending. The thickness of the pillar tested (12μm) provides more lateral compliance (0.03 N/m) than the tapered pillar (0.15 N/m). This adjustment was to create a pillar sufficiently compliant to create side contact between the pillar and the force cantilever. A scanning electron microscope image of the nontapered and tapered pillars is shown in Figure 5.11

The nontapered pillar limit curve is shown in Figure 5.12. The curve shows a reduction of normal adhesive capacity with increasing shear force.

In Figure 5.13, we see the limit curve of a tapered pillar and a non-tapered pillar shown on the same plot. These limit curves show that the tapered pillar exhibits a gecko-like frictional adhesion behavior while the non-tapered pillar exhibits pressure-sensitive adhesive behavior[9].

5.4   Slanted Beam Limit Curves

Natural fibrillar adhesive structures are usually at angle to the substrate less than 90 degrees. We were curious about the performance of tapered structures that were
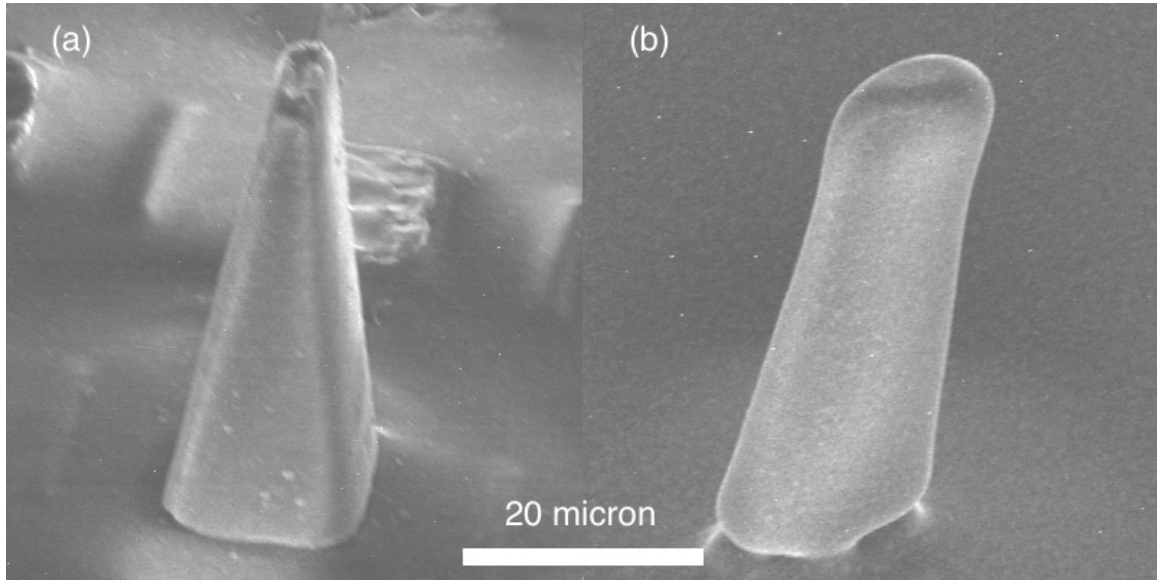
Figure 5.11: SEM Images of pillar types. Both pillars share a base width of ∼20 μm and a height of ∼60 μm. The pillar in (a) is ∼20 μm thick at the base and tapers to a tip. The pillar in (b) is ∼12 μm thick at the base and has uniform thickness along the length of the beam.

at an angle to the backing. However, fabrication issues of alignment between layers prevented us from creating tapered angled pillars. Using the degrees of freedom available in the test apparatus, we were able to vary the angle of the pillar with respect to the force cantilever substrate. This variation of angle is depicted in Figure 5.14. We conducted tests that varied the angle of the pillar in the plane defined by the cantilever normal and the proximal-distal axis of the pillar.

The data in Figure 5.15 show that as the angle between the substrate and the pillar is moved into the preferred direction (positive θ), the normal force capacity for a given amount of shear force increases. This corresponds to an increased stability for an adhesive with a fixed shear load. The variation in normal force to break the interface at zero shear load is much less than the variation at shear loads greater than 2 μN. In this region, it seems likely that the adhesion is dictated by the shape of the tip rather than the compliance of the beam. The effect of the beam compliance on adhesion will be discussed in Chapter 6.
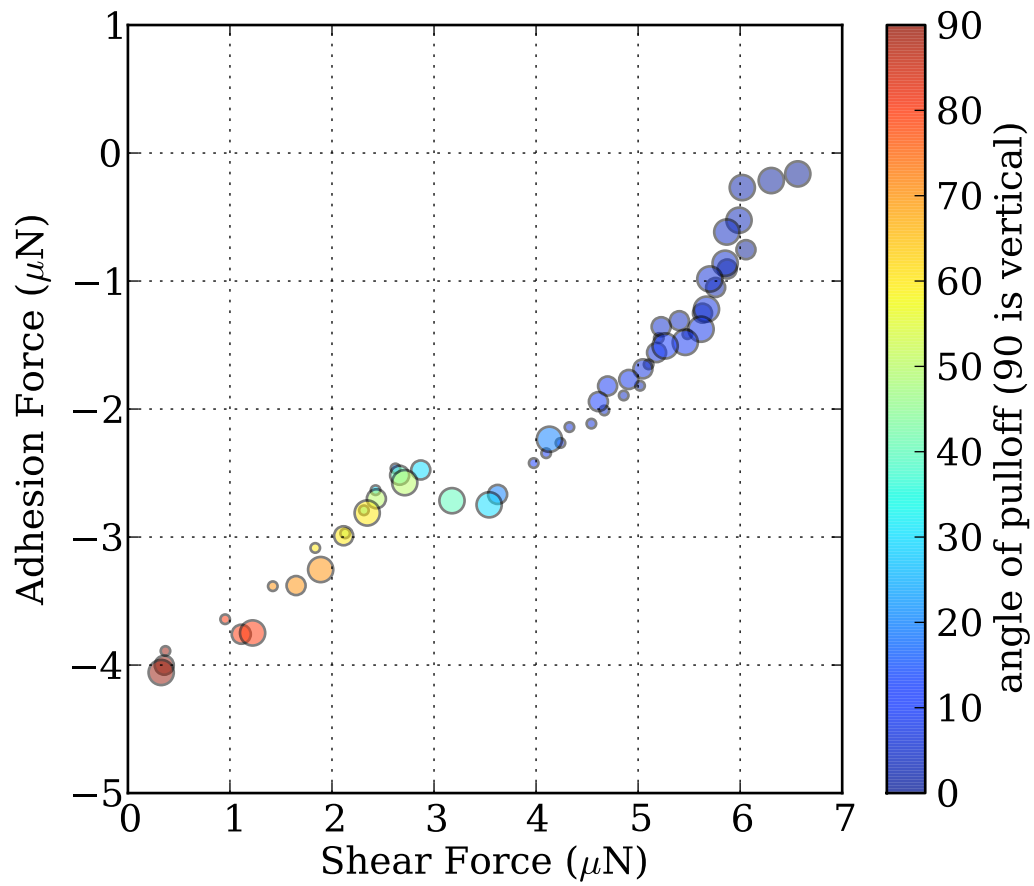
Figure 5.12: Limit curve for single nontapered pillar element. Each plot point represents an adhesive failure. Notice the decline in normal force capacity with increasing shear force. The color depicts the angle of withdrawal of the cantilever. The size of the circle indicates the amount of compression applied before the tensile phase.
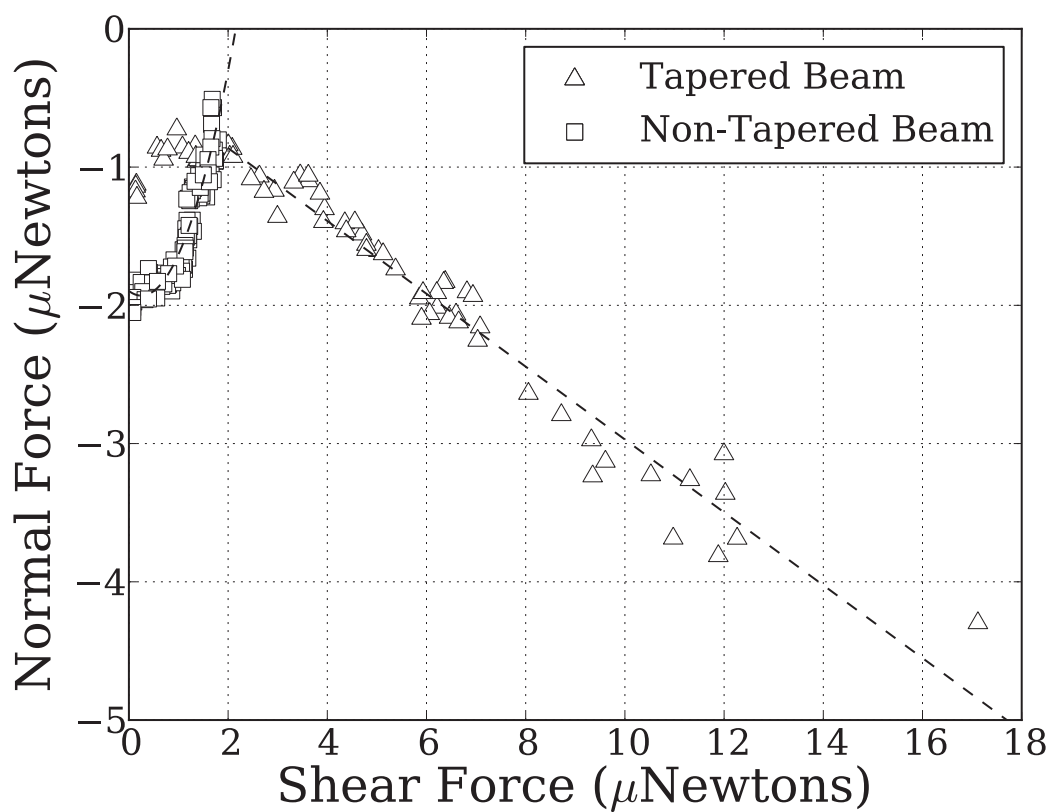
Figure 5.13: Limit surfaces for tapered and non-tapered single pillars. Each data point reports the forces preceding a single failure event. Trials are run at 19 pull angles ranging between 0 degrees (vertical) and 90 degrees (shear). Each of these angles is tested at two different levels of peak compressive load.
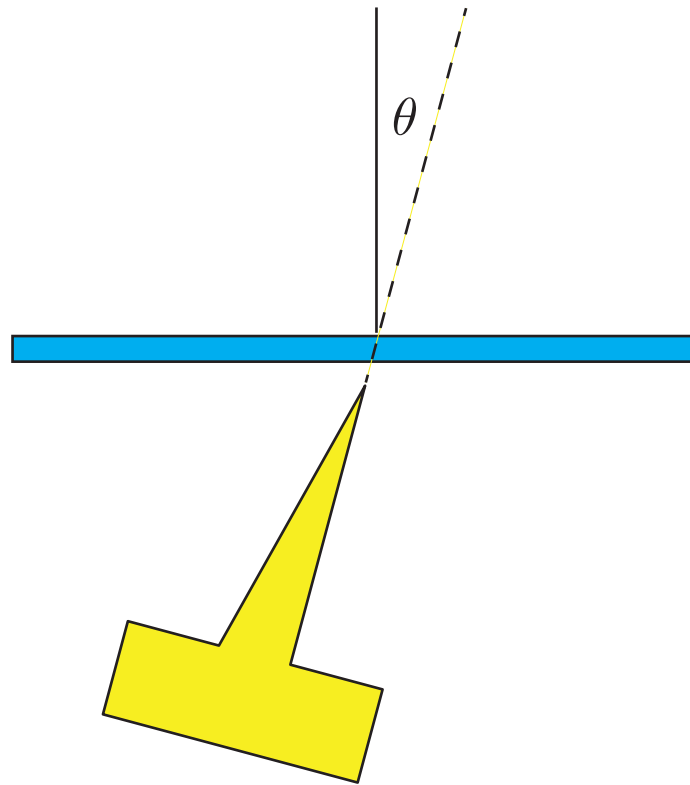
Figure 5.14: Drawing of slant angle definition used in testing. Angle is between the back vertical face of the wedge structure and the normal to the cantilever surface. Positive angle is considered to be the preferred slant direction for the structure.
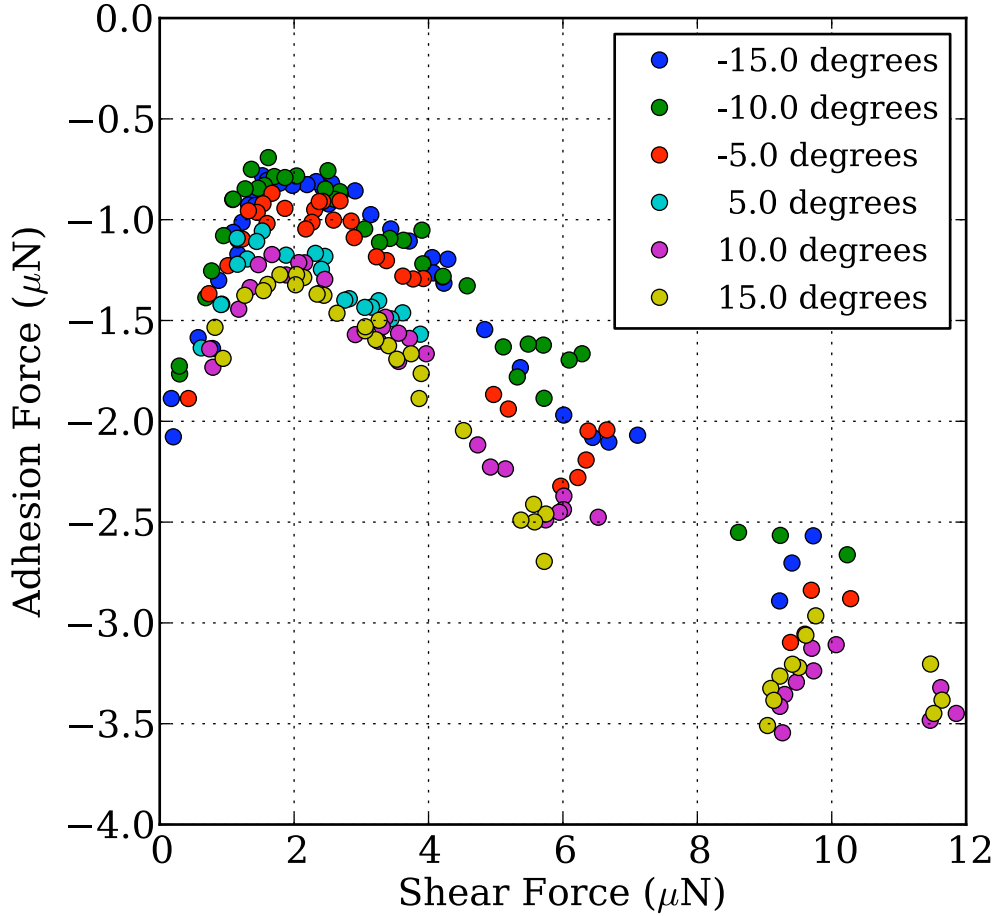
Figure 5.15: Limit curves of single pillar at varying angles with respect to the force cantilever surface. Each plot point represents an adhesive failure. The amount of normal adhesion force necessary for failure increases with the application of shear force to the interface as the angle is moved from the anti-preferred to the preferred angle.

Adhesive pillars that are inclined with respect to the substrate have a lower effective stiffness. As the beam angle moves away from perpendicular, the load moves from axial to shear and the deflection is greater. This lower effective stiffness could be observed as a function of the slant angle of the beam. Figure 5.16 shows the measured relation of the normal component of compliance with slant angle. This lower effective
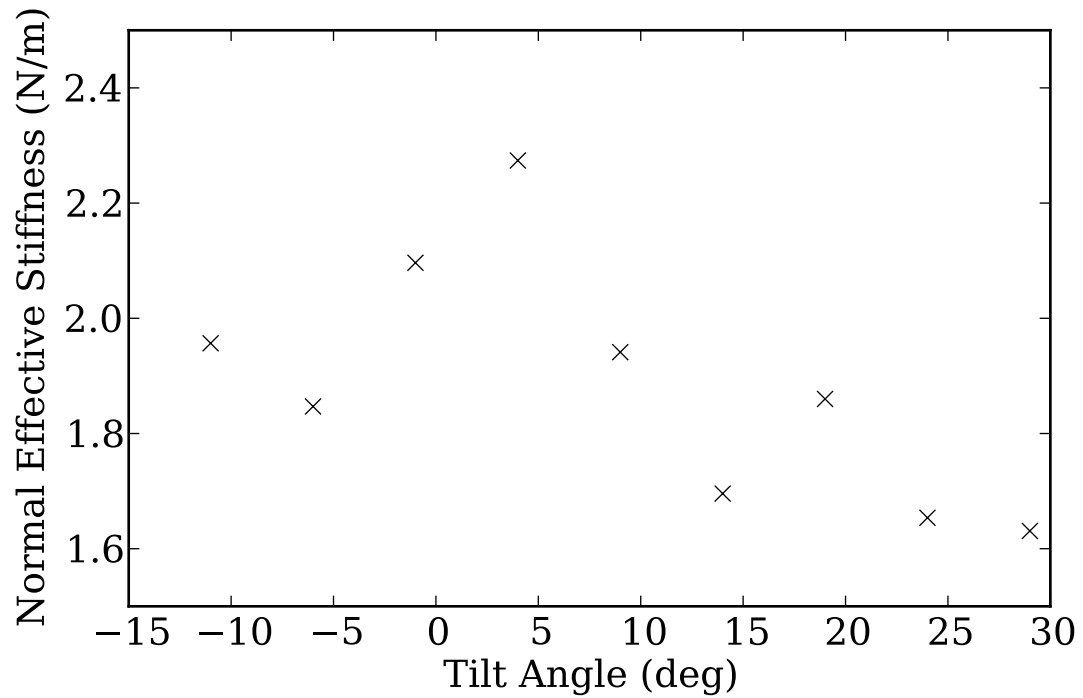
Figure 5.16: Plot of measured stiffness in the normal axis vs. the angle of the pillar. Highest stiffness is measured near zero degrees.

modulus could improve the ability of the adhesive to engage with lower initial compression forces. This would be advantageous for efficient and stable climbing since the initial compression forces must be balanced by the adhesion of the other contacts of a climbing animal or robot.

These results point toward the importance of the leaning angle of the fibril in the performance of the adhesive.

Chapter 6

Modeling

In Chapter 5, different limit surfaces were observed depending on the shape of the beam. The aim of this chapter will be to present models that can provide insight into this behavior. We would like to develop a model that predicts these observed changes in the limit surface as a function of the beam shape. Such a model could allow for the design of beams with engineered limit surfaces to provide the type of adhesion desired for a specific application.

Fibrillar adhesives are often modeled using contact models developed for hemi-spherical contacts [31]. These models are applicable for low aspect ratio fibrils. For high-aspect ratio fibrillar adhesives, models of adhesion incorporate the bending of the fibrils [40]. These bending models use elastica beam theory [41] to predict the shape of the beam. To account for the highly anisotropic behavior of gecko adhesive, a model known as the 'peel-zone' model was proposed [42]. This work attempts to use the 'peel-zone' model along the elastica beam model to predict the change in the limit surface observed.

6.1 Peel Zone Model

We begin these modeling efforts with a description of the peel-zone model of fibrillar adhesion which attempts to capture gecko-like adhesive behavior. In the peel zone model, the central idea is that the area of the surface in contact gives rise to the

friction forces observed and the area in close proximity where the pillar is peeling away from the substrate is responsible for the adhesion. The model assumes that the shear stress is uniform over the area in contact and that the resulting friction force is directly proportional to the amount of area in intimate contact. The adhesion force is calculated by integrating the attractive force in the area in close proximity. The model finds that the adhesion force is an increasing function of the radius of curvature of the beam in this area of close proximity or 'peel zone'. An illustration of these regions can be seen in Figure 6.1. The peel zone geometry applies to our situation in that when the pillar is sufficiently sheared by the cantilever, the tip of the pillar is bent so that a length of the flat section of the pillar is in side contact (see Figure 6.12. The task is then to model the shape of the beam under the adhesion conditions of our test, determine the size of the region in contact and the region in close proximity and then predict the forces the interface is capable of withstanding. This approach will build on the peel-zone model, which lacks a consideration of the beam mechanics of the fibril.

6.2   Elastica Model

To find the profile of the beam for use in the peel-zone predictions of adhesive force, we use the elastica beam model. The elastica beam model [41] allows the calculation of a beam profile for large angle deflection of an elastic beam. The elastica model of beam deflection has been used by researchers in the calculation of the deflection of microfabricated polymer structures [40, 43]. The elastica model is used because the more familiar model, the Euler beam model, is not valid for large angle deflections. Unlike the Euler beam model, the elastica model does not rely on an approximation of the curvature. This model of beam deformation will allow us to simulate the beam profile under loading. To solve for the beam profile given a load and shape, we solve the equation

$$M = \kappa EI \tag{6.1}$$
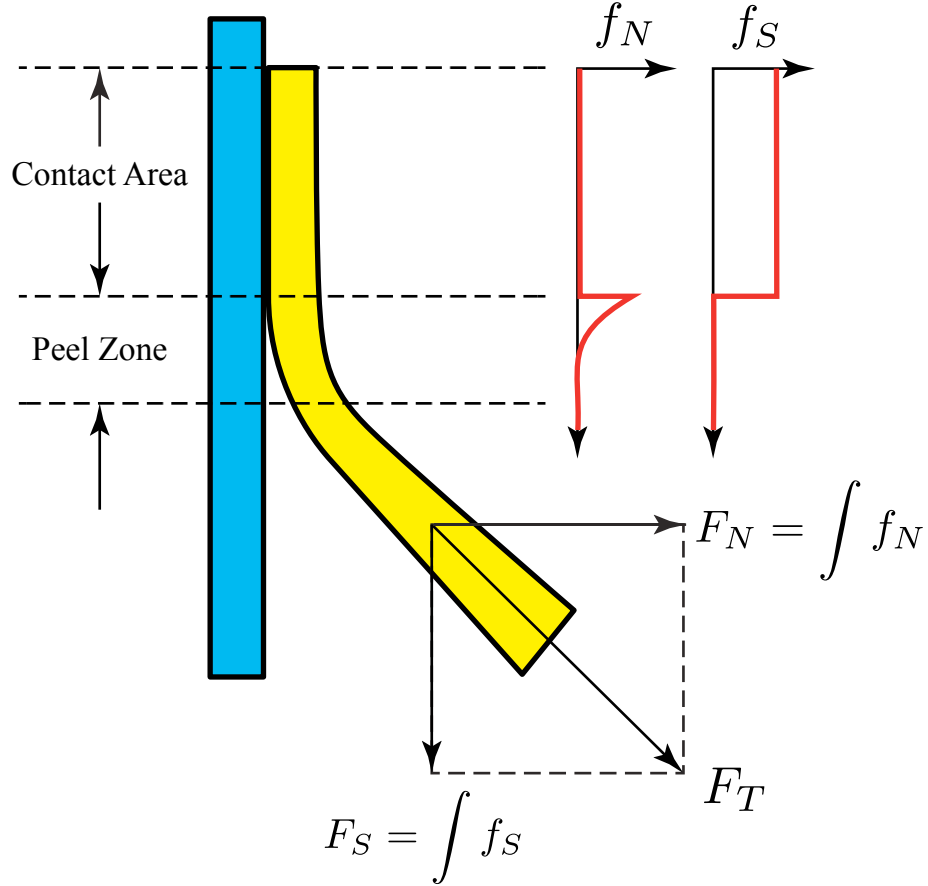
Figure 6.1: Pillar peel diagram. The peel zone model assumes uniform shear stress distributed over the contact area. The peel zone is defined as the region with contact close enough for significant van der Waals force. The total force transmitted along the beam is the vector sum of the shear force in the contract area and normal force in the peel zone area.

where M is the bending moment on the beam, E is the elastic modulus of the material, I is the moment of area of the beam, and κ is the curvature of the beam.

In cartesian coordinates, the curvature κ is expressed exactly as

$$\kappa = \frac{y''}{(1 + y'^2)^{3/2}}. \tag{6.2}$$

Euler beam theory assumes that the slope (y') is negligible compared to unity and that the curvature (κ) can be approximated by the second derivative (y''). Instead of cartesian coordinates, the beam is expressed with parameterized coordinates of arc length (s) and tangent angle along the beam ($\psi(s)$), reminiscent of the Frenet-Serret formulas. These coordinates allow the curvature to be expressed exactly as

$$\kappa = \frac{d\psi}{ds}. \tag{6.3}$$

This elastica formulation allows us to sidestep the small angle deflection restrictions of Euler beam theory. The other benefit of expressing the beam slope as a position of arc length is that the beam shapes observed in experiments that would be multivalued functions in cartesian coordinates, are expressed easily. The model as presented here does not take into account shear strain in the beam, which can affect the results.

Using this alternate set of coordinates, the beam equation (Eq. (6.1)) becomes

$$M = \kappa EI = \frac{d\psi}{ds}EI, \tag{6.4}$$

In general, M and I are functions of the arc length, s, and we have the first-order differential equation

$$\frac{d\psi}{ds} = \frac{M(s)}{EI(s)}. \tag{6.5}$$

This function can be solved either analytically or numerically depending on the form of the resulting functions for the load and shape of the beam. We now turn to a discussion of the loads and beam shapes in our adhesive wedge structures. We approximate the loading with a combination of point loads and moments to reflect the shape observed during testing.
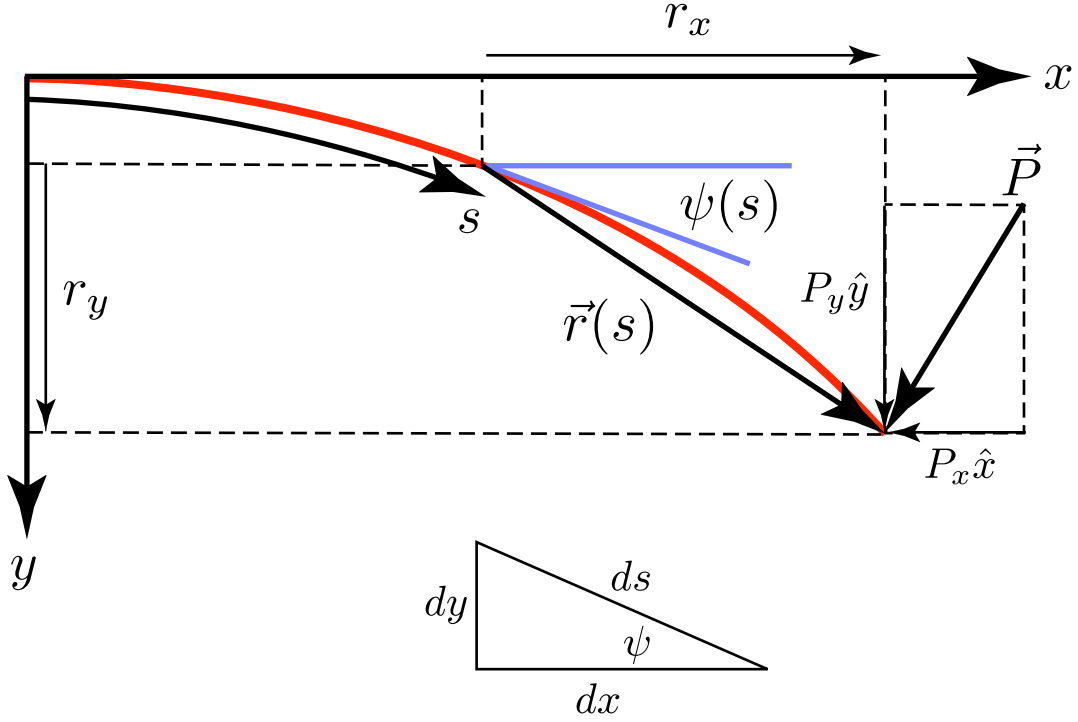
Figure 6.2: Elastica coordinates for point load. x and y denote the cartesian system used to describe beam displacement. s is the displacement along the beam, and ψ is the angle of the beam with respect to the x-axis at the point s. $\boldsymbol{P}$ is the load, $\boldsymbol{r}$ is the lever arm for the moment at point s along the beam. The small triangle shows the decomposition of ds along the x and y axes.

6.2.1 Cantilever with Point Load at End

Consider the case of a point load applied at the end of a cantilevered beam. Following the treatment in [41] we apply this point load to an elastica beam representing the adhesive pillar. In Figure 6.2 we have the geometry of our horizontal cantilever with this point load. To solve the bending equation

$$\frac{d\psi}{ds} = \frac{M(s)}{EI(s)}. \tag{6.6}$$

we must find the bending moment (M) and the moment of the beam (I) in terms of the variables s and ψ.

To find the bending moment along the beam, we look at the vector product between the displacement vector and the applied load. The magnitude of the moment is equal to the magnitude of the cross product between the vector from the point on the beam to the load ($r(s)$) and the load (P).

$$M = r(s) \times P \tag{6.7}$$

If we decompose the load, P, into shear and axial components and project the displacement vector $r(s)$ onto the x and y axes, (see Figure 6.2) we can express the magnitude of the moment as

$$M = P_y r_x - P_x r_y. \tag{6.8}$$

If we substitute this expression for the moment into equation (6.6) we obtain

$$\frac{d\psi}{ds} EI = P_y r_x - P_x r_y \tag{6.9}$$

By differentiating the equation with respect to s, the components of the displacement vector $\vec{r}$ become trigonometric functions of ψ, which allows us to express the equation purely in terms of ψ. Note that

$$r_x(s) = \int_s^L \cos\psi \ ds = -\int_L^s \cos\psi \ ds \tag{6.10}$$

Differentiating this expression by the arc length, we find

$$\frac{dr_x(s)}{s} = -\frac{d}{ds} \int_s^L \cos\psi \ ds = -\cos\psi. \tag{6.11}$$

Similarly, we find that

$$\frac{dr_y(s)}{s} = \sin\psi. \tag{6.12}$$

By substituting Eqs.(6.11) and (6.12) into Eq. (6.9), we obtain

$$\frac{d^2\psi}{ds^2} EI = -P_y \cos\psi + P_x \sin\psi. \tag{6.13}$$

This equation is solved numerically to determine the beam shape for a given point load. This second-order equation is reduced to two coupled first-order equations for the numerical calculation.

Equation (6.13) holds for a beam of uniform cross-section. The beams under consideration have a wedge shape. These beams are modeled as a truncated prism as shown in Figure 6.3. To express the taper, there are two length scales for the pillar. The first is the actual length, the second is the distance from the base where the planes defined by the sides of the pillar would intersect. The thickness of the beam is then a linear function of the arc length variable s.

$$b(s) = b_0 \left(1 - \frac{1}{L_T} \right) s \tag{6.14}$$

The moment of area of the beam includes this term for the thickness

$$I(s) = \frac{1}{12} \frac{wb(s)^3}{L^3} \tag{6.15}$$

In the case of a non-uniform cross-section of the beam, the derivatives of the moment of inertia of the beam with respect to the arc length are non-zero. In this case, the equation is

$$\frac{dI}{ds}\frac{d\psi}{ds} + I(s)\frac{d^2\psi}{ds^2} = (P_x \sin \psi - P_y \cos \psi)\frac{1}{E}\frac{dx}{ds} \tag{6.16}$$

$$\frac{d^2\psi}{ds^2} = \left[(P_x \sin \psi - P_y \cos \psi)\frac{1}{E} - \frac{dI}{ds}\frac{d\psi}{ds} \right] \frac{1}{I(s)} \tag{6.17}$$

Once the slope has been determined as a function of the arc length, the cartesian coordinates of the beam position can be determined by integrating the slope function.

For the point load, the boundary conditions are the undeflected slope at the base of the beam

$$\psi|_{s=0} = 0 \tag{6.18}$$
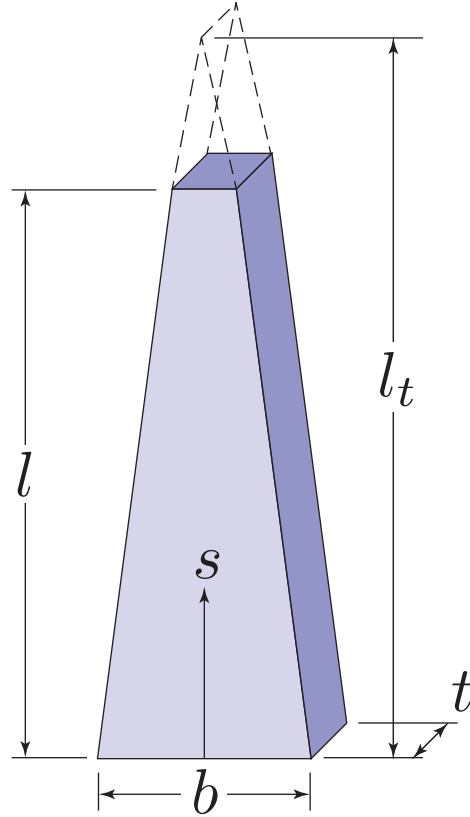
Figure 6.3: Dimensions used in the simulation of the tapered beam. The length l is the physical extent of the beam while the taper length l_t is the point at which the beam thickness would vanish. Due to imperfections in the fabrication process, these lengths are not the same. s is the arc length along the beam and b and t are the dimensions at the base of the structure. The tapered structures tested in this work have dimensions approximately $l = 50$ μm, $b,t = 20$ μm, and l_t=80 μm.

and the zero curvature at the end of the beam

$$\psi'|_{s=L} = 0. \tag{6.19}$$

6.2.2 Fixed Slope at End of Beam

The actual loading condition of the beam during testing applies a shear load but generally provides an additional constraint that the end of the beam is parallel to the substrate ($\psi = \pi/2$).

In this case, the boundary conditions are the slopes at both ends of the beam

$$\psi|_{s=0} = 0 \tag{6.20}$$

$$\psi|_{s=L} = \frac{\pi}{2} \tag{6.21}$$

In this case, the curvature at the end of the beam is a free parameter. This is in contrast with the point load case where the curvature is zero at the end. A shooting method solution is used since neither of these cases provides an initial condition that can be used to uniquely solve the beam. The initial curvature ($\psi|_{s=0}$) is guessed and the solution is performed until the condition at the end of the beam matches the boundary condition.

6.3 Numerical Results

6.3.1 Validation

We solve the differential equation governing the beam shape (Equation (6.17)) numerically. Before using the model to simulate beam deformations, we pause to perform some simple verifications. We verify the model for small point loads by comparing it to the Euler model of beam bending for a point load. Figure 6.5 shows a plot of the tip displacement as a function of the load. The models are in good agreement for

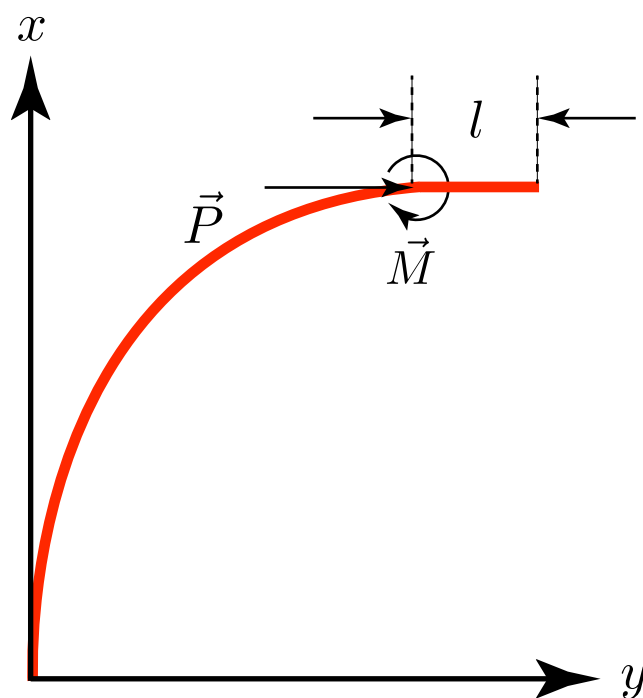Figure 6.4: Depiction of parameters used in side contact elastica model. The load $\boldsymbol{P}$ is proportional to l, the length in contact. The point moment $\boldsymbol{M}$ is applied at the point where the pillar begins to peel out of contact.
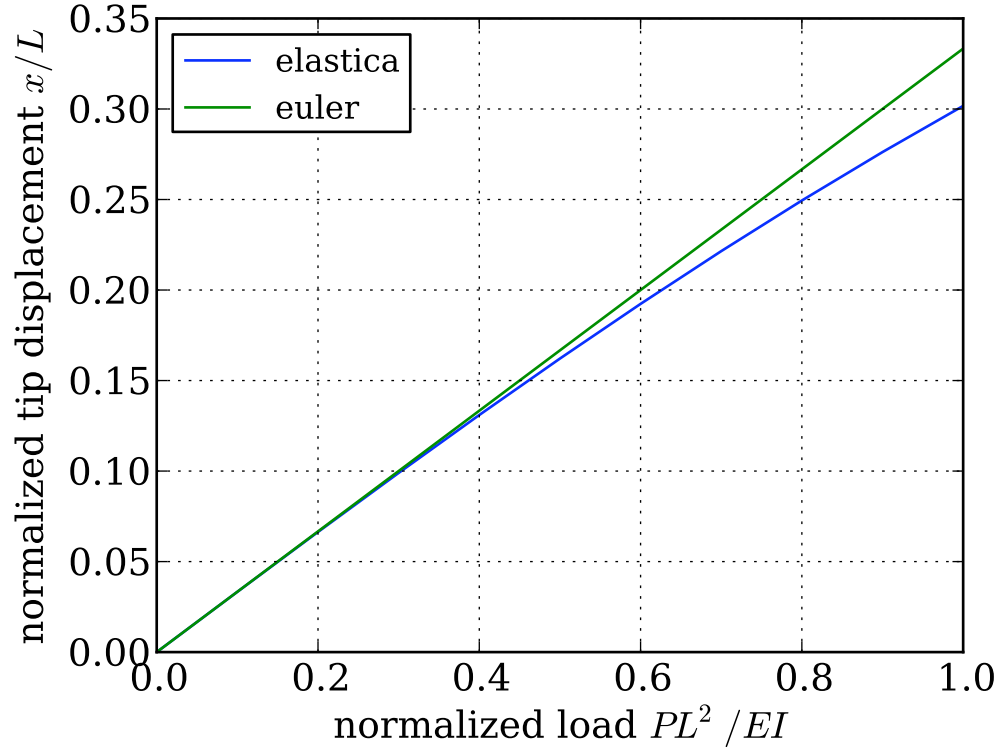
Figure 6.5: Normalized tip deflection as a function of load for both the Euler beam model and the elastica numerical model. The models have good agreement for smaller loads and diverge with the application of larger loads. This plot is for the typical pillar dimensions and the normalized loads correspond to approximately 0-4μN.

small loads. We expect the models to diverge for larger loads where the beam slope is no longer negligible.

The next demonstration of the model is the beam profile under various loading conditions. The first of these loading conditions is that of a point shear load. Figure 6.6 shows a simulated pillar under increasing shear load. The beam shows increased deflection with increased shear load. The profile however, does not match the profile observed in the testing. A point load does not result in the end of the beam bending over to be perpendicular to the base of the beam. To get profiles that match the testing of the adhesive pillars, we add a point moment condition.

Figure 6.6: Profile predicted by elastica model of various beam loadings. Note that the beam does not become vertical in these cases. Under experimental conditions the beam is 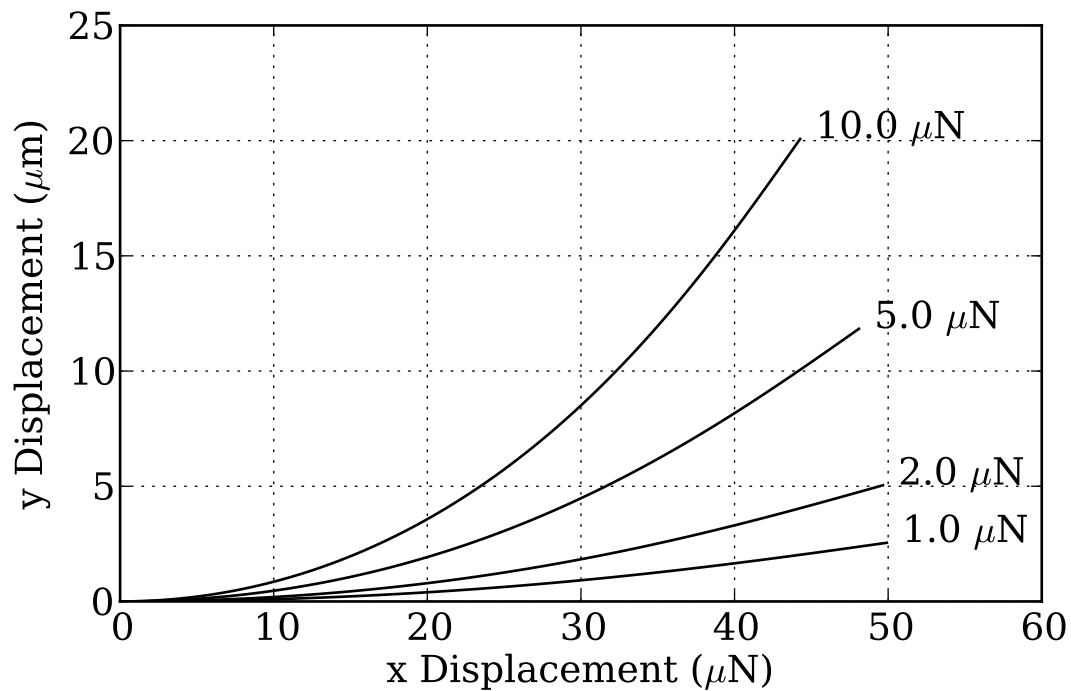bent over at the same shear force load. For this reason, we impose the extra point moment condition to get a more realistic profile in the model.
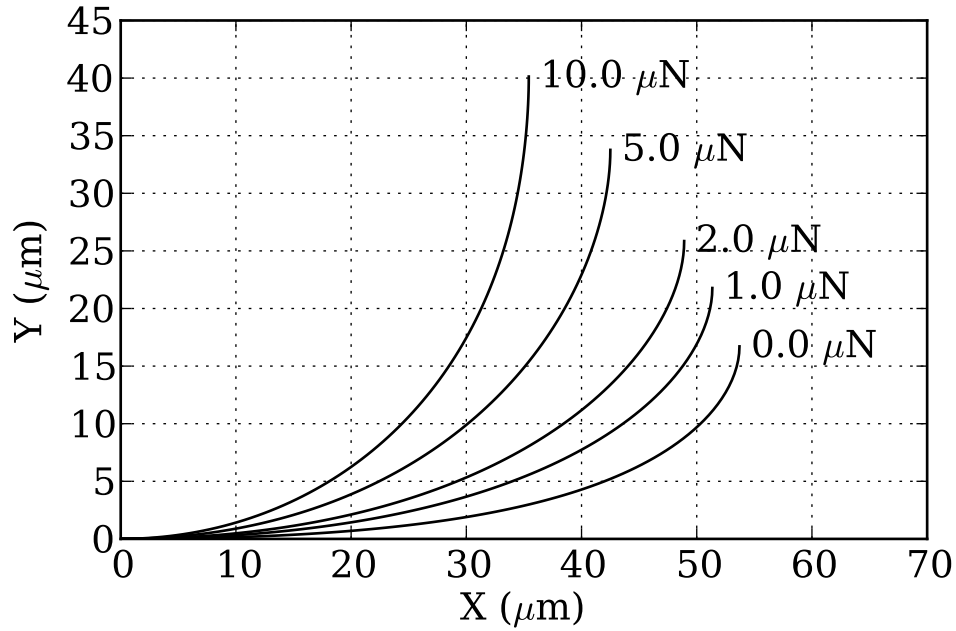
Figure 6.7: Constrained end angle with varying point shear load. Model simulates a tapered beam of nominal dimensions and constrains the end angle to be 90°. The magnitude of the shear load is varied and the beam profile is plotted.

Figure 6.7 is a plot of a simulation of an adhesive pillar constrained so that the end angle is 90 degrees from the base of the pillar. The pillar also has increasing amounts of normal shear load applied. If we compare this profile to the images observed experimentally (Figure 6.12), the simulation seems more plausible than those given for only a point moment.

It is difficult to accurately compare the profiles for a given shear force applied. The image quality of the microscope system made accurate measurement of the profile and length of side contact difficult. Another compounding factor is that the piezoresistive force sensors are light-sensitive. This invalidates the calibration curves, which are obtained under dark conditions.

6.3.2   Limit Surface Simulation

With the model giving plausible results, we start to simulate the behavior of uniform and tapered beams looking for differences in the behavior that may explain the limit curve differences we observe. We start by looking at the profiles of the beams under the experimental loading conditions. We then simulate the loading of the beam in the experiment and observe the beam geometry. By extracting the beam geometry in the regions of interest in the peel-zone model, we hope to gain insight into the limit curve.

When we plot the profiles of these two pillars for the condition of having the end angle of the beam at 90 degrees we see a clear qualitative difference in their profiles. Figure 6.8 shows two beams of dimension 60μm long with 20μm by 20μm bases. The difference is that the tapered beam would converge to a point at 80μm, giving a 5μm thick tip, which is reasonable in our fabricated structures. The plot shows that for the uniform thickness pillar that the radius of curvature is constant over the length of the beam. In the absence of a point load, the beam is indeed a circular arc. The tapered beam however, shows that the curvature is concentrated at the end of the beam. In the absence of a point load, the bending moment is uniform over the beam but the non-uniform moment of inertia leads to a non-uniform curvature.

In the previous chapter we showed the difference in the observed limit curve depending on the shape of the pillar. For frictional adhesion to occur, the peel-zone suggests that as the area in contact increases, the radius of the beam in the peel zone increases. As the radius of curvature increases, the normal force capacity of the fibril increases, giving a frictional adhesion limit curve. In contrast, the limit curve observed in pressure-sensitive adhesives would be observed if the radius of curvature in the peel-zone decreased as the length in contact increased.

Glassmaker and Hui [44] show that for a beam in a similar geometry that the radius of curvature in this peel zone is an increasing function of the moment of inertia of the beam. Due to the taper, the thickness and moment of inertia of the pillar at the peel-zone increases and the radius of curvature at the point of peeling increases. As this radius increases, the length of the zone close enough for attractive force increases, allowing for more normal adhesion and the adhesive demonstrates frictional adhesion.
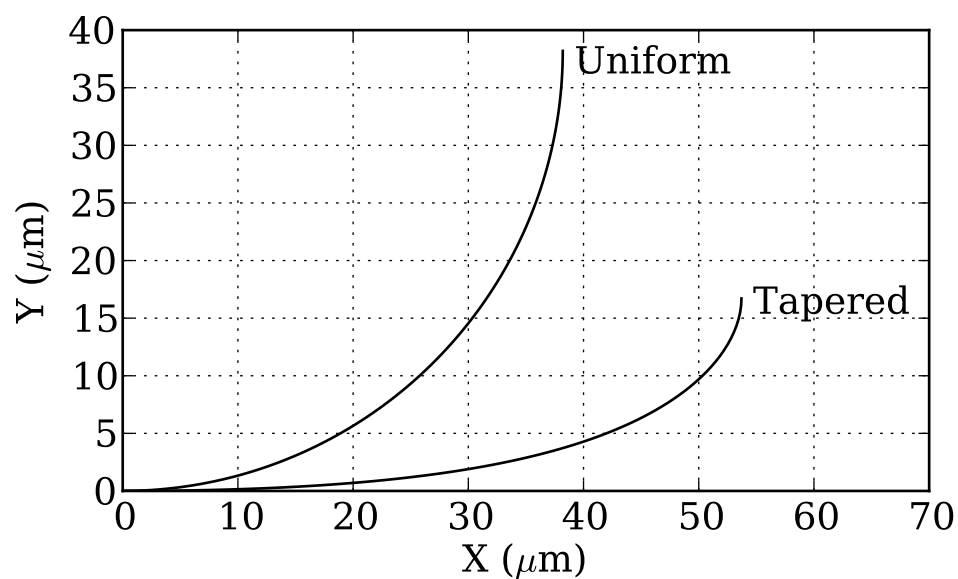
Figure 6.8: Comparison between beam profile for a uniform beam and a tapered beam with the end at 90 degrees. Beam profile is simulated using the elastica model. The curvature for the uniform beam is constant throughout the beam while for the non-uniform beam it is concentrated at the end of the beam.

Figure 6.9: Radius of curvature at peel-zone as a function of the length of fibril in contact for a tapered beam. The radius of curvature adjacent to the length of the beam in contact is calculated at varying lengths of beam in side contact at 90°. No shear for was applied in this simulation.

In contrast, the non-tapered beam has a uniform moment of inertia and does not show the increase in normal force with increasing shear force.

This section will show simulations that suggest that for a tapered and non-tapered beam this is the predicted behavior. Our strategy is then to observe the changes in this radius of curvature as we hold an increasing fraction of the beam in contact, as would be necessary to sustain increasing shear or friction force.

Using the dimensions appropriate for the structures under test we simulate the beam profile.

If we approximate the shear adhesion by the cylindrical JKR approximation [45] and ignore the tip radius and its effect on the adhesion at low shear values, we can
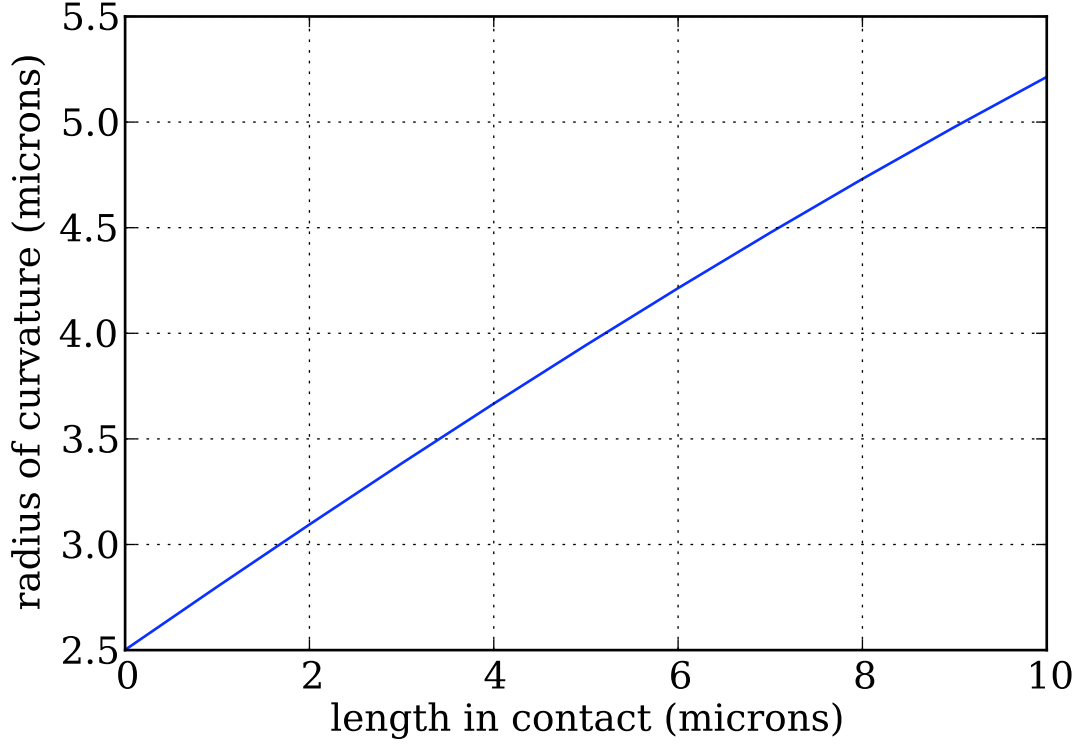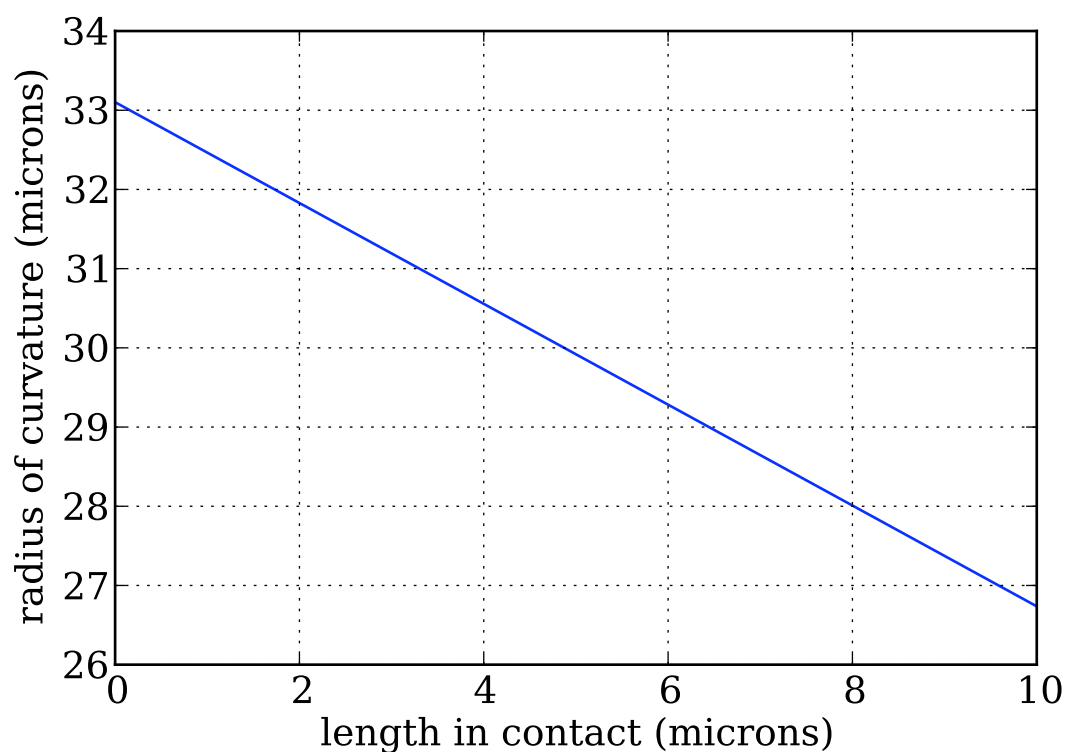
Figure 6.10: Radius of curvature at peel-zone as a function of the length of fibril in contact for a non-tapered beam. The radius of curvature adjacent to the length of the beam in contact is calculated at varying lengths of beam in side contact at 90°. No shear for was applied in this simulation.

simulate the limit curve. The simulation shown in Figure 6.11, that as the shear adhesion increases, for a 20μm tip (no taper), that there is an decrease in the normal adhesion capacity. For smaller tip thicknesses, this situation reverses, with the limit curve showing negative slope for 2 and 5 μm tips. It is interesting to note that for an intermediate tip thickness there is a curve with near-zero slope.

These results suggest that by tailoring the pillar shape such that the local radius of curvature at the point of contact is an increasing function of shear load, frictional adhesion can be achieved. While the geometries are very different, the tokay gecko adhesive behaves in a similar fashion. The initial contact of the gecko adhesive is with the flat edges of the spatulae. With shear loading, the spatulae are bent into flat contact resulting in a large increase in shear adhesion. We must be cautious in using this beam model to explain gecko adhesion but we do observe similarities in these very simple tapered structures.
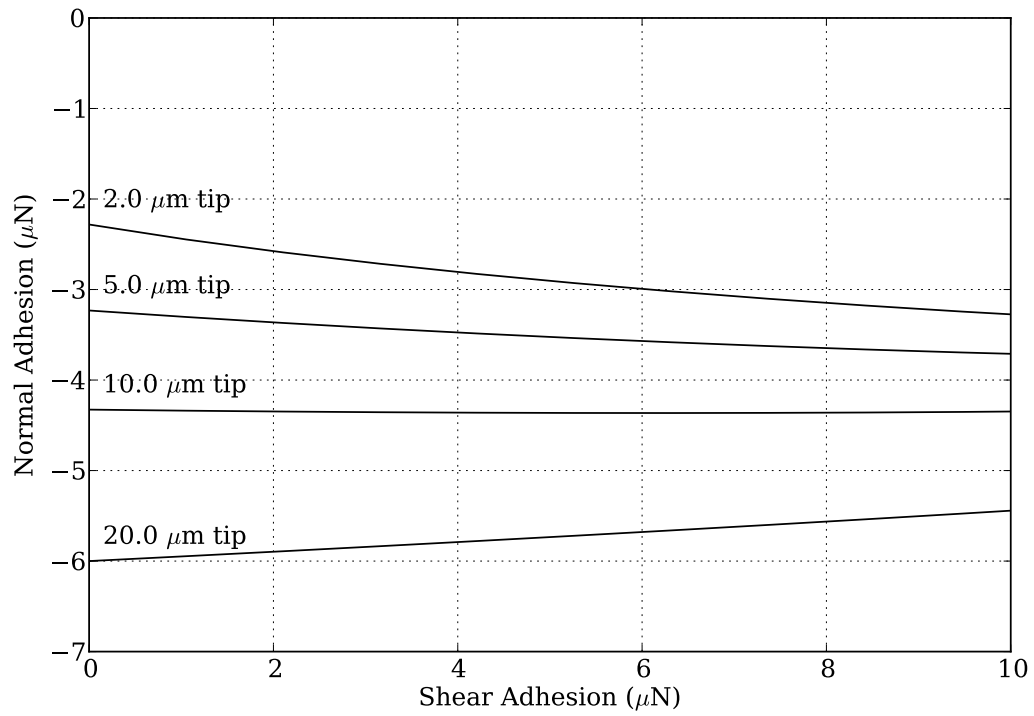
Figure 6.11: Limit curve simulation. Simulation computes the normal pull-off force using the cylindrical JKR formula for an elastica beam with a shear force and corresponding length in contact. The different curves depict a spectrum between tapered and uniform beams. The 20 μm tip is a uniform pillar and the 2 μm tip has the highest degree of taper.
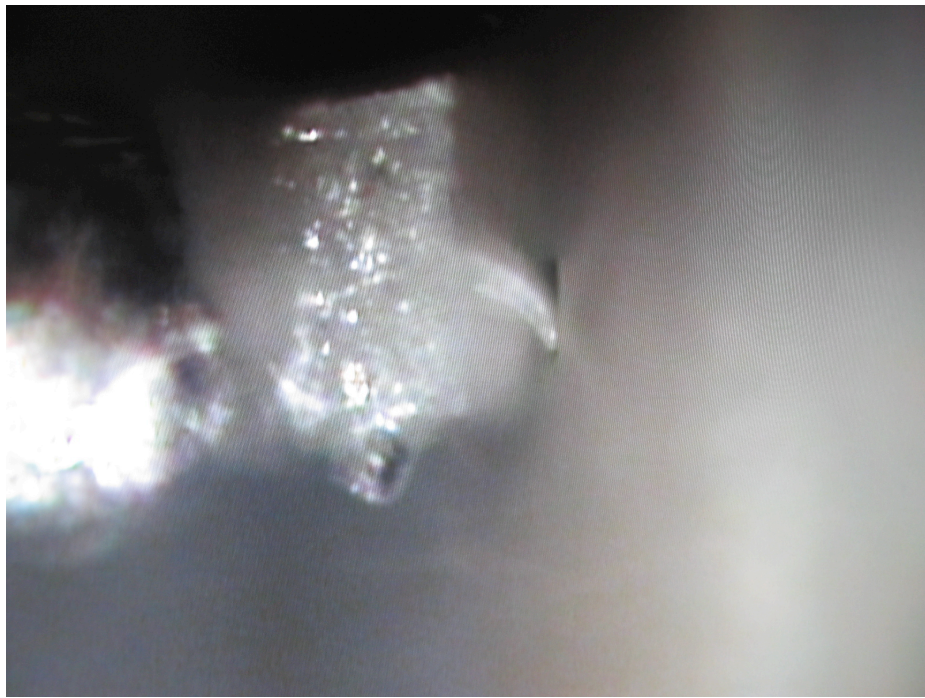
Figure 6.12: Photo of single wedge in cantilever test setup under deflection. The cantilever is the small vertical stripe in the center of the photo. The normal force axis is horizontal and the shear force axis is in the vertical direction.

Chapter 7

Conclusion

7.1 Summary

Inspired by the unique frictional adhesion property of the gecko's adhesive, we fabricated a microstructured adhesive with tapered pillars. Testing of arrays of these adhesive pillars revealed that the adhesive displayed the frictional adhesion property. This means that the adhesive becomes more tenacious in response to loading. Specifically, that the amount of holding capacity normal to the surface increases as the amount of shear stress at the interface is increased.

To determine if this frictional adhesion property is due to the fibril or due to the array, we tested a single adhesive fibril using a sensitive dual-axis micromachined cantilever. Using this cantilever we determined that the adhesive behavior of the single pillar differs from the array. First, the single pillar shows randomly occurring failures that are averaged out in the arrays. Second, the single pillar shows a limit curve whose behavior at low values of shear stress differs from the array's limit curve. The single pillar shows a normal force adhesion at low shear values that is not evident in the limit curve of the array.

We varied the pillar shape to determine if the tapered pillar shape contributes to the frictional adhesion behavior. To test, we fabricated adhesive pillars of uniform cross section that lacked the tapered shape. These structures did not exhibit frictional adhesion and instead displayed the type of adhesion found in pressure-sensitive

adhesives. We also varied the angle that the pillar made with the cantilever surface to investigate the effect of leaning angle. The limit curve showed an enhancement of the ratio of normal force to shear force with leaning angle.

Last, we presented modeling of these adhesive cantilevers predicting the differences in adhesion behavior of tapered and nontapered pillars. The modeling also predicted the enhancement of the adhesion as the leaning angle increased.

The results presented here will help inform the design of fibrillar elements that are customized for the application. Frictional adhesion, a property useful for climbing applications can be achieved using tapered, slanted beams. Nontapered beams, however, may be optimal for applications where frequent reattachment and easy detachment are not important.

7.2   Future Work

This thesis presents work important for synthetic fibrillar adhesives. The fabrication techniques in this work are difficult, labor intensive, and often low yield. The development of more robust and repeatable manufacturing methods make fabrication easier and aid in development of improved adhesives. If a more robust mold could be made, then large scale manufacturing of these fibrillar adhesives becomes possible.

Another opportunity for improvement is in the modeling of the behavior of these fibrillar elements. It would be very useful to validate the model using careful imaging of pillars under load. Finite Element Models using distributed rather than lumped forces would also increase confidence in the results presented here.

Improvements in these areas could enable adhesive technologies that in addition to the ability to adhere, have the ability to disengage quickly and cleanly. These adhesives can improve the capabilities of climbing robots or the throughput of flat panel manufacturing and could eventually find a place in consumer adhesives.

Appendix A

Beam Compliance Characterization

In addition to the limit curve testing of the cantilever, we have tested the compliance of the pillar. Testing of the compliance was used to help validate simulations of the beam profile in the previous chapter. This appendix describes the testing of the compliance of PDMS adhesive pillars in the normal and shear directions.

A.1 Compliance

A.1.1 Axial Compliance

Normal compliance was measured by bringing the flat end of the dual-axis cantilever into contact with the top of the microwedge tip. The cantilever was then moved along the axial dimension of the adhesive pillar to put the pillar into axial compression. The deflection of the pillar can be inferred as well as the force applied, yielding a spring constant for the adhesive pillar. The system is essentially two springs in parallel, one spring is the dual-axis cantilever spring in the normal direction, the other spring is the adhesive pillar. This effective spring constant is the force measured by the cantilever divided by the displacement of the stage. The slope of the curve in figure A.1 is this effective spring constant of the system. Defining k_E as the effective spring constant, k_P as the pillar spring constant and k_C as the cantilever spring constant, the relation
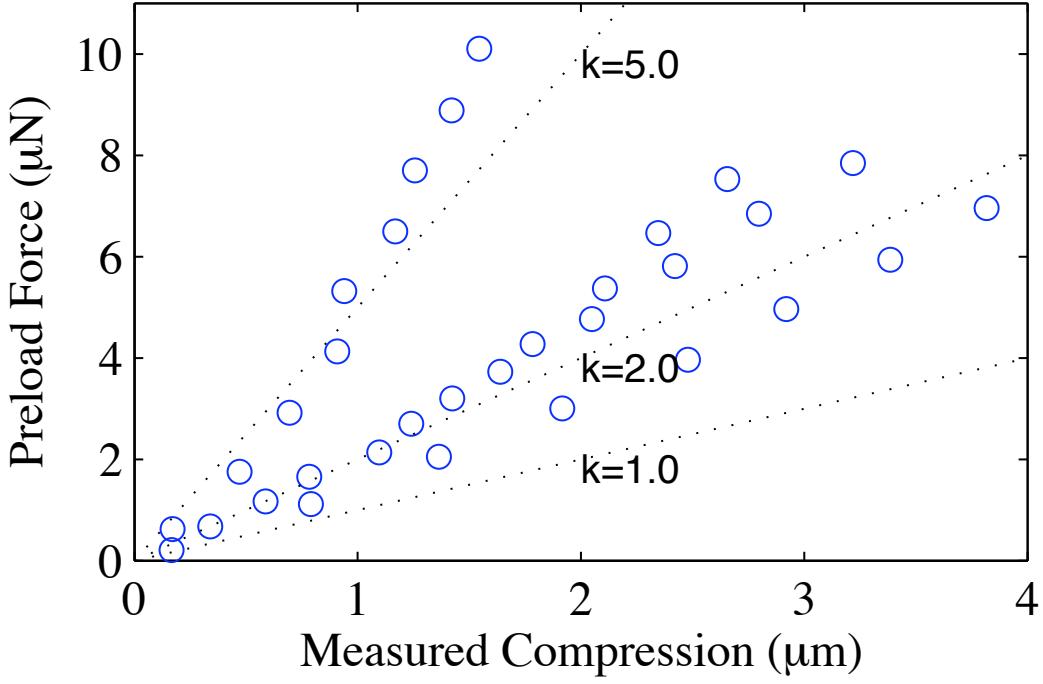
Figure A.1: Axial compression for tapered adhesive pillar. Sample was rotated about long axis. The spread in the data illustrates the uncertainty arising from placement along the tip of the force cantilever.

between them is

$$\frac{1}{k_P} = \frac{1}{k_E} - \frac{1}{k_C} \tag{A.1}$$

We measure the k_E of the system and then use the known spring constant of the cantilever k_C to calculate the pillar's spring constant. The tapered pillar is predicted to be about 2–3 times stiffer than the cantilever's normal compliance. In this case, the correction for the spring constant is necessary for a meaningful measurement.

Figure A.1 shows measured data of a tapered adhesive pillar sample under axial compression. The measured compression axis is the compression of the pillar. The plot has data from four rotation angles. Because of the variability in normal force as a function of placement on the tip of the cantilever, there is a large range of measured spring constants.

The modeled spring constant for a tapered beam is given by

$$k = \frac{Ewb}{L}\frac{a-1}{\log a}.$$ (A.2)

For numbers matching the tapered pillar structure (E modulus of 1MPa w and b the base and width of the structure are 20 μm, $L = 60$ μm and $a = 0.25$. Here a represents the amount of taper in the pillar, with $a = 1$ being a uniform beam, and with $a = 0$ describing a perfect point. The resulting spring constant is $k = 3.6$ N/m which is in within the spread shown in A.1.

A.1.2   Lateral Compliance

The lateral compliance measurement is similar to the normal measurement but instead used the side of the cantilever and pressed in the lateral direction. Two differences arise in this case. The first is that the sensitivity to the point of contact is reduced when using the cantilever in the shear direction. This is because the cantilever uses a truss structure. The second difference is that the cantilever has a different spring constant in the lateral direction. Because the compliance of the pillar is much greater in shear than axial, the force cantilever is stiffer than the structure under test. It was the opposite in the axial compliance measurement. Despite the relative spring constants, the correction described above was also performed on these measurements.

These values are clustered around $k = 0.1$ N/m. Using the elastica model described in Chapter 6 and the values used above in the axial compression, we obtain a spring constant of 0.08 N/m. This value is in excellent agreement with the measured value.
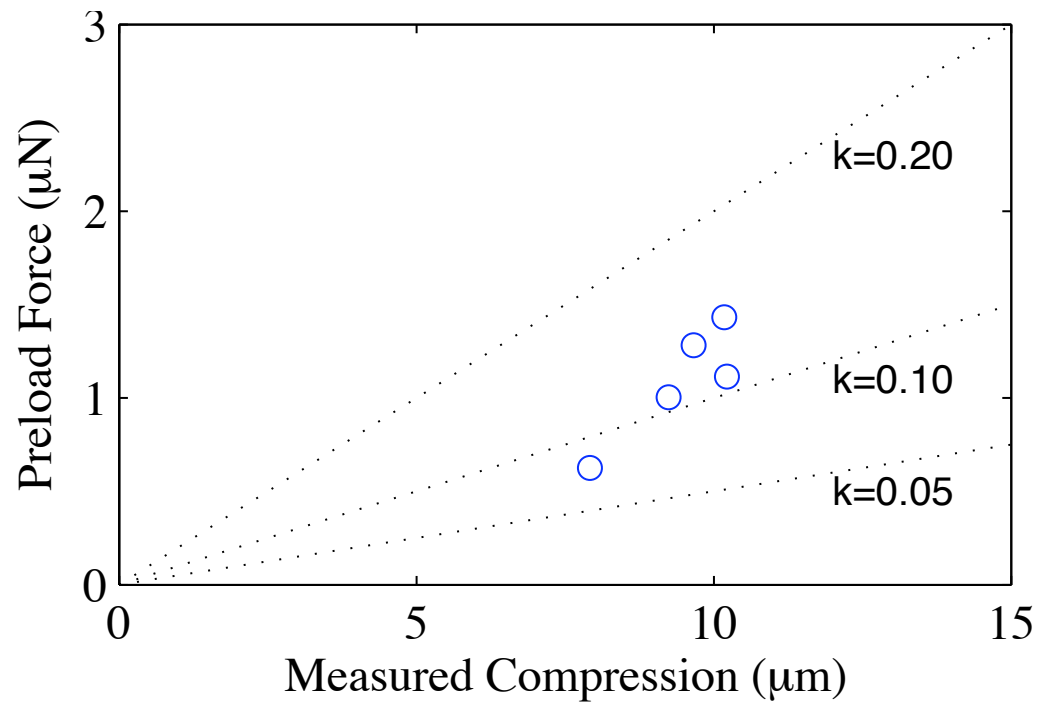
Figure A.2: Lateral compliance for tapered adhesive pillar. The measured compression is in the lateral direction.

Bibliography

[1] C. Gay and L. Leibler, "Theory of tackiness," *Physical Review Letters*, Jan 1999.

[2] A. Peattie, C. S. Majidi, A. Corder, and R. J. Full, "Ancestrally high elastic modulus of gecko setal -keratin," *Journal of The Royal Society Interface*, vol. 4, no. 17, pp. 1071–1076, Jan 2007.

[3] J. Israelachvili, *Intermolecular & Surface Forces*. Academic Press, 1985.

[4] C. Thornton, "Interparticle sliding in the presence of adhesion," *J. Phys. D: Appl. Phys*, vol. 24, pp. 1942–1946, Oct 1991.

[5] H. Yoshizawa, Y.-L. Chen, and J. Israelachvili, "Fundamental mechanisms of interfacial friction. 1. relation between adhesion and friction," *J. Phys. Chem.*, vol. 97, pp. 4128–4140, Jun 1993.

[6] A. Savkoor and G. Briggs, "The effect of tangential force on the contact of elastic solids in adhesion," *Proceedings of the Royal Society of London. Series A, Mathematical and Physical Sciences (1934-1990)*, vol. 356, no. 1684, pp. 103–114, 1977.

[7] H. Hertz, "Uber die beruhrung fester elasticher korper," *Journal fur die reine und angewandte mathematik*, vol. 92, pp. 156–171, May 1881.

[8] K. Johnson, K. Kendall, and A. Roberts, "Surface energy and the contact of elastic solids," *Proceedings of the Royal Society of London. Series A*, Jan 1971.

[9] K. Autumn, A. Dittmore, D. Santos, M. Spenko, and M. R. Cutkosky, "Frictional adhesion: a new angle on gecko attachment," *Journal of Experimental Biology*, vol. 209, pp. 3569–3579, Jan 2006.

[10] K. Autumn, S. Hsieh, D. Dudek, J. Chen, C. Chitaphan, and R. J. Full, "Dynamics of geckos running vertically," *Journal of Experimental Biology*, vol. 209, pp. 260–272, Jan 2006.

[11] A. Geim, S. Dubonos, I. Grigorieva, K. Novoselov, A. Zhukov, and S. Y. Shapoval, "Microfabricated adhesive mimicking gecko foot-hair," *Nature Materials*, vol. 2, pp. 461–463, Jan 2003.

[12] S. Gorb, M. Varenberg, A. Peressadko, and J. Tuma, "Biomimetic mushroom-shaped fibrillar adhesive microstructure," *Journal of The Royal Society Interface*, vol. 4, pp. 271–275, Jan 2007.

[13] L. Ge, S. Sethi, L. Ci, P. Ajayan, and A. Dhinojwala, "Carbon nanotube-based synthetic gecko tapes," *Proceedings of the National Academy of Sciences*, vol. 104, no. 26, pp. 10 792–10 795, Jan 2007.

[14] B. Schubert, J. Lee, C. S. Majidi, and R. S. Fearing, "Sliding-induced adhesion of stiff polymer microfibre arrays. ii. microscale behaviour," *Journal of The Royal Society Interface*, Jan 2008.

[15] M. P. Murphy, B. Aksak, and M. Sitti, "Adhesion and anisotropic friction enhancements of angled heterogeneous micro-fiber arrays with spherical and spatula tips," *J. Adhesion Sci. Technol*, vol. 21, no. 12-13, pp. 1281–1296, Jan 2007.

[16] S. Kim and M. Sitti, "Biologically inspired polymer microfibers with spatulate tips as repeatable fibrillar adhesives," *Applied Physics Letters*, vol. 89, no. 26, p. 261911, Jan 2006.

[17] L. Qu, L. Dai, M. Stone, Z. Xia, and Z. L. Wang, "Carbon nanotube arrays with strong shear binding-on and easy normal lifting-off," *Science*, vol. 322, no. 5899, pp. 238–242, Oct 2008.

[18] B. Aksak, M. Sitti, A. Cassell, J. Li, and M. Meyyappan, "Friction of partially embedded vertically aligned carbon nanofibers inside elastomers," *Applied Physics Letters*, Jan 2007.

[19] J. Lee, R. S. Fearing, and K. Komvopoulos, "Directional adhesion of gecko-inspired angled microfiber arrays," *Applied Physics Letters*, vol. 93, no. 19, p. 191910, Jan 2008.

[20] E. Arzt, S. Gorb, and R. Spolenak, "From micro to nano contacts in biological attachment devices," *Proceedings of the National Academy of Sciences of the ...*, vol. 100, no. 19, pp. 10 603–10 606, Jan 2003.

[21] A. del Campo, C. Greiner, and E. Arzt, "Contact shape controls adhesion of bioinspired fibrillar surfaces," *Langmuir*, vol. 23, no. 20, pp. 10 235–10 243, Jan 2007.

[22] B. Aksak, M. P. Murphy, and M. Sitti, "Adhesion of biologically inspired vertical and angled polymer microfiber arrays," *Langmuir*, vol. 23, pp. 3322–3332, Jan 2007.

[23] H. Jeong, J. Lee, H. Kim, S. Moon, and K. Suh, "A nontransferring dry adhesive with hierarchical polymer nanohairs," *Proceedings of the National Academy of Sciences*, Jan 2009.

[24] D. Santos, M. Spenko, A. Parness, S. Kim, and M. R. Cutkosky, "Directional adhesion for climbing: theoretical and practical considerations," *Journal of Adhesion Science and Technology*, vol. 21, no. 12-13, pp. 1317–1341, 2007.

[25] N. Rizzo, K. Gardner, D. Walls, N. Keiper-Hrynko, T. Ganzke, and D. Hallahan, "Characterization of the structure and composition of gecko adhesive setae," *Journal of The Royal Society Interface*, vol. 3, no. 8, pp. 441–451, 2005.

[26] R. Ruibal and V. Ernst, "The structure of the digital setae of lizards," *Journal of Morphology*, vol. 117, no. 3, 1965.

[27] K.-Y. Hung, H.-T. Hu, and F.-G. Tseng, "Application of 3d glycerol-compensated inclined-exposure technology to an integrated optical pick-up head," *J. Micromech. Microeng.*, vol. 14, no. 7, pp. 975–983, 2004.

[28] H. Sato, Y. Houshi, and S. Shoji, "Three-dimensional micro-structures consisting of high aspect ratio inclined micro-pillars fabricated . . . ," *Microsystem Technologies*, vol. 10, pp. 440–443, Jan 2004.

[29] M. Han, "3d microfabrication with inclined/rotated uv lithography," *Sensors and Actuators A: Physical*, vol. 111, no. 1, pp. 14–20, 2004.

[30] Y.-K. Yoon, J.-H. Park, and M. G. Allen, "Multidirectional uv lithography for complex 3-d mems structures," *J Microelectromech S*, vol. 15, no. 5, pp. 1121–1130, 2006.

[31] M. Sitti and R. S. Fearing, "Synthetic gecko foot-hair micro/nano-structures as dry adhesives," *Journal of Adhesion Science and Technology*, vol. 17, Jan 2003.

[32] D. Santos, "Contact modeling and directional adhesion for climbing robots," Ph.D. dissertation, Stanford University, Oct 2007.

[33] A. Parness, D. R. Soto, N. Esparza, N. Gravish, M. Wilkinson, K. Autumn, and M. R. Cutkosky, "A microfabricated wedge-shaped adhesive array displaying gecko-like dynamic adhesion, directionality and long lifetime," *Journal of the Royal Society*, vol. 6, no. 41, pp. 1223–1232, Jan 2009.

[34] A. Parness, "Micro-structured adhesives for climbing applications," Ph.D. dissertation, Stanford University, Feb 2010.

[35] B. Chui, T. Kenny, H. Mamin, B. Terris, and D. Rugar, "Independent detection of vertical and lateral forces with a sidewall-implanted dual-axis piezoresistive cantilever," *Applied Physics Letters*, vol. 72, no. 11, pp. 1388–1390, Jan 1998.

[36] K. Autumn, Y. Liang, S. Hsieh, W. Zesch, W. Chan, T. Kenny, R. S. Fearing, and R. J. Full, "Adhesive force of a single gecko foot-hair." *Nature*, vol. 405, no. 6787, pp. 681–685, Jan 2000.

[37] G. Hill, "Dual-axis mems force sensors for gecko adhesion studies," Ph.D. dissertation, Stanford University, Feb 2009.

[38] S. Goyal, A. Ruina, and J. Papadopoulos, "Planar sliding with dry friction part 1. limit surface and moment function," *Wear*, vol. 143, pp. 307–330, 1991.

[39] A. Asbeck, S. Dastoor, A. Parness, L. Fullerton, N. Esparza, D. R. Soto, B. Heyneman, and M. R. Cutkosky, "Climbing rough vertical surfaces with hierarchical directional adhesion," *IEEE International Conference on Robotics and Automation*, 2009.

[40] C. S. Majidi, R. E. Groff, and R. S. Fearing, "Attachment of fiber array adhesive through side contact," *Journal of Applied Physics*, vol. 98, no. 10, p. 103521, Jan 2005.

[41] R. Frisch-Fay, *Flexible Bars.* Butterworth and Co., 1962.

[42] Y. Tian, N. Pesika, H. Zeng, K. Rosenberg, and B. Zhao, "Adhesion and friction in gecko toe attachment and detachment," *Proceedings of the National Academy of Sciences*, vol. 103, no. 51, pp. 19 320–19 325, Jan 2006.

[43] Y. Xiang and D. A. Lavan, "Analysis of soft cantilevers as force transducers," *Applied Physics Letters*, vol. 90, no. 13, p. 133901, Jan 2007.

[44] N. Glassmaker and C.-Y. Hui, "Elastica solution for a nanotube formed by self-adhesion of a folded thin film," *Journal of Applied Physics*, vol. 96, no. 6, pp. 1–6, Aug 2004.

[45] J.-J. Wu, "Adhesive contact between a cylinder and a half-space," *J. Phys. D: Appl. Phys*, vol. 42, p. 155302, Jul 2009.